

UNIVERSITY OF OKLAHOMA

GRADUATE COLLEGE

A SIMULATION AND ANALYTICAL STUDY ON THE PERFORMANCE OF GAS-
LIQUID CENTRIFUGAL DOWNHOLE SEPARATORS

A THESIS

SUBMITTED TO THE GRADUATE FACULTY

in partial fulfillment of the requirements for the

Degree of

MASTER OF SCIENCE

By

LAURA CAMILA OSORIO OJEDA

Norman, Oklahoma

2023

A SIMULATION AND ANALYTICAL STUDY ON THE PERFORMANCE OF GAS-LIQUID
CENTRIFUGAL DOWNHOLE SEPARATORS

A THESIS APPROVED FOR THE
MEWBOURNE SCHOOL OF PETROLEUM AND GEOLOGICAL ENGINEERING

BY THE COMMITTEE CONSISTING OF

Dr. Hamidreza Karami Mirazizi, Chair

Dr. Xingru Wu

Dr. Hamidreza Shabgard

© Copyright by LAURA CAMILA OSORIO OJEDA 2023

All Rights Reserved.

ACKNOWLEDGMENTS

First, thanks to God, the Almighty, whose blessings have guided and protected me. I am truly thankful for my mother's unwavering support, who has selflessly given everything for me. Her love and sacrifices have been my source of strength. To my godmother for her honest advice throughout my life; to my father, who has been a constant pillar in my life despite the difficulty of seeing me leave his side; and to my uncle, who always has celebrated my achievements.

Thanks to my advisor, Dr. Karami. Since 2017, his encouragement, guidance, and pedagogy have been instrumental in helping me achieve numerous goals. I sincerely appreciate my committee members, Dr. Shabgard; your teachings on ANSYS, patience, and enthusiasm have shaped my understanding. Dr. Wu, thank you for your insightful suggestions and feedback. Additionally, I would like to give a special acknowledgment to Dr. Chang and Dr. Teodoriu, whose passion for mechanical engineering has instilled in me a deep love for my second major.

I want to thank my partner, Colton, for always being supportive and exceptional. To my dearest friends in Norman, Oklahoma, your companionship has filled my graduate school experience with happiness and fellowship, especially to Michael Olubode and Jeff McCaskill, who mentored me at the beginning of my research, and to Gloria and Mitch Burros for being my family away from home. Finally, a lighthearted appreciation goes to my ever-present cat, Coca-Cola, who has been a 24/7 emotional support, even if it means occasionally stepping on my keyboard.

Each of you has played a crucial role in shaping my academic, professional, and personal journey, allowing me to complete this thesis; for that, I am profoundly thankful.

Live On, University! #BoomerSooner

TABLE OF CONTENTS

ACKNOWLEDGMENTS	iv
TABLE OF CONTENTS.....	v
LIST OF TABLES.....	viii
LIST OF FIGURES	ix
ABSTRACT	xiii
CHAPTER 1: INTRODUCTION	1
1.1. Problem Statement.....	3
1.2. Objective.....	5
1.3. Scope of Work	5
CHAPTER 2: LITERATURE REVIEW	6
2.1. Downhole Gravitational Separators.....	6
2.2. Downhole Centrifugal Separators.....	7
2.2.1. Dynamic Downhole Centrifugal Separators	8
2.2.2. Static Downhole Centrifugal Separators.....	9
2.3. Gas-Liquid Centrifugal Separation Technology in Surface Separators.....	11
2.3.1. Tangential Surface Centrifugal Separators	12
2.3.2. Axial Surface Centrifugal Separators	13
2.4. Parameters Influencing Gas-Liquid Centrifugal Separation.....	15

2.5. Methodologies to evaluate separators' performance.....	18
2.5.1. Laboratory Testing.....	18
2.5.2. Computer Fluid Dynamic (CFD) Simulation	23
CHAPTER 3: CFD SIMULATIONS	39
3.1. Geometry Design.....	39
3.1.1. CAD Model.....	41
3.2. Meshing	44
3.2.1. Grid Independence Study.....	48
3.3. Modeling Set-up	55
3.4. Results.....	57
3.4.1. Single-Phase Flow Simulations with Constant Outlet Pressure	58
3.4.2. Single-Phase Flow Simulations with Constant Outlet Mass.....	69
3.4.3. Multiphase Flow Study Cases.....	74
CHAPTER 4: MACHINE LEARNING ANALYSIS	85
4.1. Data Collection	85
4.2. Operational and Geometrical Parameters	88
4.3. Dimensional Analysis	92
4.3.1. Weber Number.....	94
4.3.2. Reynolds Number	94
4.3.3. Taylor Number.....	95

4.4. Machine Learning Model Application.....	96
4.4.1. Data Preprocessing.....	96
4.4.2. Machine Learning Models	98
4.5. Modeling Results	99
4.6. Variable Importance	101
CHAPTER 5: FINAL REMARKS	106
5.1. Summary and Conclusions	106
5.2. Recommendations.....	109
REFERENCES	111

LIST OF TABLES

Table 2.1. Summary table of the parameters influencing the gas-liquid centrifugal separation. .	18
Table 2.2. Physical Models used by different authors in the literature.....	34
Table 2.3. Boundary conditions used by some authors in the literature.....	36
Table 3.1. Descriptions of the Geometry Boundaries.....	43
Table 3.2. Meshes used in Grid Independence Study.....	49
Table 3.3 Grid Independent Study Results For the Six Selected Meshes.....	50
Table 3.4. Selected mesh characteristics.....	52
Table 3.5. averaged y^+ values for the walls in the domain	54
Table 3.6. Single-phase simulation results using pressure outlets.....	59
Table 3.7. Single-phase cases using mass-flow outlets	70
Table 3.8. Single-phase Case 3 (water) vs. Multiphase Case 9 (water-air).....	74
Table 3.9. Multiphase flow cases (10, 11, 12, and 13) boundary conditions and results	78
Table 4.1. Flow parameters for the data considered in the analysis (Osorio et al., 2023).....	88
Table 4.2. Dimensionless Analysis (Parameters, Units, and Dimensions).....	93
Table 4.3. Data split percentages	97
Table 4.4. Machine Learning Results	100

LIST OF FIGURES

Figure 2.1. Inverted Shroud Technology (Adapted from Bohorquez 2006).....	7
Figure 2.2. The Main Components of Dynamic Downhole Centrifugal Separators (Osorio et al., 2023)	8
Figure 2.3. Fluid path in a Dynamic Centrifugal Separator.....	9
Figure 2.4. Static Downhole Centrifugal Separator, Texas Twister (Adapted from Bohorquez et al. 2009).....	10
Figure 2.5. Static Downhole Centrifugal Separator, Helix-type (Taken from Olubode et al. 2022)	11
Figure 2.6. Tangential Surface Centrifugal Separators: A. Vertical Annular Separation and Pumping (VASP) (from Do Vale and Garcia et al. 2002). B. Gas-Liquid Cylindrical Cyclone (GLCC) (from Hreiz et al. 2014).	12
Figure 2.7 Axial Surface Centrifugal Separators: A. Single-Swirl Separator (from Zheng et al. 2019). B. Multi-Swirl Separator (from Wang et al. 2019).....	14
Figure 2.8. Centrifugal gas-liquid separators classification (from Osorio et al. 2022)	15
Figure 2.9. Static separator testing facility (from Olubode et al. 2022)	20
Figure 2.10. Surface centrifugal separator testing facilities. A. Tangential Separator testing facility (from Hreiz et al. 2014). B. Axial Separator testing facility (from Wang et al. 2019).....	21
Figure 2.11. Control envelope for laboratory testing (from Wang et al. 2010).....	23
Figure 2.12. Inverted Geometry concept applied to a Stainless-Steel Pipe	24
Figure 2.13. Element types. Adapted from ANSYS Fluent User Guide.	26

Figure 2.14. Hybrid mesh for a dynamic centrifugal downhole separator (from Abbariki et al. 2020).....	27
Figure 2.15. Turbulence models' hierarchy	31
Figure 3.1. Schematic of the static downhole centrifugal separator (Olubode et al. 2021).....	40
Figure 3.2. gas-liquid separation system schematic.....	41
Figure 3.3. Numerical simulation control volume	42
Figure 3.4. Solid geometry simplification (cross-sectional view)	42
Figure 3.5. Inverted Geometry: Fluid domain (cross-sectional view).....	43
Figure 3.6. Final CAD Model.....	44
Figure 3.7. Impact of cell size in the mesh	45
Figure 3.8. Growth Rate impact in mesh generation	46
Figure 3.9. Growth Rate impact on boundary generation.....	46
Figure 3.10. Boundary layer types tested in meshing analysis.....	47
Figure 3.11. Simulation time (h) vs. Number of cells plot.....	50
Figure 3.12. Inlet Flux (kg/s) vs. Number of cells plot.....	51
Figure 3.13. Inlet Pressure (Pa) vs. Number of cells	52
Figure 3.14. Final Selected Mesh	55
Figure 3.15. Steady state achievement during transient simulations.....	58
Figure 3.16. air particle pathline in Case 2.....	61
Figure 3.17. Cases 1 to 4 velocity contours.....	62
Figure 3.18. Vortex cores or eddies formation.....	63
Figure 3.19. Cases 1 to 4 dynamic pressure contours.....	64
Figure 3.20. cases 1 to 4 velocity profiles in the bottom outlet.....	65

Figure 3.21. cases 1 to 4 velocity profiles in the top outlet	67
Figure 3.22. Eddies formation in the top section of the separator.	68
Figure 3.23 Instantaneous static pressure contours for cases 1 to 4 in the expelling section.	69
Figure 3.24. Cases 5 to 8 dynamic pressure contours.....	71
Figure 3.25. Velocity profiles of cases 5 to 8 close to the bottom outlet.....	72
Figure 3.26. Velocity profiles of cases 5 to 8 close to the top outlet.....	73
Figure 3.27. air and water particle pathlines inside and outside the helical paths	73
Figure 3.28. Case 9 contours of velocity, dynamic pressure, and water volume fraction	76
Figure 3.29. Y-velocity profile for Case 9 in the bottom outlet.	77
Figure 3.30. Velocity profiles for Case 10.....	80
Figure 3.31. Cases 11, 12, and 13 Y-velocity profiles close to the bottom and top outlet.	81
Figure 3.32. water volume fraction contours for cases 11, 12, ad 13.	82
Figure 3.33. Dynamic pressure in the helix-type paths for case 13.....	83
Figure 3.34. CFD vs Laboratory testing	84
Figure 4.1. Downhole centrifugal separators used for data analysis. (Alhanati 1993, Lackner 1997, Bohorquez et al. 2009, Wang et al. 2018, and Olubode et al. 2022)	87
Figure 4.2. The average efficiencies of the tested separators	89
Figure 4.3. Gas Efficiency for Different Separator Types and <i>vSL</i> ranges (Osorio et al., 2023) 90	
Figure 4.4. Liquid flow rate (BPD) vs. separation efficiency (Osorio et al., 2023)	91
Figure 4.5. Results of the Machine Learning Models.....	101
Figure 4.6. Bar plot of feature importance.....	102
Figure 4.7. Weber Number impact over separators' efficiency.	103
Figure 4.8. Bar plot for the feature of importance for the Accelerated Fan.	104

Figure 4.9. Gas Reynolds Number impact over the accelerated fan separator's performance... 104

Figure 4.10. Gas Reynolds Number impact over the efficiencies of the separators..... 105

ABSTRACT

A common issue in depleted oil and gas wells is the lack of energy to drive the fluids to the surface. Engineers use various artificial lift systems to solve this problem, most commonly by using pumps. Many pump types do not perform at their maximum capacity when working in the presence of gas. To address this problem, downhole separators can be used. This study seeks to understand the dynamics of the fluid flow inside one of the common types of such separators, static downhole centrifugal type. The study compiles an extensive literature review of gas-liquid centrifugal separation.

Data are collected from the literature review to feed a machine learning model and predict the equipment's efficiency. A total of 272 data points are extracted from the literature. These data are used to perform dimensional analysis and obtain dimensionless numbers to feed five machine learning algorithms: linear regression, random forest, K-nearest neighbor, support vector machine, and voting. The data are used to determine the best model in predicting separation efficiency. The voting algorithm is the best predictor for this dataset. It has a cross-validated adjusted R² of 0.535 and RMSE of 0.138 on the set. This means that the predictor can represent 53.5% of the variance in gas separation efficiency data with an error of 13.8%.

Single-phase and multiphase study cases are run of the fluid domain of a static centrifugal separator using ANSYS Fluent 2023. Realizable k-epsilon turbulence and multiphase Eulerian models are used for the conducted simulations with pressure and mass-flow rate boundary conditions. Pressure, velocity, and volume fraction contours, and outlet velocity profiles are analyzed for each case.

From the single-phase cases, it is observed that the velocity of the fluids increases about five times in the outermost section of the helix-type path of the separator. In all the cases, the fluids leave the domain through the top outlet, which has the biggest cross-sectional area. Eddies or vortices are formed in certain cornering sections of the equipment. Future re-designs can be performed to minimize these eddies. Additionally, eddies in the separator's upper section are caused by the high velocity at which the fluids are expelled from the helical section to the annulus.

The gas-liquid flow was studied inside the helix-type paths through the multiphase study cases. The totality of the liquid was expelled through the bottom outlet. Furthermore, from these cases, it was verified the importance of having a higher pressure at the bottom outlet for the correct convergence of the study cases. Through analysis of the velocity profiles in the outlets, it can be seen how the air tends to leave the domain through the top outlet, while the water through the bottom outlet. It was observed that pressure control influences the separator performance, when the bottom outlet pressure is set as 1500 Pa higher than the top outlet pressure, the water leaving the domain through the bottom outlet is 98.3% and the air leaving through the top outlet is 85%.

CHAPTER 1: INTRODUCTION

The oil and gas industry aims to meet the global energy demands by extracting substantial amounts of hydrocarbons. The fluids are produced by constructing wells that reach reservoirs of interest. The sector follows an integrated development path with five phases: exploration, drilling, completion, production, and abandonment. After a well is drilled, it is completed with perforations for flow from the reservoir to the wellbore. As the completion phase ends, production engineering becomes paramount to ensure efficient utilization of resources. The overarching objective of the production phase is to maximize the reservoir's fluid contents extraction while keeping the expenses low, consequently generating substantial economic gains.

Part of a production engineer's plan involves deciding on the well's oil recovery method during different stages of its productive life according to the well deliverability. During natural flow primary recovery, the hydrocarbon production enabler is the bottomhole pressure. The higher this pressure, the stronger the energy is to drive fluids from the high-pressure bottomhole to the low-pressure surface. However, the bottomhole pressure is often insufficient to drive the fluids, particularly as the well matures and the pressure declines. In such cases, other types of oil recovery will need to be implemented.

The bottomhole pressure can be low due to different factors, affecting the wellbore dynamics. One common reason is the depletion of the reservoir fluids in mature oil and gas fields due to the high extraction rates from the reservoir over several years. Additionally, geological features or operational factors, such as improper well design and equipment issues, can lower the bottomhole pressure. Once the pressure falls to a point where natural flow is no longer profitable,

artificial lift systems are implemented to boost the production. Some of these methods include gas lift, plunger lift, and pumping lift systems.

As the name indicates, pumping lift systems use pumps to convert electrical energy into hydraulic energy and increase the fluid pressure at the bottom of the well. The pumping systems currently used in the oil and gas industry are Sucker Rod Pumps (SRP), Electrical Submersible Pumps (ESP), Progressive Cavity Pumps (PCP), and Jet Pumps. These methods have high success rates and have been used in the energy industry for decades. They use traditional pumps designed to work with liquids. The implementation of these pumps is typically reserved for applications where liquids represent the bigger fraction of the extracted fluids, or in ideal cases, where only liquid is being produced. However, multiphase flow is common when dealing with fluids on pressure-fluctuating systems, such as wells. Hence, the pumps must handle some gas flowrates.

Wells represent an engineering challenge due to their longitude and amount of equipment used in their production, making pressure losses inevitable. While the pressure losses increase, the reservoir fluid falls into the two-phase (liquid-gas) envelope, quickly reaching high free gas production levels and increasing the gas-liquid ratio (GLR) (Osorio et al., 2023). Depending on the installed pumping artificial lift, the gas tolerance varies. PCP tolerates high percentages of free gas, while SRP and ESP have lower tolerances.

Free gas in pumps entails problems that detriment the performance of the equipment and subsequently cause failures. Gas locking, cavitation, increased wear and tear, and vibration are issues that contribute to the loss of efficiency, which might be influenced by an increased of GVF due to low pump intakes (Praveen Adiraju, 2023), reduced production, pressure fluctuations, and unpredictable performance of the equipment. Particularly in ESP, the gas can cause degradation of the hydraulic head (Zhu et al., 2023). To mitigate these problems, pumps must be designed and

operated considering gas-handling capabilities. Solutions may involve pumps with special design adjustments, such as anti-cavitation features, setting pump intake below the perforations, or installing a gas-liquid downhole separator upstream of the pump.

1.1. Problem Statement

Downhole separators are installed to prevent the gas from entering the pump and affecting the pump's efficiency. The separator seeks to direct the gas to the casing-tubing annulus, while sending the liquid to the pump to work under full fillage. Downhole separators used in the oil and gas industry can be divided by their separation mechanism into gravitational and centrifugal, based on the same principle: density difference.

Gravitational separators rely on gravity alone to separate the phases. However, centrifugal separators use a stronger centrifugal force to separate fluids with different densities. They can operate efficiently at higher flow rates and under varying pressure conditions, making them crucial in downhole environments where fluid properties constantly fluctuate. They can separate phases with low density differences, enhancing their applicability in scenarios where gravitational forces alone would be insufficient.

As a fluid flows through a downhole centrifugal separator, the complex flow dynamics impact the separators' performance. Understanding the premises of centrifugal separation is crucial for achieving optimal operation. Working within the best efficiency range of a separator can help minimize damage to the production equipment and provide process stability. The oil and gas industry is not interested in centrifugal separation only because of its better separation performance. It is also because implementing this mechanism results in cost savings, as more

efficient equipment reduces reprocessing and maintenance needs. On top of that, it is a technology that can be implemented in the downhole, surface, and many stages along the production stream.

Laboratory testing is an excellent tool for studying a centrifugal separator's performance and collecting meaningful data for analysis. However, this method fails to detail the downhole fluid dynamics. Particularly, laboratory testing is insufficient in assessing how pressure, velocity, and design parameters interact to affect separation efficiency. Computational Fluid Dynamics (CFD) is a powerful tool to bridge this knowledge gap, enabling a comprehensive examination of fluid behavior. A CFD simulation solves the conservation laws (mass, momentum, and energy) governing fluid motion to predict the physics of the flow. This project uses CFD to simulate a novel static centrifugal separator experimentally tested and analyzed by Olubode et al. (2021). The purpose is to understand the physics of flow in centrifugal separators.

The last decade has brought efforts in implementing data analytics and machine learning for different applications in several industries. The energy industry collects thousands of data points annually. Using machine learning to build robust prediction algorithms from such data provides a solid foundation for many applications. This approach can be applied for downhole centrifugal separators based on the available laboratory data. Using data from experiments conducted on different types of centrifugal separators, one can predict the separator's performance and optimize its condition. In this study, the data from different separator designs, tested experimentally, were collected through an open literature review. The data points were used to build a robust machine-learning model. This novel approach provides a third way to evaluate the performance of a centrifugal separator besides laboratory testing and CFD simulation. In addition, it opens the possibility of combining these three methods to provide insights into separator dynamics and highlights the improvement areas to enhance the separator's overall performance.

1.2. Objective

This study has the following main objectives:

- Perform CFD simulations of flow through a static centrifugal downhole separator and analyze the data from the simulated scenarios.
- Collect and clean laboratory testing data from the open literature.
- Build a robust machine learning model to predict the performances of downhole centrifugal separators based on design and operational conditions.

1.3. Scope of Work

The nature of this work is computational, with CFD simulations and machine learning as the two applied approaches. The data used for the machine learning model were collected from the open literature, covering five types of centrifugal downhole separators.

This work includes five chapters. First, Chapter 2 shows a comprehensive review of the experimental and simulation works performed in the literature on centrifugal separators and their performance evaluations. Chapter 3 describes the CFD simulation design, applied procedures, and the result obtained from it. Chapter 4 presents a machine learning model based on the dimensional analysis of the data collected from the open literature. Chapter 5 concludes the study with the key findings of this research and provides some recommendations for future work in this field.

CHAPTER 2: LITERATURE REVIEW

This chapter collects the previous studies performed over the past 30 years in a comprehensive literature review on the topic of this work, centrifugal separators. The objective is to clarify the main concepts associated with this thesis. The review is not only limited to downhole centrifugal separators, also covering the surface centrifugal separation mechanisms in other stages of production. Previous laboratory testing and CFD simulation works are analyzed to understand the current knowledge gap. We start by discussing the differences between the gravitational and centrifugal separators.

2.1. Downhole Gravitational Separators

Gravitational separation involves allowing the gas to rise due to its lower density, while the liquid settles at the bottom due to its higher density. Downhole gravitational separators force the fluids to change flow direction (Lopez, 2021). The direction change caused by gravity forces the liquid to flow downward in an inverted-shroud-type chamber, while the gas is vented in the casing-tubing annulus, as seen in Figure 2.1. Some of the gravitational separators used in the oil and gas industry are Poor Boy, Patterson, Echometer, Don-Nan, Heal System, and Odesa (Lopez, 2021).

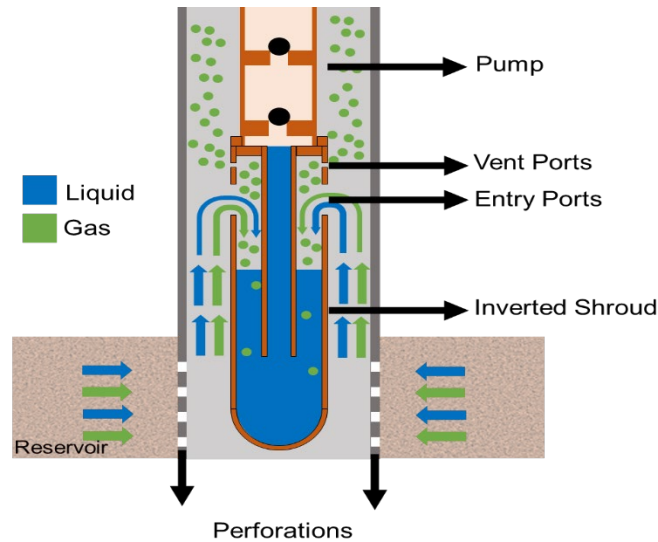


Figure 2.1. Inverted Shroud Technology (Adapted from Bohorquez 2006)

2.2. Downhole Centrifugal Separators

A major drawback of gravitational separators is the time consumed during the separation. Centrifugal separators use the centrifugal force to enhance and accelerate the process. Stoke's law governs the physical mechanism of gas-liquid separation (Ogunsina et al. 2005). This law describes how a particle (or bubble) travels through a fluid, depending on its size, viscosity, and density. Centrifugal separators forces an inflowing stream into a swirling motion to create a vortex-type phenomenon. This movement can be obtained by abruptly changing the direction of the fluid tangentially or by using helical elements or designs, such as augers. A such element generates a centrifugal force when the fluid enters the equipment axially. Following the same principle as gravitational separators, due to different gas and liquid densities, centrifugal forces drag the heavier liquid to the outer part of the vortex while the gas stays in the inner part (Osorio et al. 2023). Downhole centrifugal separators can be classified as static and dynamic separators.

2.2.1. Dynamic Downhole Centrifugal Separators

Dynamic downhole centrifugal separators are attached to a motor that rotates the equipment at a certain speed, commonly 3500 RPM. These types of separators are often used in ESP applications due to the availability of a motor that rotates the equipment. Nonetheless, they can also be implemented in SRP applications if a motor is added. A dynamic separator is composed of an intake, inducer (reducer), guide vanes, separation chamber (impeller), and crossover (Takacs 2018). Figure 2.2 displays two types of dynamic separators and their main components.

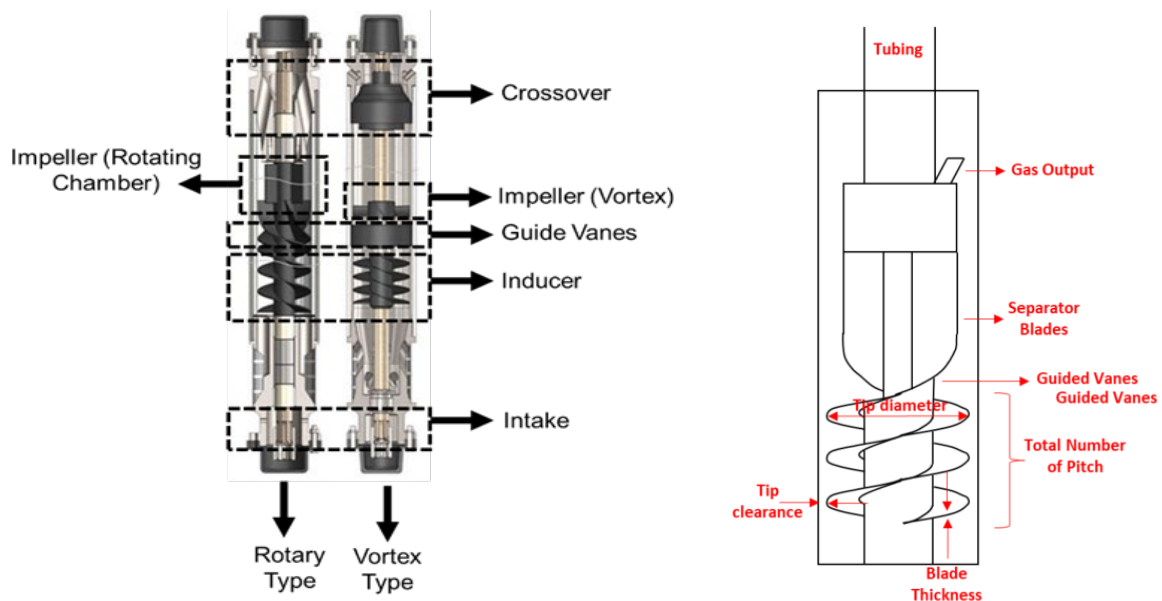


Figure 2.2. The Main Components of Dynamic Downhole Centrifugal Separators (Osorio et al., 2023)

Before the fluids enter the separator, a gravitational separation occurs in the casing annulus, allowing the free gas to flow upward, while the liquid with entrained gas accumulate at the bottom of the annulus (Osorio et al., 2023). The accumulated mixture enters the separator through the intake ports, as seen in Figure 2.3. This action causes a pressure loss that is compensated by a pressure head generated at the inducer section (Harun et al., 2004). Then, the fluid mixture is guided through smoothly moving vanes to the impellers, where the centrifugal forces enhance the separation (Osorio et al., 2023). After the separation occurs at the impeller, the liquid and gas are

sent to the crossover. The separated fluids reach the crossover section, where the gas is directed from the center of the generated vortex to the tubing-casing annulus, and the liquid is sent from the outer part of the generated vortex to the pump.

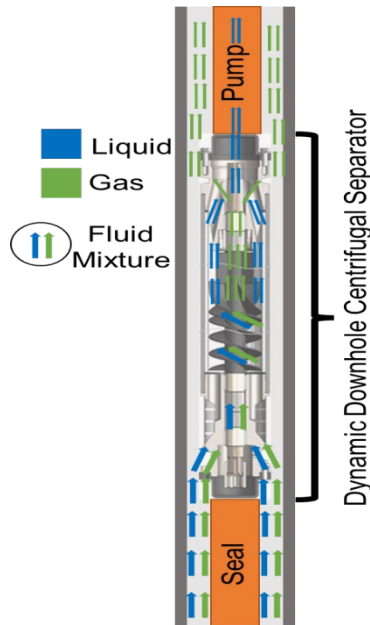


Figure 2.3. Fluid path in a Dynamic Centrifugal Separator.

2.2.2. Static Downhole Centrifugal Separators

Rather than being connected to a shaft, this separator type is set alone and attached to a tubing or a shroud pipe. These separators force fluids into a helix-type path, or an auger, to induce a swirling movement that eventually causes centrifugal separation. Some of these separators have been tested in the literature, like the Texas Twister, first studied by Bohorquez et al. (2009), displayed in Figure 2.4. This separator has a twisted dip tube set stationary inside a shroud. The intake is in the shroud's upper section. The fluid mixture is forced downward in a centrifugal motion along and outside the helical-shaped dip tube. During the descent, the separation occurs. The liquid flows to the lower part and eventually enters the dip tube, which discharges it into the

pump (Osorio et al., 2023). Meanwhile, the gas flows upward through the center of the chamber and leaves through the vent holes (Bohorquez et al. 2009).

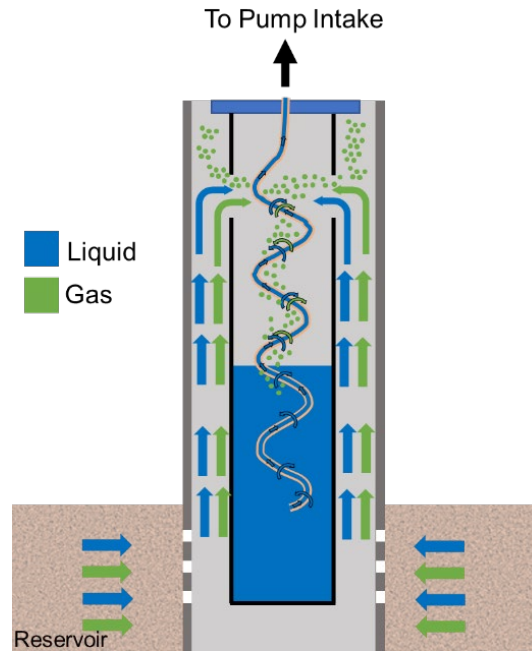


Figure 2.4. Static Downhole Centrifugal Separator, Texas Twister (Adapted from Bohorquez et al. 2009)

A modified style of the static separator was tested by Olubode et al. (2021). This packer-type centrifugal separator is attached to the tubing and inside a shroud pipe. The liquid-gas mixture enters the separator through a dip tube after passing the packer. The mixture is then immediately sent to the helical channel, which provides the centrifugal force to enhance the separation process. When the mixture gets expelled into the casing, this movement helps send the liquid, with a higher density, toward the outer wall and keep the gas, with a lower density, in the center. This action activates a second gravity separation, causing the gas to flow upward in the casing annulus while the liquid flows downward. The shroud's lower section sucks the liquid accumulated at the bottom into the tubing through a crossover and upward to the pump (Olubode et al., 2022). Figure 2.5 displays the separator described above.

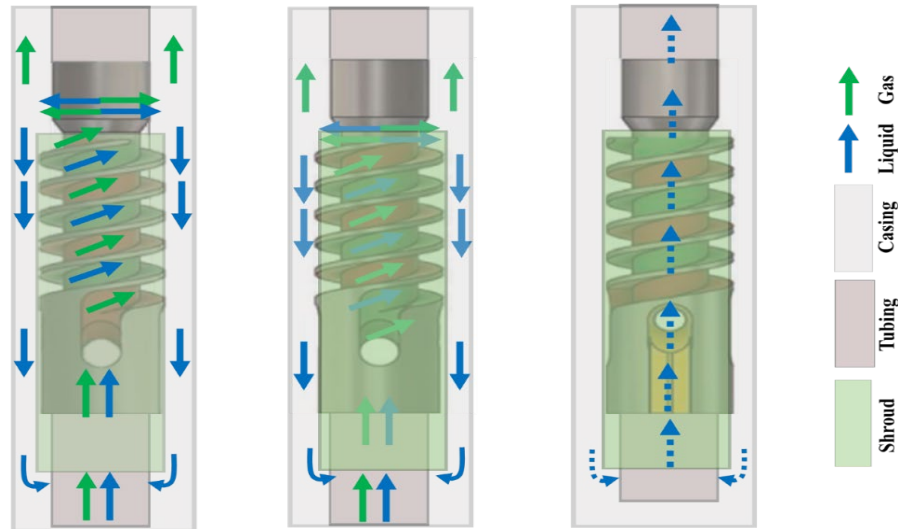


Figure 2.5. Static Downhole Centrifugal Separator, Helix-type (Taken from Olubode et al. 2022)

2.3. Gas-Liquid Centrifugal Separation Technology in Surface Separators

Gas-liquid separators have various downhole and surface applications related to the oil and gas industry and nuclear energy. The surface separation is essential to the function of a production facility. If too many liquid droplets are in the gas stream, high-cost issues and downtime may occur in equipment like compressors or burners. On the other hand, surface pumps incur cavitation in the presence of gas bubbles. Besides the oil and gas industry, nuclear industry safety depends on separating water-steam and fission gas in molt salt reactors (Zheng et al., 2019). The development of centrifugal separators solves the space problem of the traditional gravitational separators, which are massive equipment compared to the compact and lightweight centrifugal ones (Saeid Mokhatab et al., 2015). Surface Centrifugal Separators can be divided into tangential and axial separators.

2.3.1. Tangential Surface Centrifugal Separators

Tangential separators are designed to have an upper intake perpendicular to the direction of the bottom liquid outlet and upper gas outlet, as seen in Figure 2.6. These separators use centrifugal forces as leading sources of separation, and have secondary gravitational processes that help with the performance. In Vertical Annular Separation and Pumping System (VASP) equipment, the fluid mixture enters the equipment through a tangential inlet in the upper part of the apparatus, directly accessing a helix joint attached to the outer face of a pressure housing, generating the swirling movement, as seen in Figure 2.6-A. Another type of such separator is the Gas-Liquid Cylindrical Cyclone (GLCC), where the vortex is generated by a rough direction change of the fluid when impinging the front wall, as seen in Figure 2.6-B. Then, the mixture flows down in a swirl motion, causing the two phases to separate. While moving downward in the spiral, the gas gets pushed to the center of the equipment, subsequently flowing to an upper gas outlet. Meanwhile, the liquid accumulates in the bottom and is suctioned by the tubing in the equipment's center part (Hreiz et al., 2014).

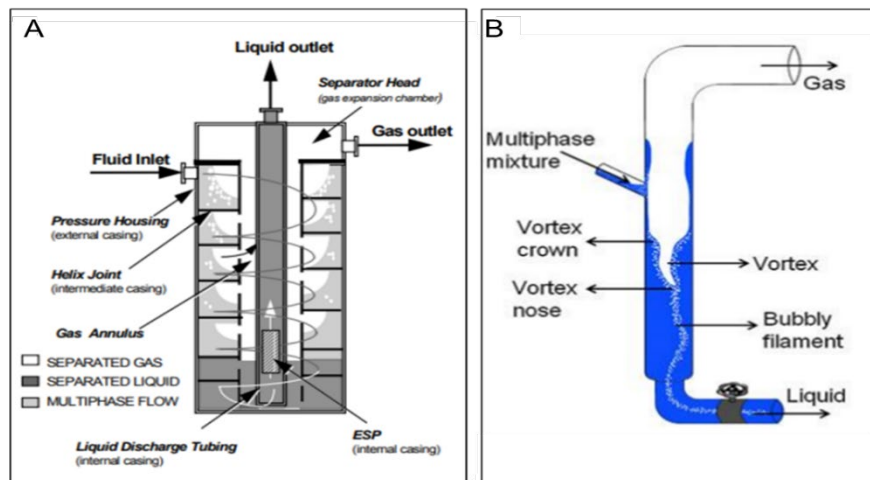


Figure 2.6. Tangential Surface Centrifugal Separators: A. Vertical Annular Separation and Pumping (VASP) (from Do Vale and Garcia et al. 2002). B. Gas-Liquid Cylindrical Cyclone (GLCC) (from Hreiz et al. 2014).

Two variables define the separator's efficiency in tangential separators: liquid carry-over (LCO) and gas carry-under (GCU). LCO occurs when the mixture's velocity in the separator's intake is too high, and the separation chamber is not long enough to deal with this condition (Rosa et al., 2001). The liquid flow rate also influences the amount and thickness of the liquid film above the inlet, causing LCO (Hreiz et al., 2014). Turbulence at the inlet increases the liquid level, and hence the LCO, which is reduced by inclining the inlet downward at an angle of 27° (Kouba et al. 1995). GCU, seen as the bubbly filament in Figure 2.6-B, occurs when the residence time swirling around the channels is short. If the swirling time is less than the time it takes the bubbles to travel across the liquid film and reach the gas core, dispersed bubbles will be present in the liquid core at the bottom of the separator (Rosa et al., 2001). The GCU is a function of the separator length and the liquid level in the separator.

2.3.2. Axial Surface Centrifugal Separators

Axial centrifugal separators have intakes normal to the direction of the flow. They have a swirl element generating centrifugal forces. This swirling motion is less intense than the tangential inflow separators (Niewstadt & Dirkzwager, 1995). These separators can be divided into single-stage swirl element and multi-stage swirl element separators, as seen in Figure 2.7. In single-stage swirl element separators, displayed in Figure 2.7-A, the fluid mixture enters the inner cylinder of the separator from the bottom, encounters a swirl element that generates a spiral movement, and enhances the centrifugal separation. The phases leave the inner cylinder through the vent holes to activate the gravitational separation, with the liquid falling downward and the gas moving freely to the upper part of the separator. At the gas outlet, a third separation process occurs with a baffle

plate. In this section, the tiny liquid droplets not retrieved by the two previous processes are contained (Zheng et al., 2019).

Multi-stage swirl element separators combine three swirl elements and two separation chambers, as displayed in Figure 2.7-B. They have four gas outlets throughout their structure. Like the previous separator, the fluid mixture enters from the bottom of the equipment directly to the first swirl element, where the vortex field is generated. The fluid is expelled to the so-called upstream chamber and set the separated gas-free through two gas outlets. The mixture continues traveling upwards and enters the second swirl element, the downstream swirling chamber, and then a third element that restores the pressure to avoid the collapse of the gas core (Zheng et al., 2020). The separated gas flows out of the separator through the fourth gas outlet. Meanwhile, the liquid flows upwards through the cylinder and exits from the top (Wang et al., 2019).

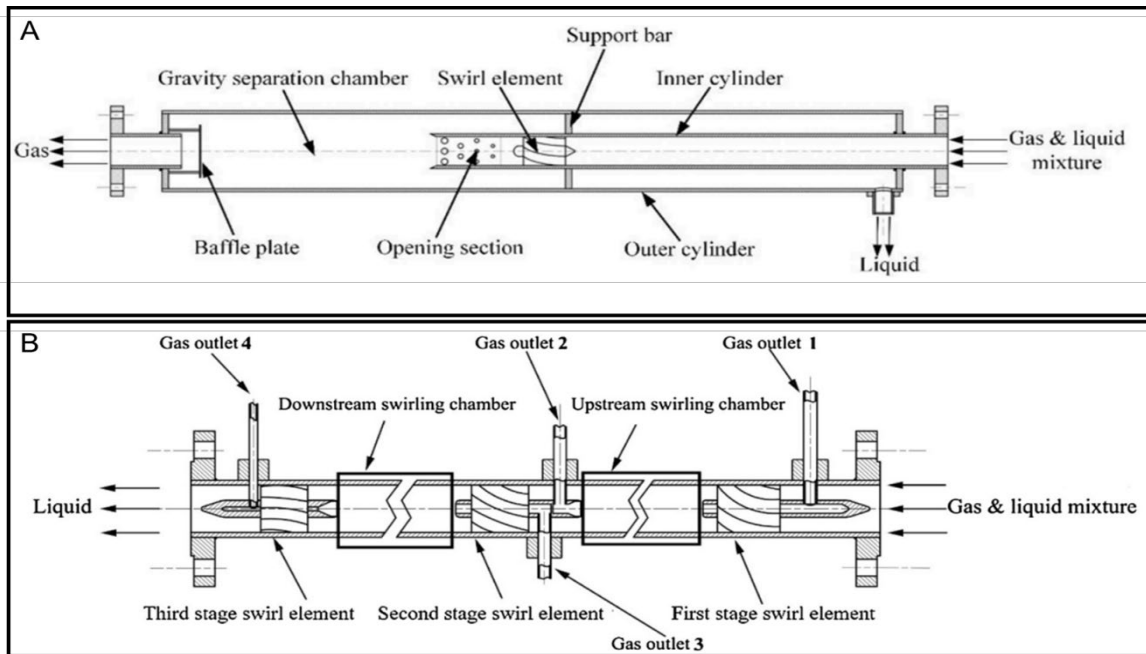


Figure 2.7 Axial Surface Centrifugal Separators: A. Single-Swirl Separator (from Zheng et al. 2019). B. Multi-Swirl Separator (from Wang et al. 2019)

Many separators have been designed for different applications. They can be divided based on the fluids or solids being separated (gas-liquid, liquid-liquid, liquid-solid, gas-solid), the type of inlet (axial or tangential), the mechanism (gravitational or centrifugal), the shape (vertical or horizontal). This thesis focuses on separators whose main separation mechanism is centrifugal and separates gas from liquid. The diagram in Figure 2.8 summarizes the classification of gas-liquid centrifugal separators in the oil and gas industry.

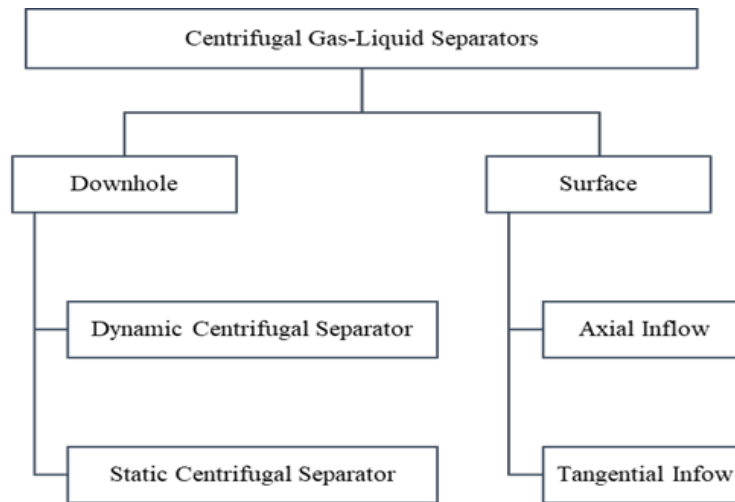


Figure 2.8. Centrifugal gas-liquid separators classification (from Osorio et al. 2022)

2.4. Parameters Influencing Gas-Liquid Centrifugal Separation

To understand the gas-liquid centrifugal separation, studying the parameters affecting its physics is critical. Three main concepts influence the separation performance of rotary gas separators: retention time, turbulence, and pressure head (Tackas 2018). The greater the retention time, the greater the separator's efficiency. Keeping the cross-sectional area of a dynamic separator as large as possible minimizes the axial velocity, resulting in higher retention times. Dynamic separators have integral outer housings (shells) that rotate with them during the operation. These shells are essential to maintaining minimal turbulence or flow shearing (Lea & Bearden, 1982).

Avoiding turbulence in centrifugal gas-liquid separators is critical, as high flow disturbances cause phase remixing (Alhanati et al. 1994).

The generation of sufficient pressure head is essential to overcome the pressure losses of flow through the inflow ports. The pressure head is the pressure generated by the helix-type path, or auger, also providing the centrifugal force. During the operation of a dynamic separator, gas is expelled to the casing-separator annulus area. The relationship between the pressure loss and the provided head by the inducer section controls the amount of ejected gas (Alhanati et al., 1994). This type of separator must be carefully designed to work under the right conditions and to avoid inducer overload reducing the head (Harun et al., 2002).

A factor to consider in the separator's performance is recirculation. There is a chance that liquid is expelled back to the annulus with the gas. As the liquid flows downward and recirculates into the separator, it may carry gas bubbles, affecting the gravitational separation at the bottom of the separator. Separators commonly handle different amounts of liquid and gas, which may alter their performances (Alhanati et al., 1994). The influence of physical properties, like viscosity, on the separator performance has also been evaluated. Lackner et al. (2002) found that liquid viscosity does not influence the efficiency of dynamic separators for liquids with viscosity range of 1-50 cp.

Like dynamic separators, the performances of static downhole centrifugal separators are governed by the pressure drop control, turbulence, and gas bubble dynamics. The pressure drop along the helical section must be minimized for the fluid to be expelled to the casing annulus. The pressure drop across the separator increases with gas and liquid flow rates (Olubode et al., 2021). McCoy et al. (2005, 2007, 2015) indicated that pressure drop should be minimized to prevent condensation and fragmentation in the separator. The size and shape of the gas bubbles influence these phenomena (Wang et al., 2018).

The forces affecting the gas-liquid separation dynamics are drag and buoyancy. The drag force tends to mix the liquid film and the gas bubbles. Meanwhile, the buoyancy force separates the phases by raising the gas (Derakhshan et al., 2018). This effect is easily identifiable in the casing-separator annulus when the natural separation occurs (Alhanati et al., 1994). The force balance is explained mathematically by Stoke's Law. It is deduced that the bubble rise velocity is proportional to its diameter (Olubode et al., 2021). Reducing the phase velocities minimizes the turbulence and the possibility of the liquid dragging bubbles into the pump. The rule of thumb in the industry is that 0.25-in. bubbles flow upwards at an approximate velocity of 6 in./s. (Lopez et al., 2019). Good separation occurs when the downward liquid velocity in the shroud is less than 6 in/s (Lopez et al., 2019). Thus, maximizing the downflow area to minimize the liquid velocity can improve the separation efficiency (Olubode et al., 2021). McCoy et al. (2007) concluded that separation is not guaranteed if the liquid velocity surpasses 7 in/s.

A key to efficient centrifugal separation is forming a rod-like gas core (Yin et al., 2015). Flow patterns upstream of the swirling element influence the state of the gas core (Wang et al., 2018). Flow patterns are directly related to the gas content, making the gas content an influential parameter for centrifugal separators. Thus, the flow pattern of the mixture must be considered for the design (Wang et al., 2018). Liquid levels are also essential for the correct usage of gas-liquid centrifugal separators. Several studies have used different control methods to achieve a stable liquid level. Sharma et al. (2020) built a test facility for downhole centrifugal gas-liquid separators. They controlled the liquid level by adjusting the casing and tubing head pressures using downstream control valves. A stable level prevents the gas from entering the shroud or tubing and avoids liquid production from the casing (Olubode et al., 2021). In surface centrifugal gas-liquid separators, the residence time is influenced by liquid level fluctuations, caused by factors such as

slugging (Wang et al., 2010). The efficiency of a separator is a function of implementing a specific control system to monitor the flow through it.

Table 2.1 summarizes the parameters mentioned here. The following section explains some of the tested systems in detail.

Table 2.1. Summary table of the parameters influencing the gas-liquid centrifugal separation.

Parameter	Retention Time	Fluid’s erratic motion (Turbulence and recirculation)	Pressure (Pressure head generation and pressure drop)	Fluid Dynamics (Liquid levels and gas content)
Description	Time the fluids spend in the separator.	Undesired parameters that need to be avoided through design improvement and control of operation conditions.	Sufficient pressure must be generated to overcome the frictional losses inside the separator	Liquid levels need to be kept stable. Selection of a centrifugal separator must be based on gas content

2.5. Methodologies to evaluate separators' performance

Two types of methodologies have been used by various authors to evaluate a separator's efficiency: experimental and simulation techniques. These laboratory testing and computational fluid dynamics simulation techniques are discussed in the following sections.

2.5.1. Laboratory Testing

Many studies are available in the literature, covering the lab testing of centrifugal separators. This type of testing has been the industry's preferred method for years. When testing surface and downhole separators, one may observe some similarities and some differences. Knowing the differences can help with new designs for future testing.

2.5.1.1. Downhole Gas-Liquid Centrifugal Separators

Laboratory facilities to test downhole gas-liquid centrifugal separators are similar in style. Some examples are the works of Lea & Bearden (1982); Alhanati (1993); Lackner (1997); Harun et al. (2004); Wang et al. (2018); Sharma (2019); Olubode (2021). A facility comprises a testing section, a gas-supply section, and a liquid-supply section. The testing section is commonly vertical with two long pipes acting as tubing and casing. The height of the casing pipes varies between 20 to 50 ft. The longer the vertical testing section, the more space the flow will have to be stabilized, resulting in higher accuracy.

Most laboratory tests in the literature use water and air as the testing fluids, mainly for safety reasons. However, Lea & Bearden (1982) used a mixture of diesel and carbon dioxide, and Lackner (1997) used two commercial mineral oils (Lubsnap 100 and Lubsnap 200) as the liquid. The gas supply gets mixed with the liquid supply at some point to obtain the input fluid mixture to the test section. Compressors provide the gas supply in an open loop, meaning that as soon as the separated gas leaves the test section, it is released to the atmosphere. In contrast, liquid supply sections are closed loops. Liquid leaves a storage tank and gets pumped to the test section. It then gets collected when leaving the separator and is returned to the tank. When rotary gas separators are tested, their facilities count with a motor and a shaft for rotation. Figure 2.9 displays an example of an experimental facility, used by Olubode et al. (2022).

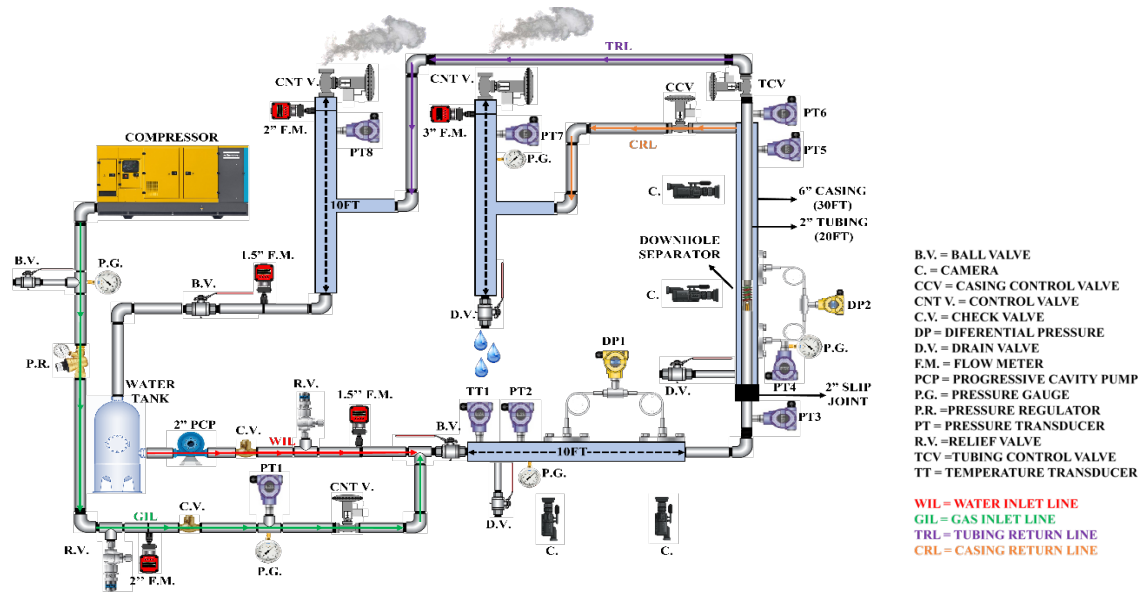


Figure 2.9. Static separator testing facility (from Olubode et al. 2022)

Control systems are used to abide specific parameters, such as pressure and liquid level, into desired ranges to determine efficiency and performance accurately. Lea and Bearden (1982) used manual adjustments to control the liquid supply and discharge lines to obtain a stable annulus fluid level. Alhanati (1993) used a globe valve in the liquid return line to apply back pressure to the system and control the testing pressure. Olubode et al. (2021) tested a static centrifugal downhole gas-liquid separator, as shown in Figure 2.9. They used a Casing Control Valve (CCV) to keep the liquid level in the casing-tubing annulus at a desired setpoint. The CCV was choked to apply backpressure and reduce the liquid level or opened to allow the liquid level to rise. This is due to the U-tube nature of the casing-tubing system. Opening the CCV reduces the casing head pressure compared to the tubing head pressure. On the other hand, the casing head pressure becomes more prominent than the tubing head pressure when the CCV is choked.

2.5.1.2. Surface Gas-Liquid Centrifugal Separators

Laboratory tests in the literature for surface separators consist of similar facilities to downhole separators. The facilities include separation sections, liquid and gas supply lines, and return lines. Figure 2.10 displays facilities for tangential and axial centrifugal surface gas-liquid separators, taken from Hreiz et al. (2014) and Wang et al. (2019).

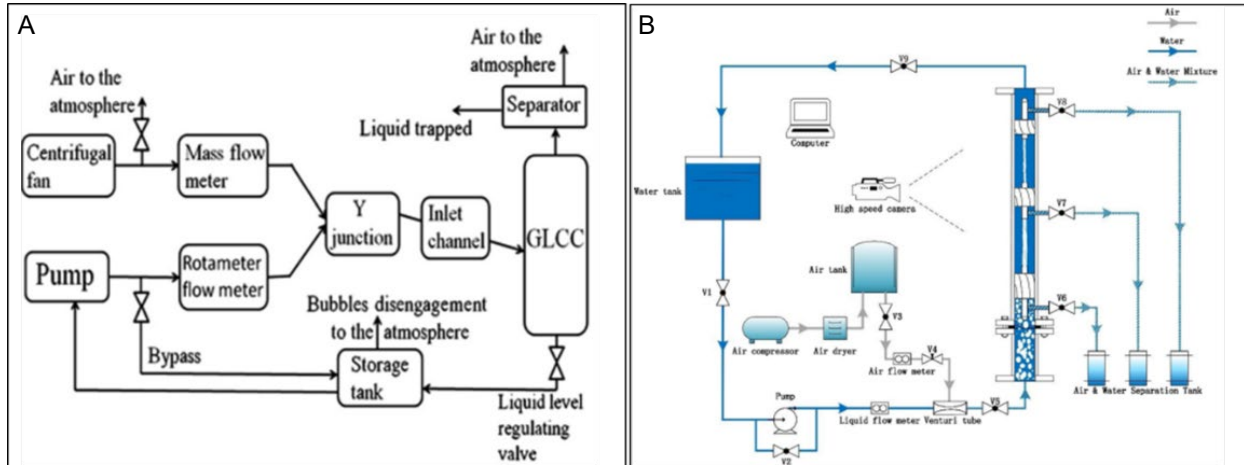


Figure 2.10. Surface centrifugal separator testing facilities. A. Tangential Separator testing facility (from Hreiz et al. 2014). B. Axial Separator testing facility (from Wang et al. 2019).

The flow becomes more unstable in surface centrifugal separators compared to gravitational separators, as the residence time is shorter. The flow instabilities can generate slugging (Wang et al., 2010). As mentioned previously, one of the parameters improving the performance of centrifugal separators is the flow control used to keep the flow rates within an expected range and keep the separation smooth. Wang et al. (2010) discussed control systems for facilities testing GLCC (tangential separators). They stipulated two types of control systems: feedback and feedforward controllers. A feedback controller reacts to a change in the output it analyzes, either liquid or gas, through controllers located in the output lines. When using a Liquid Control Valve (LCV), a sensor sends a signal when an undesired fluctuation occurs at the liquid level. Then, the controller responds by activating the control valve to influence the liquid outflow

and control the liquid discharge, thus modifying the liquid level. The procedure is similar to a Gas Control Valve (GCV), where the control valve adjusts the backpressure, which consequently modifies the liquid level as convenient (Wang et al., 2010).

A feedforward control measures the cause of the disturbance, and the actions affect the root problem. When using an LCV, a sensor detects liquid slugs at the inlet of the separator, sending a signal to the controller. This drives the control valve to match the outflow port to the same flow as in the inlet to maintain the liquid level at the desired set point. A similar process occurs when using a GCV, but the valve manipulates the backpressure to obtain the desired gas outflow and maintain the liquid level (Wang et al., 2010). The feedback control acts on the output and not the root of the problem, unlike feedforward control, which is considered less accurate (Wang et al., 2010).

Figure 2.11 displays an operational envelope designed by Wang et al. (2010). This envelope is considered to choose the best control strategy depending on the flow pattern in the separator. The 40 in. and 20 in. are the liquid level set points. For bubbly and stratified flow patterns, which are liquid-dominated, GCV is recommended. The recommendation for annular and mist flow, gas-dominated flows, is to use an LCV. The above strategies (LCV or GCV) can be accomplished using feedback or feedforward controls. On the other hand, slug flows need combined strategies from both types of controllers to control the level (Wang et al., 2010).

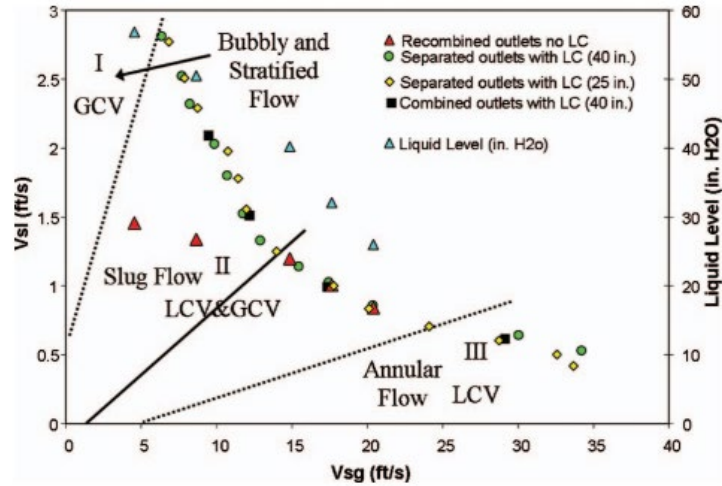


Figure 2.11. Control envelope for laboratory testing (from Wang et al. 2010)

2.5.2. Computer Fluid Dynamic (CFD) Simulation

Computational fluid dynamics (CFD) is a branch of fluid mechanics that mathematically predicts fluid-flow phenomena based on the conservation laws (mass, momentum, and energy) governing the fluid motion. These predictions are made for a meshed geometry with a series of fixed boundary conditions subjected to the physical properties and phenomena affecting the flow field (Howard H. Hu 2012). Thanks to the ever-growing computational power, CFD has become a powerful tool for studying the performances of different types of devices, such as downhole centrifugal separators. The simulations represent a suitable alternative to study cases with highly complicated phenomena, depending on too many variables to implement analytical solutions. These simulations are an ideal alternative when typical laboratory testing is limited and expensive. CFD allows engineers to make decisions early in the design process to save time and money.

Performing a CFD simulation involves several steps: geometry design, meshing, modeling, and solution. In the literature, several authors have attempted to simulate gas-liquid centrifugal

separation with various approaches, but following the universal steps of any simulation: geometry design, mesh generation, modeling set-up, and solution methods.

2.5.2.1. Geometry Design

Before starting a CFD simulation, a Computer-Aided Design (CAD) model must be developed as a virtual representation of the object. A CAD model, in principle, characterizes the solid features of the geometry. However, we need a model that characterizes the fluid features of the geometry to perform CFD. This model consolidates all the channels, paths, and spaces where fluid flows through the analyzed object. It is important to understand the difference between the solid and the fluid model. A solid model defines the real geometry of the object. It is a tangible tool manufactured in real life. As an example, it can be a stainless-steel pipe as shown in Figure 2.12-A. The fluid model defines the path the fluid follows within this object, which is not tangible in real life, as depicted in Figure 2.12-B. What matters for a CFD simulation is the fluid model. Hence, it is important to be familiar with the concept of generating inverted geometry.

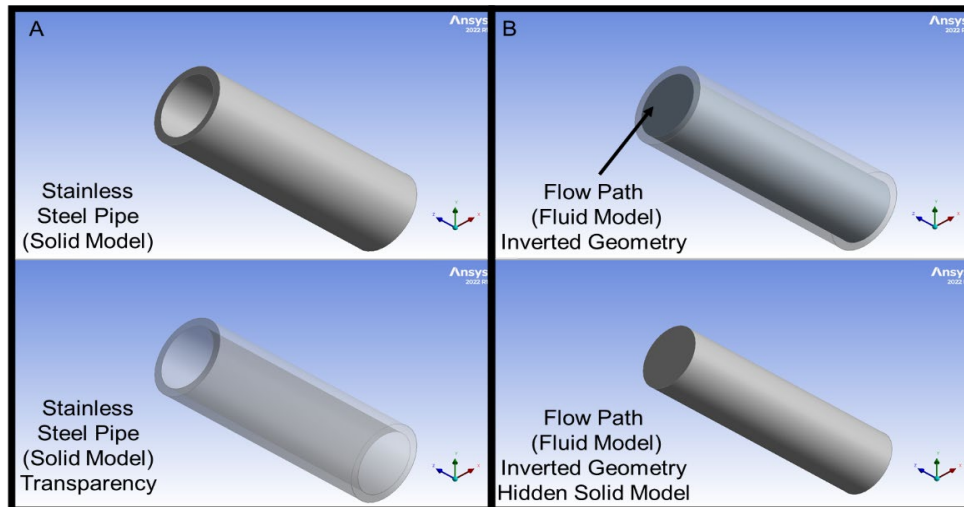


Figure 2.12. Inverted Geometry concept applied to a Stainless-Steel Pipe

Different software are specialized in CAD or CFD to model geometries. Depending on the type of design, proper CAD software must be chosen to correctly draft the features of interest within the analyzed separator. Suarez et al. (2005) and Abbariki et al. (2020) used a component of ANSYS Inc. called BladeModeler to accurately model turbomachine blades in the dynamic downhole centrifugal separators.

A well-structured and detailed geometry model contributes to the integrity of the simulation results. Geometry design is a stage where unimportant features can be neglected to simplify the geometry. Li et al. (2023) used GAMBIT2.4 to generate a simplified geometry for a static-type centrifugal downhole separator. In this simulation, they reduce the complexity of the calculations by replacing a gap between the casing and the separator's spiral section with boundary conditions (Li et al., 2023). Due to the complexity of some designs, a good practice is to create composed geometries, where a single model is divided into a certain number of bodies attached through a shared topology in a single part. This technique allows the user to use different types of meshes in each body and increase the quality, while reducing the computational load.

2.5.2.2. Mesh Generation

Meshing is the process by which a continuous geometry is discretized into a finite number of elements, also known as cells. Discretizing a domain or geometry of interest allows the user to calculate individual mathematical solutions for each cell. When all the solutions are combined, the result is an approximate solution for the whole continuous domain. Each element in the domain is connected to the neighboring elements sharing edges and corners, also known as nodes. Meshes are done for either 2-D or 3-D geometries, with various elements. They can be divided into structured meshes, which exhibit well-known arranged patterns. Authors such as Zhou et al.

(2018), Wang et al. (2020), and Abbariki et al. (2020) used structured meshes in their simulations, employing GAMBIT, ANSYS ICEM 14.5, and ANSYS TurboGrid, respectively. Another meshing type is unstructured meshes, which randomly fits any geometry, providing flexibility without following a uniform pattern. This mesh type is usually combined with structured mesh using composed geometries. Authors such as Wang et al. (2018), Zhang et al. (2018), Kou et al. (2022), and Li et al. (2023) adopted hybrid mesh models to reduce the number of cells and facilitate meshing of complex geometries.

One of the most useful techniques in the past decade is patch-conforming method, where the meshing process starts from the edges and faces of the geometry, taking a 2-D approach, and then moving into 3-D towards the volume. This approach has been used in the literature by Darbani et al. (2015) and Derakhshan et al. (2018). The technique is followed by the most recent version of the Watertight method used by ANSYS Fluent Meshing. Figure 2.13 displays the types of elements generated by different ANSYS Inc. meshing components.

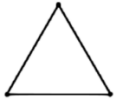

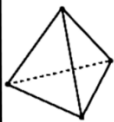
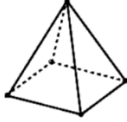
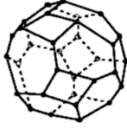
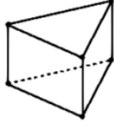
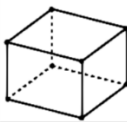
	Unstructured Elements	Structured Elements
2-D	 Triangle	 Quadrilateral
3-D	 Tetrahedron  Pyramid  Polyhedron	 Prism/Wedge  Hexahedron

Figure 2.13. Element types. Adapted from ANSYS Fluent User Guide.

Meshes need to be especially finer near the areas where large pressure gradients are expected, known as boundary layers. Nowadays, most software include techniques that capture the physics of flow to mesh these boundaries. Qui et al. (2019) and Olaleye et al. (2022) stated in their

researches that the finer meshes should only be applied in the critical regions (or composed bodies), like walls, vortexes, spirals, inlets, or outlets. Figure 2.14 displays a hybrid grid on a composed geometry. The Figure shows the meshes on two inducer and separator bodies with hexahedral structure elements. Meanwhile, the crossover was meshed with tetrahedral unstructured elements.

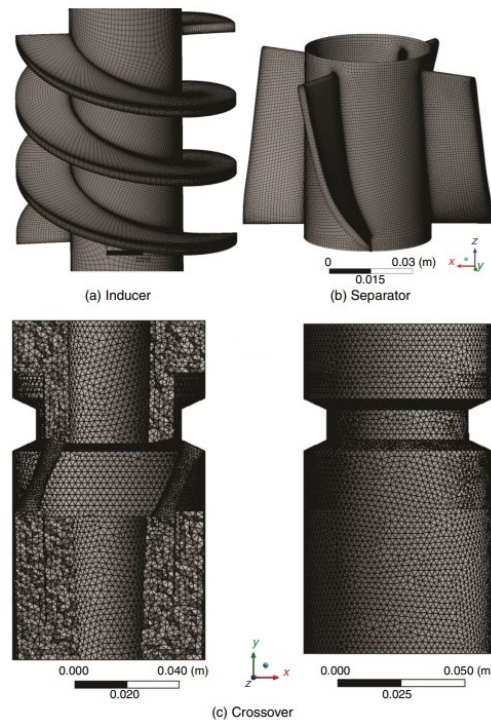


Figure 2.14. Hybrid mesh for a dynamic centrifugal downhole separator (from Abbariki et al. 2020)

While meshing, one must consider the number of cells and the effect of discretization on the simulation capability. The larger the number of cells is, the more accurate the solution will be, but also, the more computational time will be consumed. Meshing the domain with a finer grid is tempting when seeking more precise results. However, coarse grids do not mean less accurate results. There is a balance, and a sensitivity analysis must be conducted to understand when the results start depending on the mesh size. This analysis is called Grid Independence, where the same simulation is run with several mesh sizes, and the results are compared to understand when the

mesh size truly affects the outcome. The coarser the mesh is without reducing the quality of the results, the better, as the simulation time decreases.

2.5.2.3. Modeling Set Up

The modeling set-up for a problem encompassing fluids must be performed in a CFD software. This software or solver includes all the necessary selections of physical models and governing equations influencing the case of study. In addition, material selection and boundary conditions are important and must be determined in this solver.

2.5.2.3.1. Physical Multiphase Models

CFD simulations allow users to mimic a wide range of phenomena with various options and combinations. The solver simulates steady conditions, where flow does not change over time, or transient conditions, where the flow does not stay constant and varies over time. This flow may be affected by different physical models that must be determined and added to the simulation to obtain meaningful results. ANSYS Fluent 2022 R1 has the following models that can be added to any phenomenon being simulated: Multiphase, Energy, Viscous, Radiation, Heat Exchanger, Discrete Phase, Solidification and melting, Acoustics, Structure, Eulerian Wall Film, Potential/Li-ion Battery, and Battery Model.

Gas-liquid centrifugal separation is a multiphase phenomenon because more than one phase affects the process. The multiphase modeling type must be activated. In addition, viscous modeling needs to be activated as the studied phenomenon deals with fluids, and the solver must account for the effects of fluid viscosity on flow behavior. Many authors have simulated this phenomenon in the literature and selected different model combinations to achieve realistic results.

Multiphase Flow modeling comes with some sub-models that must be carefully chosen to represent the flow properly. There are two approaches to solving multiphase flow problems: the Euler-Lagrange and Euler-Euler. The Euler -Lagrange approach is used in Discrete Phase Modeling (DPM), also known as particle model. This approach treats the fluid as a continuum, while the dispersed phase is tracked through the flow field. The dispersed phase can be particles, bubbles, or droplets (ANSYS Fluent Theory Guide, 2022). Darbani et al. (2015), Zhou et al. (2018), and Zhang et al. (2018) used this type of modeling to simulate a dynamic separator and an axial separator. Zhang et al. (2018) used this method due to the low liquid fractions in their simulations compared to gas, tracking the liquid droplets as a dispersed phase.

The Euler-Euler approach treats the different phases as interpenetrating continua. In ANSYS Fluent, there are three sub-models based on this approach: the Volume-of-Fluid (VOF) Model, the Mixture Model, and the Eulerian Model. The VOF Model simulates the behavior of multiple immiscible fluids by tracking the volume fraction of each fluid in each computational cell (ANSYS Fluent Theory Guide, 2022). Meng et al. (2020) used this model in their simulations for a spiral separator meant to separate solid particles from gas-liquid, due to the fluid forming a free surface during the separation, which is known as a surface with zero shear stress like the gas-liquid interface. The VOF model has also been used by other authors trying to simulate fluid-solid separation, or cases where the interface between fluids or particles is of interest for the study. However, it is not a desirable technique to simulate gas-liquid separation.

The Mixture Model treats the multiphase flow as a single continuous fluid with averaged properties, allowing simulations of dispersed phases without tracking individual particles (ANSYS Fluent Theory Guide, 2022). Olelaye et al. (2022) and Kou et al. (2022) simulated tangential and

axial separators with this model, respectively. The mixture model is suitable for cases with good mixing between the fluids, like cyclone separators (Kou et al., 2022).

Lastly, the Eulerian Model considers all the phases in the problem analyzed continuously, making it the most complex of the multiphase models. Kharoua et al. (2016), Derakhshab et al. (2017), and Abbariki et al. (2020) simulated the equipment in their research using the Eulerian Model. According to Abbariki et al. (2020), it is essential to use the Eulerian Model when dealing with centrifugal separation, because the forces related to difference in phase densities are applied. As the Eulerian Model uses separate sets of momentum equations for each phase, it predicts the phenomenon's physics more accurately.

Some sub-models and parameters can be activated inside each model to improve the simulation. For instance, Suarez et al. (2005) used a multi-fluid model available within the Eulerian Model to simulate a downhole dynamic gas-liquid centrifugal separator. Further, Wang et al. (2018) used the Population Balance Model (PBM) available for Mixture and Eulerian Models to simulate dynamic separators. This model was used to account for the fragmentation and coalescence of bubbles or droplets in the flow domain, as it uses a mathematical framework to describe the distribution of the dispersed phase sizes (Wang et al. 2018).

2.5.2.3.2. Physical Turbulence Models

Modeling the turbulence is the second important phenomenon after multiphase modeling. In ANSYS Fluent, turbulence modeling is known as viscous modeling. This modeling approach seeks to solve the turbulence in the flow domain. Some phenomena can be considered laminar, when the fluids flow in parallel streamlines and there is no chaotic behavior. Centrifugal separation

is a phenomenon entailing chaotic features, and the flow must be described as turbulent. The CFD software comes with several models to solve the flow turbulence, as seen in Figure 2.15.

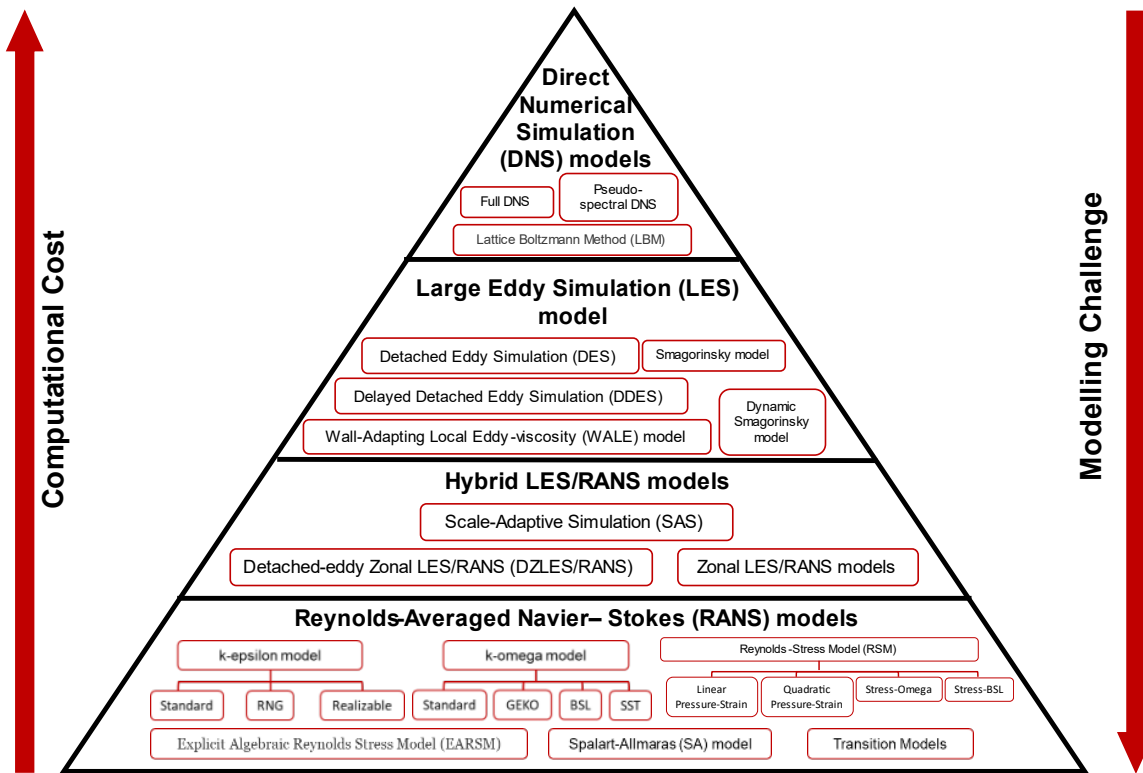


Figure 2.15. Turbulence models' hierarchy

Turbulent flows are characterized by chaotic and unpredictable fluctuations in flow characteristics, such as velocity and pressure. Due to the complexity of the physics, analytical solutions are highly difficult, if not impossible, to obtain, and numerical solutions must be implemented instead. This challenge has slowly been overcome by mathematical models solved through numerical methods. Turbulent models can be classified into Reynolds-Averaged Navier-Stokes (RANS), Large Eddy Simulation (LES), Hybrid Models (LES/RANS), and Direct Numerical Simulation (DNS).

The RANS models provide a time-averaged solution for the governing equations of the steady and unsteady fluid flows. This approach simplifies the computational requirement, but loses

information during the iterations. This is due to the modeling assumptions used to derive the mathematical formulation of the model. There are several types of RANS Models. Each model has assumptions that work better for some specific phenomena. In the literature, Suarez et al. (2005), Darbani et al. (2015), Wang et al. (2018), Meng et al. (2020), Wang et al. (2020), and Olaleye et al. (2022) used the k-epsilon model to simulate different types of centrifugal separation. The k-epsilon model is a two-equation model that describes the turbulence employing two transport equations: the turbulent kinetic energy (k) and the rate of dissipation of turbulent kinetic energy (ϵ). This model is the most employed technique in engineering for CFD (Wang et al., 2018). It can be used when not much data is known on the flow physics (Suarez et al., 2005). Meng et al. (2020) used the RNG k-epsilon model due to its stability when dealing with phenomena with high strain rates caused by curvature, acceleration, and separation. This model can improve the prediction in the boundary layers. According to Olaleye et al. (2022), the presence of the epsilon term gives accuracy to simulate fast flows.

The k-omega model is a RANS model that attempts to predict turbulence through two partial differential equations for the turbulence kinetic energy (k) and the specific dissipation rate (ω). This model has been employed to predict the physics of centrifugal separation by some authors, such as Kharoua et al. (2016), Derakhshan et al. (2017), and Abbariki et al. (2020). The authors used the SST sub-model for their simulations. SST stands for Shear-Stress Transport and is particularly well-suited for simulating complex flows, such as separation.

The Reynolds-Stress Model is another RANS model widely used in the literature. Authors such as Zhou et al. (2018), Zhang et al. (2018), and Kou et al. (2022) have successfully implemented the method in their simulations. This model is more advanced than k-epsilon and k-omega in accounting for the effect of stream curvature, rotation, and swirl (Kumar Shukla et al.

2011). It solves for the components of the Reynolds stress tensor that directly represent the turbulence-induced fluctuations in the momentum equations. This difference allows the RSM to capture the interactions between different turbulence components and provides a more detailed understanding of turbulence behavior. According to Kou et al. (2022), this model fully considers changes in the surface curvature necessary for swirling flow.

Besides the RANS model, LES models are popular. LES models are averaged between RANS and DNS, where the largest turbulence scales containing the most energy are resolved directly, using DNS models. Meanwhile, the smallest turbulence scales are modeled through RANS models. These turbulence scales, or eddies, are swirling motions or vortices within a fluid. In LES, eddies are solved directly, and a spatial grid is necessary to capture details of interest using a solver and discretization scheme, increasing the computational cost. Zhou et al. (2018) particularly mentioned the benefits of using LES models for centrifugal separation simulation but warned that these models need a highly fine mesh to achieve precision. When this feature is provided, the simulation time increases considerably. The authors used the RSM model instead.

The most computationally heavy model with no simplifications is the DNS. This method does not rely upon any turbulence model, but directly solves the entire range of eddies. It is considered the most accurate method for simulating turbulent flow, but it is limited to low Reynolds numbers or simplified geometries due to its computational requirement. This method was not implemented by any authors conforming to this literature review. Table 2.2 summarizes the authors and the physical models implemented to simulate gas-liquid centrifugal separation.

Table 2.2. Physical Models used by different authors in the literature

Author	Multiphase Flow Modeling				Turbulence Modeling			
	Euler-Euler Approach			Euler-Lagrange Approach	k-epsilon		k-omega	RSM
	VOF	Mixture	Eulerian	DPM	Std.	RNG	SST	
Suarez et al., 2005			Yes		Yes			
Darbani et al., 2015				Yes	Yes			
Kharoua et al., 2016			Yes				Yes	
Derakhshan et al., 2017			Yes				Yes	
Wang et al., 2018			Yes		Yes			
Zhuo et al., 2018				Yes				Yes
Zhang et al., 2018				Yes				Yes
Meng et al., 2020	Yes					Yes		
Wang et al., 2020			Yes			Yes		
Abbariki et al., 2020			Yes				Yes	
Olaleye et al., 2022		Yes				Yes		
Kou et al., 2022		Yes						Yes

2.5.2.3.3. Selection of Material and Phases

The type of fluids that are being simulated must be chosen with correctly assigned properties, such as density and viscosity. Other properties, such as thermodynamic properties, may be necessary depending on the phenomenon being analyzed. Nonetheless, density and viscosity are enough to simulate the gas-liquid separation phenomena. Most authors in the literature used water and air as liquid and gas, respectively, to perform simplified simulations. Some others, such as Kharoua et al. (2016), simulated oil with a density of 685.31 kg/m^3 and a viscosity and 0.369 mPa.s , and gas with a density of 27.14 kg/m^3 and a viscosity of 0.0129 mPa.s . Furthermore, Kou et al. (2022) used air as the gas phase, in a mixture with an oil with a density of 850 kg/m^3 and a viscosity of 30 mPa.s . When selecting the materials and phases, the user must decide on primary (continuous) and secondary (dispersed) phases. Features such as the dispersed phase diameter,

which is the diameter of the bubbles, droplets, or particles set as secondary (dispersed) phase, and phase interaction forces (drag, slip velocity, and surface tension) are defined in this stage, where drag is the force opposite to the direction of the motion, the slip velocity is the different velocity of fluids in the same domain, and surface tension is the force that causes phenomena such as capillary action and the formation of droplets.

2.5.2.3.4. Boundary Conditions

Boundary conditions are a set of constraints or specifications applied to the computational domain's edges or faces. These conditions determine how the control volume interacts with the surrounding environment. These conditions highly impact the results. Poor choices in boundary conditions might lead to solution divergence. There are several types of boundary conditions that can be applied to a set of geometrical features, such as inlets, outlets, and walls. Some boundary types are fixed-velocity, pressure, or mass flow for inlets or outlets, inlet or outlet vents, outflows, intake fans, symmetries, and walls. Authors have used different boundary conditions in the literature to simulate gas-liquid centrifugal separation. Table 2.3 summarizes the boundary conditions used by some authors.

Table 2.3. Boundary conditions used by some authors in the literature

Author	Year	Boundary Conditions			
		Inlet	Outlets	Wall	Blades
Suarez et al.	2005	Pressure and GVF	Fluid Velocity and GVF	Non-slip	Non-slip and rotation velocity
Darbani et al.	2015	Pressure and GVF	Liquid Outlet: Mass flow Gas Outlet: Pressure	Non-slip	Non-slip and rotation velocity
Kharoua et al.	2016	Velocity and GVF	outflow	Non-slip	-
Derakhshan et al.	2017	Pressure and GVF	Liquid outlet: mass flow rate Gas Outlet: Pressure	Non-slip	Non-slip and rotation velocity
Zhang et al.	2018	Velocity	Liquid outlet: pressure Gas Outlet: escape	trap	-
Wang et al.	2020	Velocity	Pressure	-	-
Abbariki et al.	2020	Pressure and GVF	Liquid outlet: mass flow Gas Outlet: pressure	Non-slip	Non-slip and rotation velocity
Kou et al.	2022	Velocity	Free outflow	Non-slip	-

2.5.2.4. Results

This section discusses the results and conclusions in the literature about downhole centrifugal separators. It is observed that the head affects the separator's performance considerably (Suarez et al., 2005), as mentioned before, when discussing the parameters influencing gas-liquid separation. The length of the separator was studied by some authors (Suarez et al. 2005), who stated that the location of the crossover section, bottom section of a rotational separator, and the sizing of its outlets greatly impact the performance, as inducers need to generate enough head to overcome pressure losses. Derakhshan et al. (2017) concluded this variable by stating that a large length guarantees enough retention times to achieve good separation. They performed a sensitivity analysis with different lengths (60, 90, 120, and 150 mm), determining that 90 mm was the optimal length. They estimated, as well, that the optimum number of gas outlets was four. Zhou et al. (2018) concluded that the separation can be improved with a shorter length of the separator if the rotational vane or blade angles are modified. They suggested optimum values of 22 to 25°.

Other sensitivity analyses were conducted with different design features. Derakhshan et al. (2017) found that reducing the number of blades and thickness improves the separation

performance. Furthermore, increasing the clearance results in poor performance as the head loss increases and fluid escapes the rotational path. This last conclusion contradicts the remarks of Abbaraiki et al., observing that the increase in the tip-clearance gap decreases the flow losses, increasing efficiency. Abbaraiki et al. (2020) concluded from their workover vortex-type separators that the efficiency increases when changing the inlet angle, blade length, and tip-clearance gap.

Temperature and viscosity analysis was performed by some authors. Darbani et al. (2015) found that in high viscosities, the efficiency decreases with the increase in GVF. They also compared this phenomenon between two separators and found that this phenomenon is amplified in vortex-type separators, compared to paddle wheel separators. Darbani et al. (2015) mention in their study that paddle wheel separators perform better than vortex separators. Derakhshan et al. (2017) came to a similar conclusion, observing that increasing the temperature improves the separator's performance at low flow rates.

Authors like Kharoua et al. (2016) discussed the separator's performance by setting outflow boundary conditions. They observed that the pressure drops increase with the outflow increase. The effects of different outflow conditions on the separators can be seen in the downstream sections. Suarez et al. (2005) observed the segregation of the fluids in the centrifugal section in their simulations. They pointed out the importance of knowing how large the gas-liquid transition zone is, which varies with GVF, for the separation performance. Darbani et al. (2015) observed that the concentration of gas in the center of the centrifugal vortex is higher for paddle wheel than vortex separators. They concluded that high flow rates result in high turbulence and low retention times and contribute to low efficiency. Abbariki et al. (2020) stated a similar idea when saying that the liquid does not have enough time to separate by increasing the flow rate. They also pointed out

that gas is drawn to the liquid outlet at high flow rates because of the drag force of the liquid. Furthermore, Derakhshan et al. (2017) concluded that the bubble size reduces the head, and if the bubble diameter is reduced, the gas dispersion will increase.

All the separators evaluated through CFD, which this literature review compiled, are dynamic downhole centrifugal or surface separators. This study used the learning mentioned to simulate a novel static centrifugal separator. Additionally, it was observed that engineers mainly use two evaluation methods for performance prediction. This situation allows for the inclusion of a new method based on machine learning and data analysis, an area of study that has been largely advanced in the past decade. This study presents an initial effort to set up a new evaluation method as an algorithm.

CHAPTER 3: CFD SIMULATIONS

This Chapter describes the geometry construction, meshing, simulation set-up, and results for a static downhole centrifugal separator, used for gas-liquid separation in oil and gas wells. The equipment was laboratory-tested by Olubode (2021) at the Well Construction Technology Center of the University of Oklahoma. The CFD simulation is performed to understand the physics governing the fluid flow in the equipment, gas-liquid separation phenomena, and the separator's performance under specific boundary conditions.

3.1. Geometry Design

The analyzed gas-liquid separator was experimentally studied by Olubode (2021). Figure 3.1 displays the static downhole centrifugal separator. The equipment has a bottom inlet supplied by upstream tubing, where a gas-liquid mixture enters the domain. This mixture is then forced and diverted into two helix-type paths opposite to each other, shown in green and red. After passing through the helix and getting imposed to the centrifugal force, the liquid is separated and sent down to the bottom of the equipment. It then enters two exit ports opposite to each other, shown in red. These exit ports conduct the separated liquid to the liquid outlet, subsequently connected to a downstream tubing or a pump. Meanwhile, the gas is supposed to flow up and exit from the top of the domain. The main purpose of this separator is to help downhole pumps, such as sucker rod or electrical submersible pumps, work under full liquid fillage.

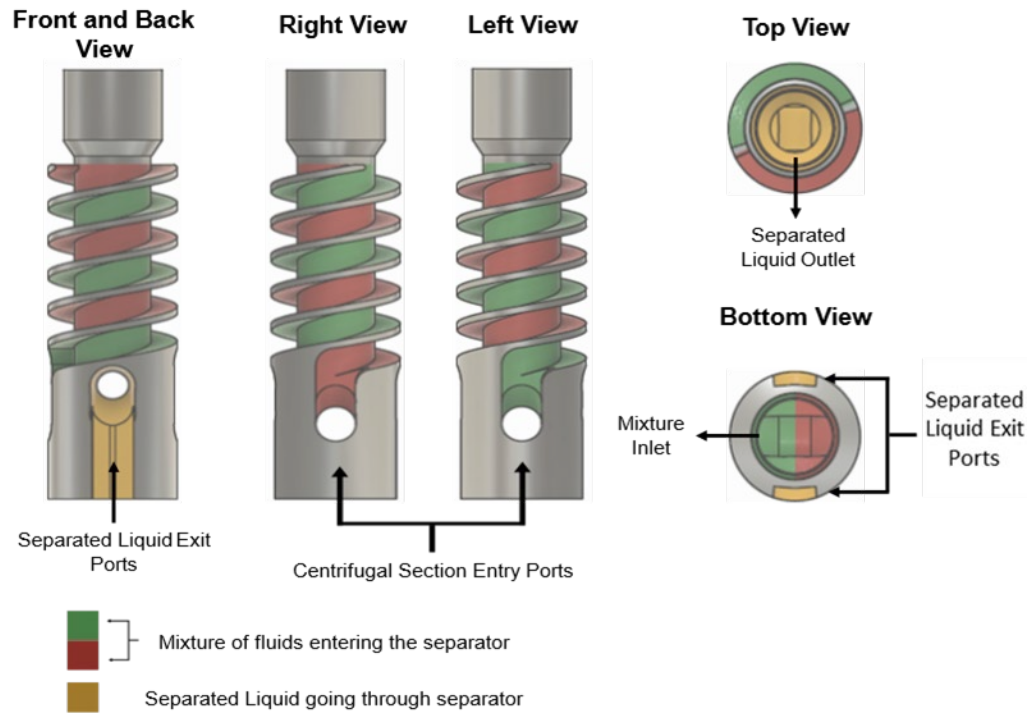


Figure 3.1. Schematic of the static downhole centrifugal separator (Olubode et al. 2021)

The gas-liquid separation in this equipment needs the assistance of shroud and casing pipes as it counts on a reverse flow technology assisted by gravity to accomplish separation. Figure 3.2. displays the separation mechanism used by the downhole separator. The mixture is extracted from the reservoir and pulled into an upstream tubing. The mixture then enters the separator through the inlet at the bottom of the equipment. It is diverted into two helix-type paths that generate centrifugal force. The separator is fixed into a shroud pipe, which covers the helix-type paths (green and red in Figure 3.2) and ends right at the top of the separator. Once at the top of the helix-type paths, the partially segregated fluids are expelled to the casing-separator annulus. The impingement of the liquid on the casing wall and the gravity effect causes the liquid to flow down the annulus while the gas flows up, finding its way to the surface through the casing-tubing annulus. The liquid falls through the shroud-casing annulus, gets sucked into the bottom part of the shroud, and is forced into two liquid exit ports (yellow in Figure 3.2). These ports conduct the

liquid to the center of the separator, into the separator's body (dotted lines) and to a downstream tubing connected to a pump.

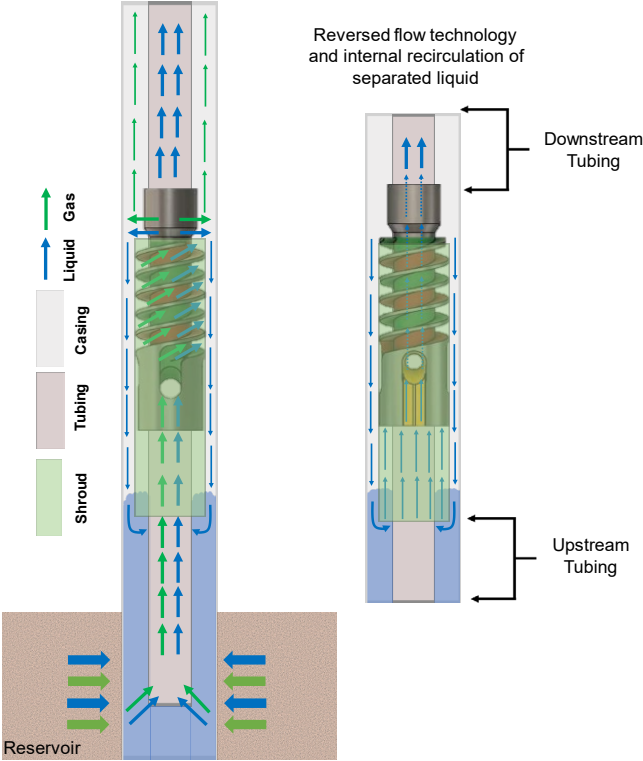


Figure 3.2. gas-liquid separation system schematic

3.1.1. CAD Model

The geometrical models used for this thesis were designed using the Design Modeler module in ANSYS Workbench 2022 R1. The system shown in Figure 3.2 was simplified to be numerically simulated in ANSYS Fluent. As shown, the control volume was selected to shorten the domain, limiting it to only the space where the fluid is being analyzed. Besides the separator, tubing, shroud, and casing pipes were modeled to represent the separation system correctly.

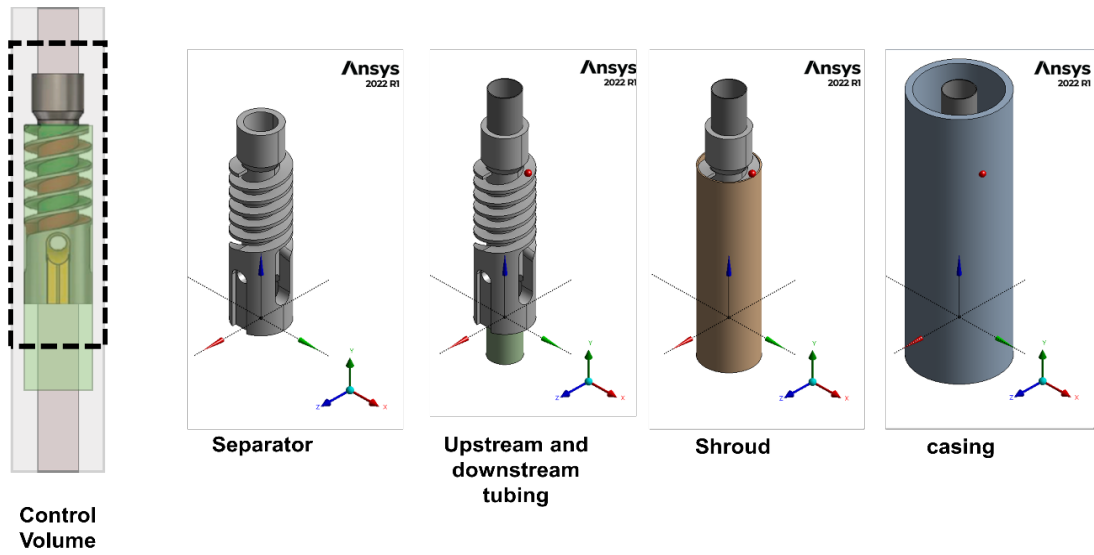


Figure 3.3. Numerical simulation control volume

For further simplification of the problem, the downstream tubing, the inner channel of the separator, and the liquid exit port were plugged. With this approach, the gas-liquid separation system is reduced to an inlet, and two outlets: a top outlet where successfully separated gas is expected to leave the domain and a bottom outlet where successfully separated liquid falls with a reverse flow mechanism. Figure 3.4 displays the further simplified schematic of the system.

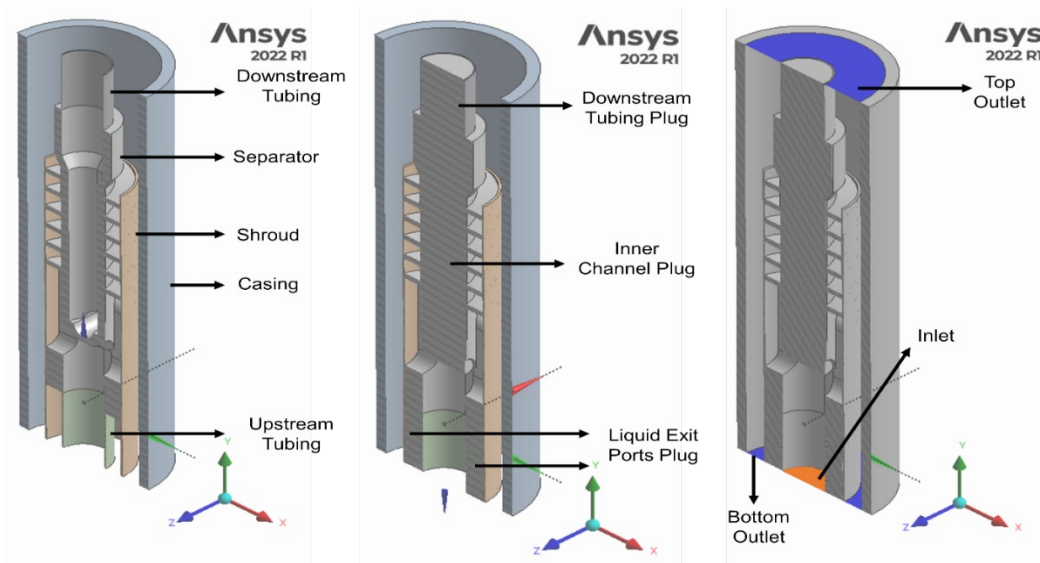


Figure 3.4. Solid geometry simplification (cross-sectional view)

After defining the solid geometry, the inlet and outlets were capped, and an inverted geometry was extracted. This new geometry is the fluid domain, representing the volume where the liquid and gas flow. Figure 3.5 displays the fluid domain geometry. This geometry is the only needed domain to perform CFD simulations, and the aforementioned solid body can be disregarded. The geometry was divided into different bodies for meshing and analysis.

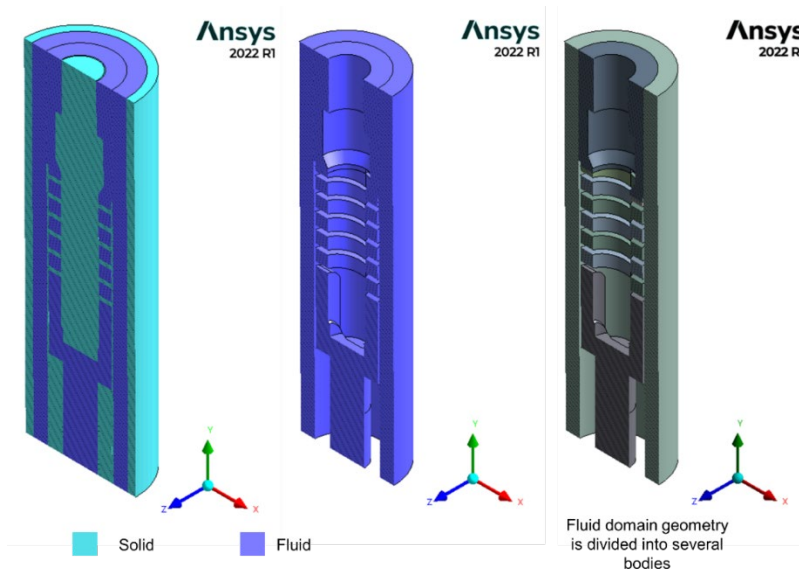


Figure 3.5. Inverted Geometry: Fluid domain (cross-sectional view)

After having the fluid geometry, name selections were given to specify the domain's boundaries. This CAD model is described as a conformal geometry divided into seven bodies, one inlet, and two outlets. Table 3.1 shows the descriptions of the boundaries in the geometry.

Table 3.1. Descriptions of the Geometry Boundaries

Boundary	Shape	Area (in ²)	Area (m ²)	Relative Diameter (in)	Relative Diameter (m)	Hydraulic Diameter (m)
Inlet	Circle	3.80	0.00245	2.20	0.056	0.056
Bottom Outlet	Annulus	14.42	0.00930	4.28	0.109	0.046
Top Outlet	Annulus	27.47	0.01772	5.91	0.150	0.097

Figure 3.6 displays the final CAD model with the fluid geometry. The front, top, and bottom views, planes with features of interest, and boundaries are shown in the schematic.

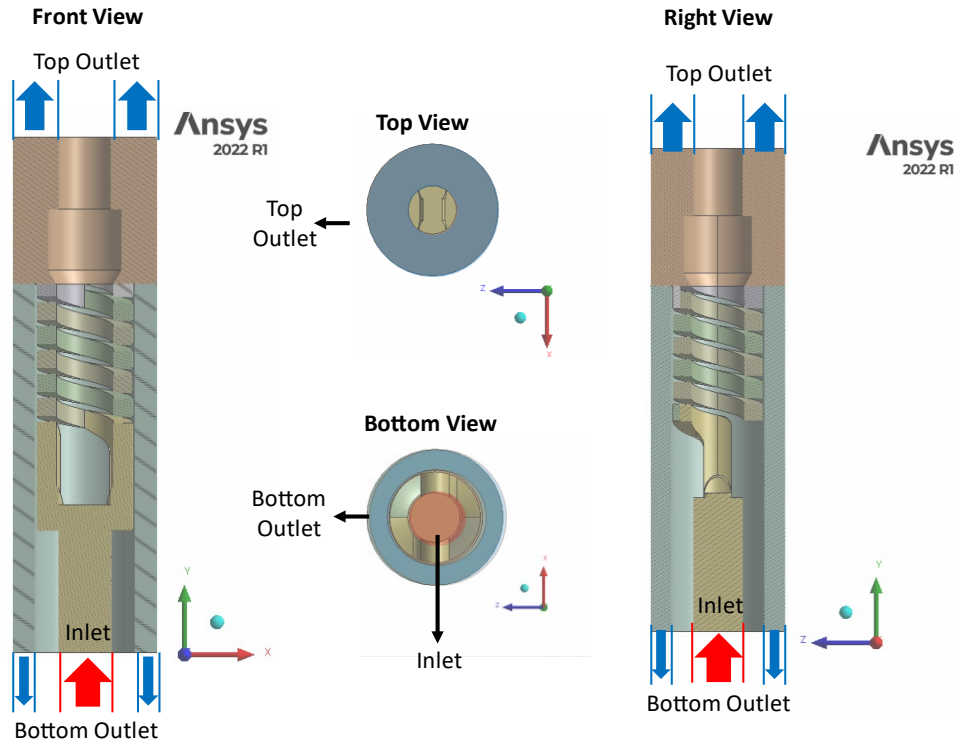


Figure 3.6. Final CAD Model

3.2. Meshing

The meshes or the grids for the CAD model were generated using the Watertight Geometry workflow from ANSYS Fluent. The following contemplations were considered to generate a high-quality mesh: local and global surface meshing, volume meshing, and boundary layers. Depending on the size and quantity of these cells, the number of the grids may increase or decrease. Meshes with a larger number of cells are more robust. Hence, it is more likely to achieve simulation convergence, and the results are more accurate. However, the simulation time increases substantially. A careful approach must be taken to generate a well-balanced mesh with an optimum number of cells.

25 types of meshes were generated for this project, testing different combinations of features for each to achieve meshes with acceptable quality. The considered features while meshing are briefly described below:

- **Cell Size (target mesh size, minimum size, maximum size, and maximum cell length):**
 The cell size requirements change depending on if a surface global mesh (min size and max size), a surface local mesh (target mesh size), or a volume mesh (max cell length) is applied. The three features seek the same information to create the size of each cell, discretizing the domain. This number is the value with the most meaningful effect on the number of cells created. Figure 3.7 displays the difference between two of the meshes generated. By changing the cell sizes, the total number of cells reduces from over 8 millions to only 68 thousands. The question is whether the simulation accuracy reduces because of this change or not.

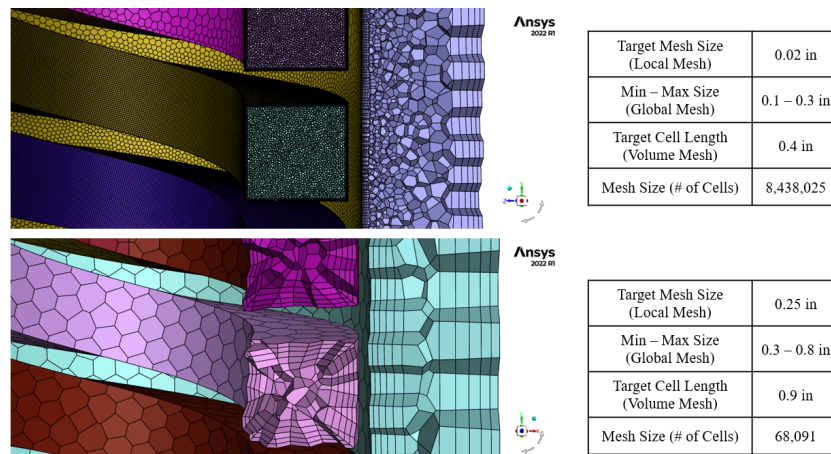


Figure 3.7. Impact of cell size in the mesh

- **Growth Rate:** It is used in surface and volume meshing, specifying the size increase in element edge length with each subsequent layer of elements (ANSYS). In other words, it measures how large the elements in the center of a domain become, as the elements

are generated from the outside (walls, edges, or faces) to the inside. Figure 3.8 displays how a mesh looks, depending on the growth rate. The smaller the value, the more populated the meshes are in the middle zone. This feature is also used for the boundary layer application. It specifies the growth rate for a layer compared to the layer immediately before it. Figure 3.9 displays the boundary layer descriptions for meshes with three growth rates. Again, the smaller the growth rate, the smaller the meshes are in the middle of the boundary layer.

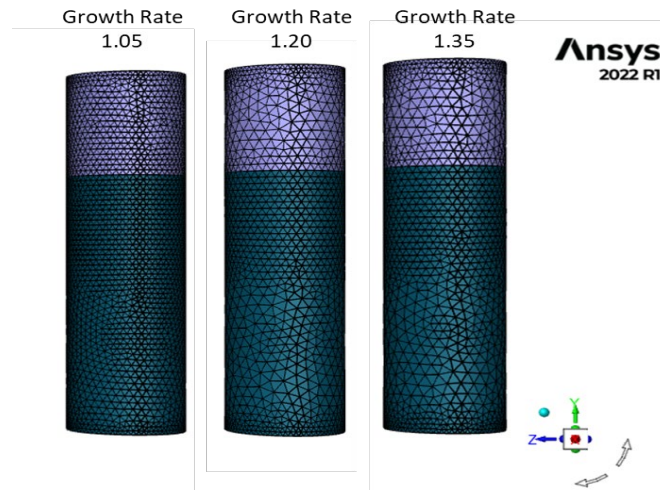


Figure 3.8. Growth Rate impact in mesh generation

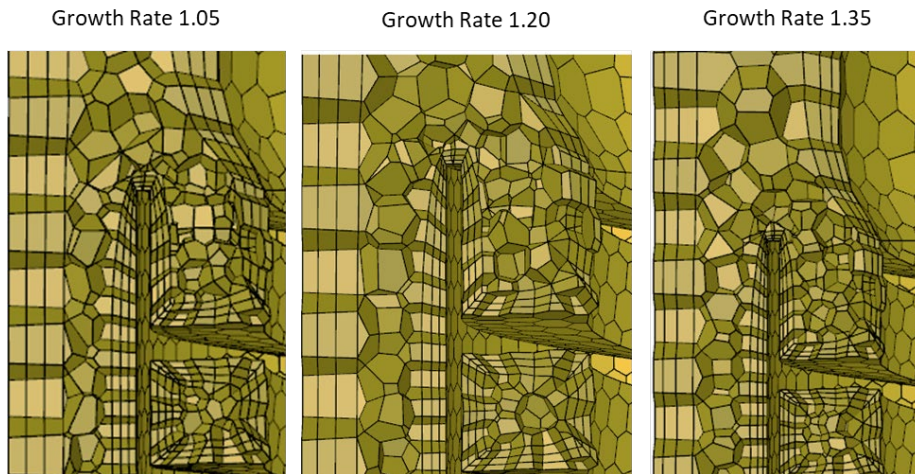


Figure 3.9. Growth Rate impact on boundary generation

- **Boundary Layer:** boundary meshing refers to discretizing the surface that defines a computational domain's boundary. Particularly for walls, it is important to implement boundary layer meshing, as significant gradients occur in these zones. Different types of boundary layers were used to generate the meshes in this study, including smooth transition, uniform, last ratio, and aspect ratio. Figure 3.10 shows the differences between these types. Additionally, the number of layers can be defined. For example, Figure 3.10 shows a boundary layer mesh with 3 layers. The final mesh used in this study used 5 layers.

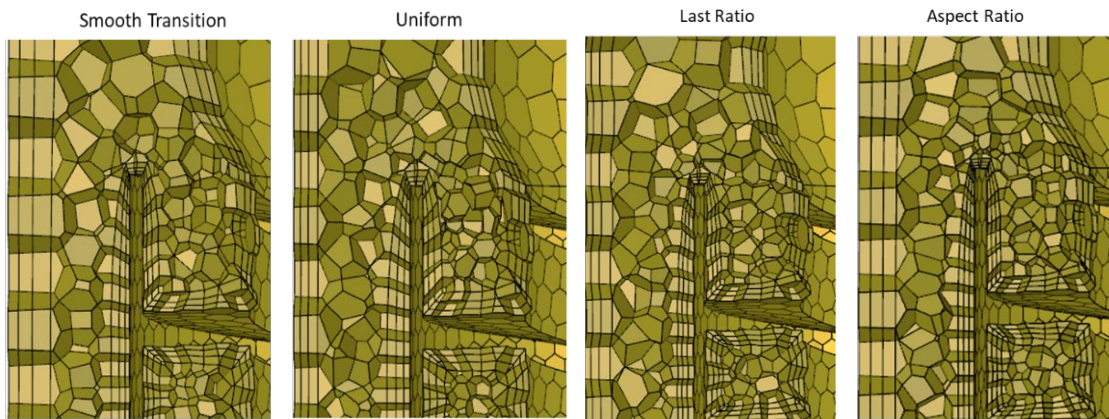


Figure 3.10. Boundary layer types tested in meshing analysis

Several combinations of the above features were used to generate the different meshes used for this study. The better the meshing quality, the higher the chances to minimize numerical errors and accurately represent the physical flow models. Each mesh's quality was assessed using orthogonality, aspect ratio, and skewness. These measurements are briefly described below:

- **Orthogonality:** This measure can be between 0 and 1, with 1 meaning excellent and 0 meaning poor orthogonality. The mesh consists of lines or elements dividing or discretizing the fluid domain into smaller regions. The orthogonality is excellent if

these lines meet at right angles (90 degrees). The further the angle is from 90 degrees, the poorer the orthogonality quality will be.

- **Skewness:** Like orthogonality, this measure varies between 0 and 1, with 0 showing excellent and 1 showing poor skewness. It measures the deviation of an element from its ideal shape by quantifying how far the angles of the element are from their ideal values.
- **Aspect Ratio:** Unlike orthogonality and skewness, aspect ratio does not have a range. It can take a value no less than 1, making 1 a perfect aspect ratio. It measures the elongation of elements in a mesh, defined as the ratio of the longest side to the shortest side of a given element.

After considering the above quality measurements, six meshes with varying element sizes were pre-selected to run a grid independence study. This study is a sensitivity analysis to assess the resolutions of the meshes and select the one that provides accurate values with the least number of cells.

3.2.1. Grid Independence Study

Table 3.2 contains the size and quality measurement for all the meshes used in the grid independence analysis. Overall, it can be seen that the finer the mesh, the better the reported quality measurements are. According to ANSYS recommendations, meshes with orthogonality between 0.95-1.00 are considered excellent, and 0.70-0.95 orthogonalities are for very good meshes. These recommendations position the four finer meshes in an excellent category and the two coarser ones in a very good category. ANSYS recommends that meshes with skewness values between 0.00-0.25 are excellent. All the meshes studied here fall in this excellent category. Finally, as mentioned

before, the closer the aspect ratio is to 1, the better. ANSYS recommends avoiding aspect ratios over 10:1. As it can be seen, the lowest average aspect ratio achieved from the meshes is 7.14:1.

Table 3.2. Meshes used in Grid Independence Study

Mesh #	Mesh 1	Mesh 2	Mesh 3	Mesh 4	Mesh 5	Mesh 6
No. of Cells	68,091	79,337	152,446	285,475	548,004	1,176,440
Avg. Orthogonality	0.87	0.85	0.90	0.91	0.92	0.94
Avg. Aspect Ratio	7.14	6.72	6.30	5.90	5.44	4.93
Avg. Skewness	0.13	0.15	0.10	0.09	0.08	0.06

From Table 3.2, all the meshes have acceptable quality measurements. However, they must be subjected to a grid independence study to select a mesh small enough to perform the simulations at moderate times. Meanwhile, it must be verified that the solution with the selected mesh is accurate and does not depend on the mesh size.

The six selected meshes were used to conduct the same simulation case, with the same physical models and boundary conditions. The case was a transient single-phase flow where water was injected at 0.02 m/s (26.5 BPD) with the realizable k-epsilon and an enhanced wall treatment model. The outlets were set as pressure boundaries, and the Intensity and Hydraulic Diameter method was used to model the turbulence. The six cases were left to simulate 15 seconds of flow, while monitoring two variables: inlet pressure and flux. The flow time was enough for the solution to stabilize. The results reported below are the averages for the last 2 seconds of the simulations. Table 3.3 displays the values obtained for each of the six cases run, including the average (avg) and standard deviation (std) values for inlet flux and pressure. The computational time spent to simulate 15 seconds of flow is also reported for each case.

Table 3.3 Grid Independent Study Results For the Six Selected Meshes

Mesh #		Inlet Flux (Kg/s)	Inlet Pressure (Pa)	Simulation Time (h)
Mesh 1	avg	0.477	3037	1.65
	std	7.77E-16	0.09	
Mesh 2	avg	0.482	3052	2.32
	std	2.18E-14	0.07	
Mesh 3	avg	0.486	3086	2.59
	std	1.59E-14	0.34	
Mesh 4	avg	0.488	3098	7.06
	std	1.65E-14	0.53	
Mesh 5	avg	0.489	3087	15.25
	std	2.27E-14	0.54	
Mesh 6	avg	0.489	3076	43.89
	std	1.85E-14	0.97	

Table 3.3 summarizes the results of the grid-independent study. Going from the first to the sixth mesh, the results for inlet flux and pressure vary 0.012 kg/s and 61 Pa, respectively. At the same time, there is a difference of 42.24 hours in the simulation time between the finest (#6) and the coarsest (#1) meshes. The large simulation times show the necessity to select a mesh that does not take too long. Figure 3.11 displays the simulation time vs. number of cells, for the six tested meshes.

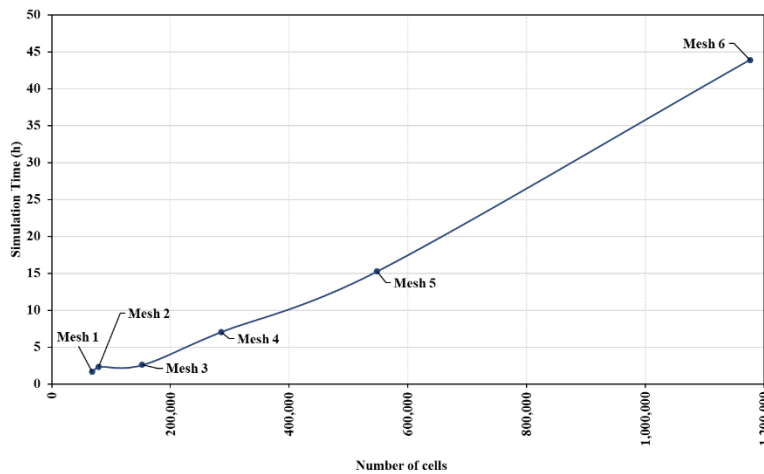


Figure 3.11. Simulation time (h) vs. Number of cells plot

The three coarser meshes have similar simulation times of less than 5 hours for the simulated case. The three finer meshes have drastically increased simulation times. The first three meshes are considered more suitable for the simulations of this study.

Figures 3.12 and 3.13 display the changes in inlet flux and inlet pressure for the six mesh sizes tested in this analysis. It is appreciated that the changes in the inlet flux become negligible for meshes 4, 5, and 6, where a plateau is observed. From this trend, it seems like mesh 4 can be a good mesh to use in the study. Nonetheless, the difference between mesh 4 and mesh 3 results is only 0.002 kg/s or 0.4% of the calculated flux. Considering this and the benefit of mesh 3 compared to mesh 4 in the simulation time, observed in Figure 3.11, it can be concluded that mesh 3 is a reliable and light mesh to simulate the cases of this study.

The inlet pressure results seem to increase from mesh 1 to mesh 3, and then fluctuate slightly between mesh 3 and mesh 6. Due to computational expense, no bigger meshes could be run to analyze the changes. Although mesh 4 reports a bigger value than all the meshes, meshes 3 to 6 have close values between 3076 and 3097 Pa, or only 0.68% difference. Any of these meshes are a good candidate to run the subsequent simulations. Mesh 3 was chosen to use for this study with a size of 152,446 cells, providing grid-independent results with shorter simulation times.

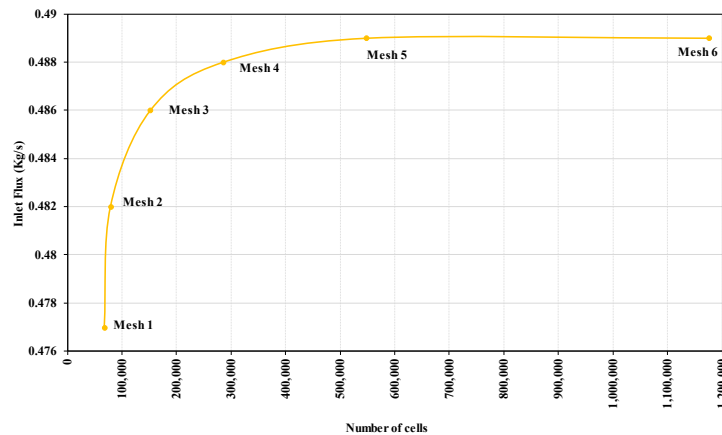


Figure 3.12. Inlet Flux (kg/s) vs. Number of cells plot

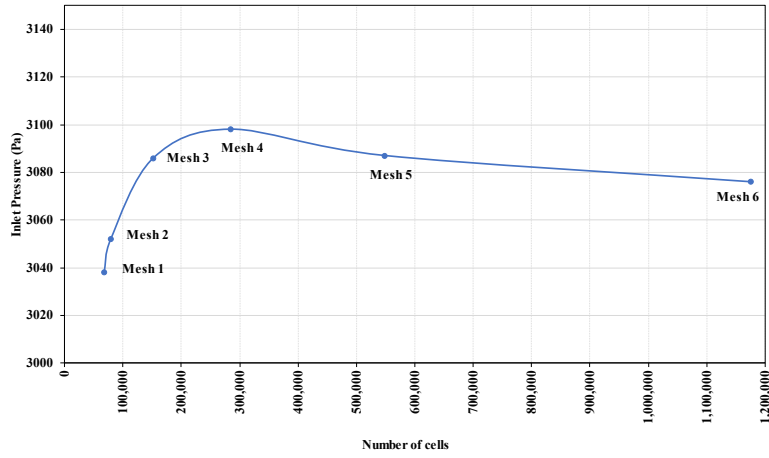


Figure 3.13. Inlet Pressure (Pa) vs. Number of cells

Table 3.4 describes the features of mesh 3, selected for the simulations of this study.

Table 3.4. Selected mesh characteristics

Local Surface Mesh	Growth Rate	1.2
	Target Mesh Size (in)	0.15
	Zone	Inlet, outlets, and helixes
Global Surface Mesh	Min Size (in)	0.2
	Max Size (in)	0.5
	Growth Rate	1.2
	Curvature Normal Angles	18
	Cells Per Gap	2
	Scope Proximity To	edges
Boundary Layer	Type	Smooth Transition
	Number of Layers	5
	Transition Ratio	0.272
	Growth Rate	1.2
Volume Mesh	Fill	polyhedra
	Growth Rate	1.2
	Max Cell Rate (in)	0.6
Size	152,446	

Some parameters seen in Table 3.4 are default values from the ANSYS Fluent meshing module, considered sufficient for the geometry meshing. Other variables, such as the cell sizes, are the results of the conducted sensitivity analysis where different values were tested. The boundary layer type is an important parameter to decide. As mentioned, four different methods can be used. The smooth transition type was selected as the most convenient for this study.

Significant changes may occur close to the wall regions, which are important to understanding the physics behind the fluid flow. Therefore, defining a good boundary layer method that refines the meshes in these zones is important. The smooth transition is a technique used to generate a boundary layer with a smooth and gradual transition. It calculates each initial height, or the height of the cells located next to the wall, and the total height, or the sum of the heights of the cells belonging to the boundary layer, to keep a smooth volume change rate. According to ANSYS, this technique is the most robust of all the boundary layer techniques, recommended for multiphase and swirling flows.

The y^+ is a crucial parameter to characterize the mesh resolution near a wall. It represents the normalized distance from the wall to the first grid point or the height of the initial cell. This parameter can be considered a quality measurement, indicating that the mesh accurately captures the fluid behavior inside the boundary layer. Depending on the desired quality, the y^+ can take the following values:

- $y^+ < 5$: represents finer meshes, used where resolving boundary layer phenomena is critical, such as high viscosity or low-speed flow cases. They are recommended for simulations involving heat transfer.
- $5 < y^+ < 30$: these middle-type meshes provide a good balance between accuracy and computational expense. They are suitable in most simulation cases.

- $y^+ > 30$: when the focus is on capturing larger-scale phenomena in a larger domain and the physics occurring near the wall is not of interest.

For this study, a y^+ value between 5 and 30 was considered enough. The weighted-average y^+ values in each of the domain walls for Mesh 3 are presented in Table 3.5. This table shows that none of the y^+ values surpass 30, indicating that the boundary layer is properly simulated. The names in the table correspond to the different bodies the main geometry was divided into.

Table 3.5. averaged y^+ values for the walls in the domain

Area-Weighted Average Wall Y^+	
expelling_section1:1	9.24
expelling_section2:1	9.01
wall_expelling_section	18.50
wall_expelling_section:1424	19.38
wall_helixes	11.35
wall_helixes:1417	11.37
wall_inlet	10.00
wall_outlet_bottom	7.24
wall_outlet_top	8.06

The final appearance of the selected mesh for this study can be observed in Figure 3.14. The local sizings for the inlet section, the bottom outlet, the top outlet, and the helx section are also shown in the Figure.

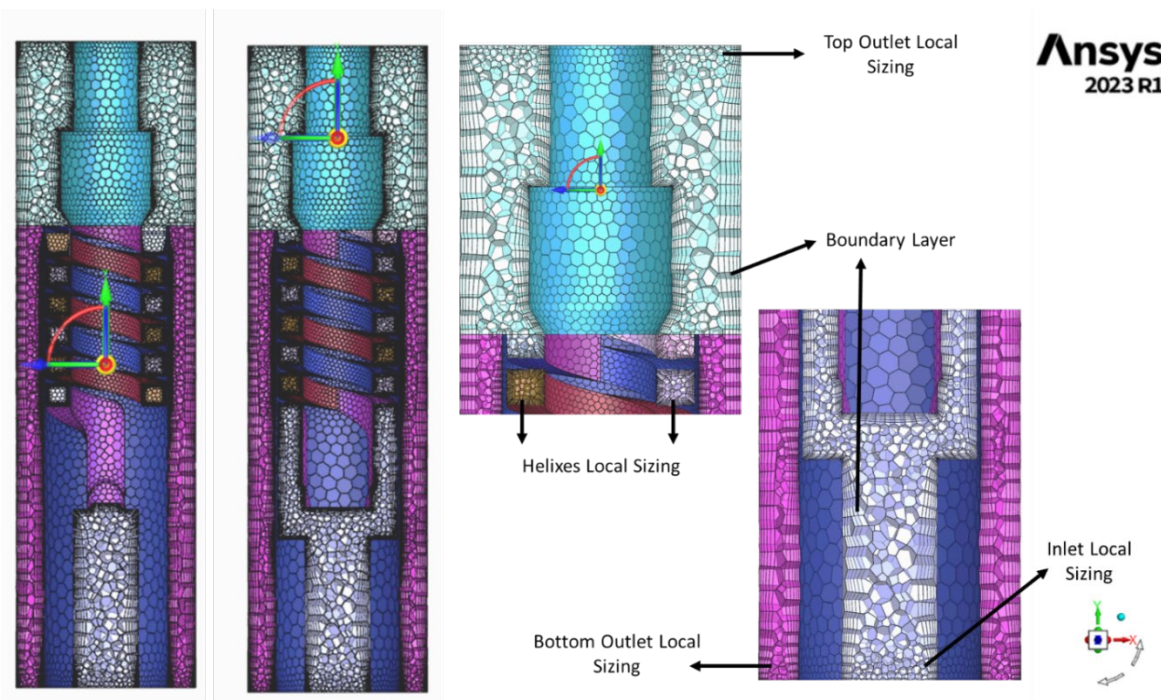


Figure 3.14. Final Selected Mesh

3.3. Modeling Set-up

Several study cases were simulated to understand the governing phenomena influencing the fluids inside the separator. These single-phase and multiphase study cases will be described below. The details of the modeling set-up used in this thesis is accounted as follows:

- **Pressure-based solver:** This type of solver considers the flow incompressible, where the density variations are considered negligible. This solver was selected to understand the physical phenomena at standard conditions without immersing the study in the effects of downhole conditions and pressure changes in a well.
- **Transient time:** All the simulations were run in transient conditions, because the nature of the gas-liquid separation process changes over time. The separation is not an instantaneous process, performed during a retention time. It involves complex dynamic

flow patterns, where bubbles are present, and their coalescence or break up is time dependent. Some steady-state simulations were run at the early stages of this study for verification purposes, but they are not discussed in this thesis.

- **Gravity** was considered in the vertical y-axis, with a standard value of -9.81 m/s^2 .
- **Realizable k-epsilon turbulence modeling:** According to literature, three turbulence models are commonly used (k-epsilon, k-omega, and RSM). This study chooses the realizable k-epsilon because its computational expense is lower than the other two models. Also, the swirl is not expected to be too strong, as this is a static separator. For strong swirls and separators with circulation, characteristics expected in dynamic separators, the RSM is recommended. Furthermore, k-omega models are sensitive to mesh quality and require a finer mesh for accuracy. Meanwhile, k-epsilon models are known to work well with coarser meshes. The realizable k-epsilon was chosen over the standard and RNG k-epsilon models because it is the most robust version that includes extra transport equations to give more accurate, realistic, and meaningful results.
- **Eulerian multiphase modeling:** Of the three (VoF, Mixture, and Eulerian) Euler-Euler approaches, the Eulerian model is the most robust and computationally efficient. It has been successfully used to simulate multiphase flows due to its ability to track different domain phases. It is the most used model in the literature, when simulating gas-liquid centrifugal separation. Another important consideration is that the model assumes the phases are well-mixed, which is an accurate assumption for this study.
- **Fluids:** Water and air were used as the fluids. Some cases were run in single-phase with either water or air. In cases where multiphase flow was run, water was considered the primary (continuous) phase with air as the secondary (dispersed) phase.

- The boundary conditions for turbulence were set with an intensity and hydraulic diameter specification method. This method was selected due to the knowledge of the hydraulic diameters for the inlet and outlets.
- Velocity inlets were used for all the cases. Different velocities were used depending on the study case. Detailed information is provided on the velocities in the following section.
- Some study cases were run with pressure outlets, while others simulated fixed mass-flow outlets. Detailed information is provided on the outlets in the following section.
- Default solution methods were initially used to run the cases. However, some cases required modification in solution methods to achieve convergence. In single-phase cases, the SIMPLE scheme was used for the pressure-velocity coupling. For the spatial discretization, Second Order and Second Order Upwind methods were used for pressure and momentum, respectively. Meanwhile, the First Order Upwind method was used for turbulent kinetic energy and dissipation rate. For a couple of cases, the methods were changed to PRESTO! for pressure and QUICK for momentum, turbulent kinetic energy, and dissipation rate. For multiphase cases, the Phase Couple SIMPLE scheme was used with the PRESTO! method for pressure, using the First Order Upwind method for momentum, volume fraction, turbulent kinetic energy, and dissipation rate.

3.4. Results

Eight single-phase and five multiphase study cases were run using the described simulation design, each for 15 seconds of flow time. This flow time was adequate for the cases to achieve a steady-state behavior. Each case was monitored through the following considerations: scaled

residuals and chosen parameters, including fluxes and area-weighted average pressures. When the parameter fluctuations and standard deviation reduce to less than 1 Pa (1.5×10^{-4} psi) for pressures, less than 1×10^{-5} kg/s (0.02 MCFD) for gas exiting fluxes, and 0.01 kg/s (5 BPD) for liquid exiting fluxes, the case is considered to achieve a steady state. The state can be observed in Figure 3.15 when the line stops changing with time. The values presented in the following sections are averages of the parameters during the considered “steady” flow time. Generally, the steady state was achieved after around 6 seconds of flow time, meaning the results shown are calculated over the last 9 seconds of flow time. Following are the results obtained, starting with the single-phase flow simulations, followed by the results of the multiphase flow simulations.

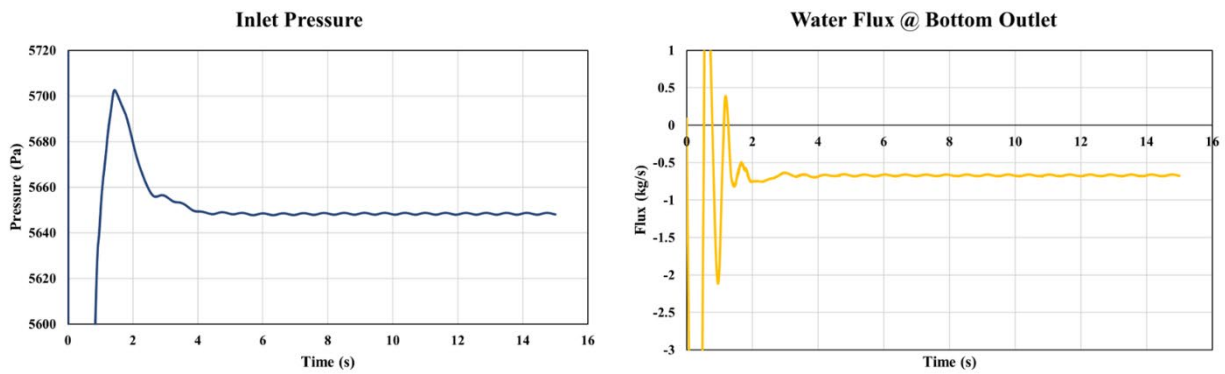


Figure 3.15. Steady state achievement during transient simulations.

3.4.1. Single-Phase Flow Simulations with Constant Outlet Pressure

Four single-phase cases were simulated with velocity inlet and pressure outlets, two with air and the other two with water. These cases are easier to converge than the multiphase flow cases. They are used to understand the dynamics of liquid and gas fluid flow inside the separator. The cases followed the modeling set-up described before, with the difference that multiphase modeling was not activated. Table 3.6 displays the boundary conditions and the results obtained for each case. The densities of air and water for the following calculations are 1.29 and 997 kg/m³,

respectively. Flow rates or fluxes with negative values mean the fluid is leaving the domain, while the positive values mean the fluid enters the domain. Furthermore, as the domain's vertical length is 21.5 in or 0.546 m, the hydrostatic columns with air and water are calculated as 6.05 Pa (0.0009 psi) and 5340 Pa (0.5 psi), respectively. However, the pressure was set as 0 Pa for both outlets for initial simulation purposes.

Table 3.6. Single-phase simulation results using pressure outlets

Cases	Case 1	Case 2	Case 3	Case 4
Boundary Conditions				
Fluid	Air	Air	Water	Water
Inlet	1 m/s	5 m/s	0.2 m/s	0.6 m/s
Bottom Outlet	0 Pa	0 Pa	0 Pa	0 Pa
Top Outlet	0 Pa	0 Pa	0 Pa	0 Pa
Results				
Inlet Pressure (gauge)	32 Pa	527 Pa	771 Pa	5670 Pa
Inlet Flux (Flow Rate)	2.98x10 ⁻³ kg/s (7.05 MCFD)	14.9 x10 ⁻³ kg/s (35.24 MCFD)	0.49 kg/s (263.07 BPD)	1.46 kg/s (789.22 BPD)
Bottom Outlet Flux (Flow Rate)	-0.39x10 ⁻³ kg/s (-0.84 MCFD)	-0.69x10 ⁻³ kg/s (-1.64 MCFD)	-5.56x10 ⁻³ kg/s (-3.01 BPD)	-56.6x10 ⁻³ kg/s (-30.64 BPD)
Top Outlet Flux (Flow Rate)	-2.59x10 ⁻³ kg/s (-6.21 MCFD)	-14.2x10 ⁻³ kg/s (-33.60MCFD)	-0.48 kg/s (-260.01 BPD)	-1.40 kg/s (-758.58 BPD)
Fluid % Bottom	12%	5%	1.2%	3.9%
Fluid % Top	88%	95%	98.8%	96.1%

The inlet velocities for the cases shown in Table 3.6 were chosen considering the computational expense of the simulation, while attempting to simulate opposite cases with low and high flow rates. Cases 1 and 2 are single-phase cases using gas. The fluid percentages leaving through the top outlet are 88% and 95% in cases 1 and 2, respectively. The behavior is similar in cases 3 and 4, where single-phase water flow is simulated. Most of the liquid flows out of the

domain through the top outlet in these cases, with the fluid percentages of 98.8% and 96.1% through the top outlet in cases 3 and 4, respectively.

The Bottom and Top outlets have the same shape (annular) and are set at the same pressure (0 Pa). The only difference is the size, as seen in Table 3.1. The top outlet is bigger (27.47 in²) than the bottom outlet (14.42 in²), reducing the frictional losses when the fluids, air or water, flow out of the top outlet. When fluids encounter multiple outlets, they get distributed based on the available pathways and the resistance each pathway offers. As the top outlet is bigger, it offers less resistance than the bottom outlet. This justifies the simulation results. So, it can be said that the fluid behavior follows a natural trend of the fluids flowing through the bigger outlet (top outlet).

Figure 3.16 displays the pathline of one particle exiting the top outlet in case 2, colored according to its velocity. The separator inlet (blue), outlets (red), and edges (gray) are displayed. The helices section is hidden to better display the spiral motion of the particle inside one of the helix-type paths. The picture shows that the fluid is forced through a helix-type path that generates centrifugal force. Hence, the fluid experiences an apparent increase in gravity as it moves radially outward from the center. The spiral motion continues after the fluid is expelled out of the helix above the separator.

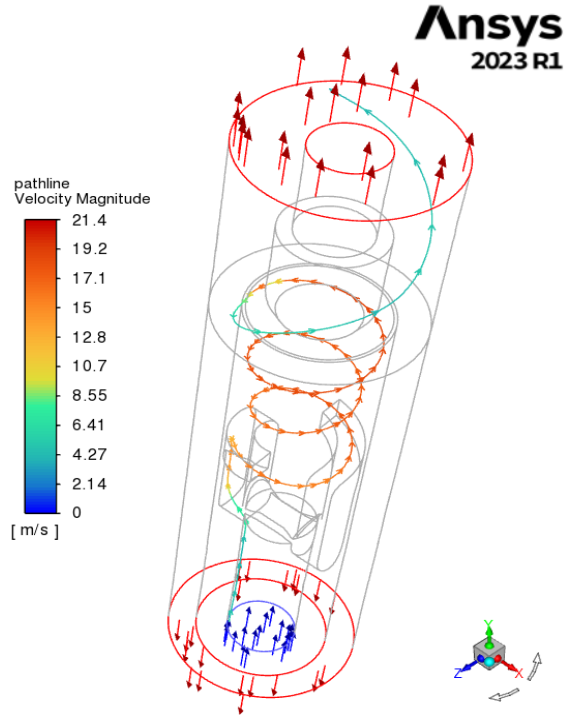


Figure 3.16. air particle pathline in Case 2.

Figure 3.17 displays an X-Y plane cut in the middle of the separator for each of the four cases, giving more insight into the velocity behavior. The figure shows that the fluid particles near the outer wall of the container have higher velocities than those closer to the center. The centrifugal force generated due to the shape of the helix-type path acts on the fluid particles by moving them away from the axis of rotation, incrementing the concentration of particles in the outermost section of the paths. In addition, the change in cross-sectional area from the inlet (3.8013 in^2) to the helix-type path (0.6 in^2) increases the velocity magnitude inside the paths.

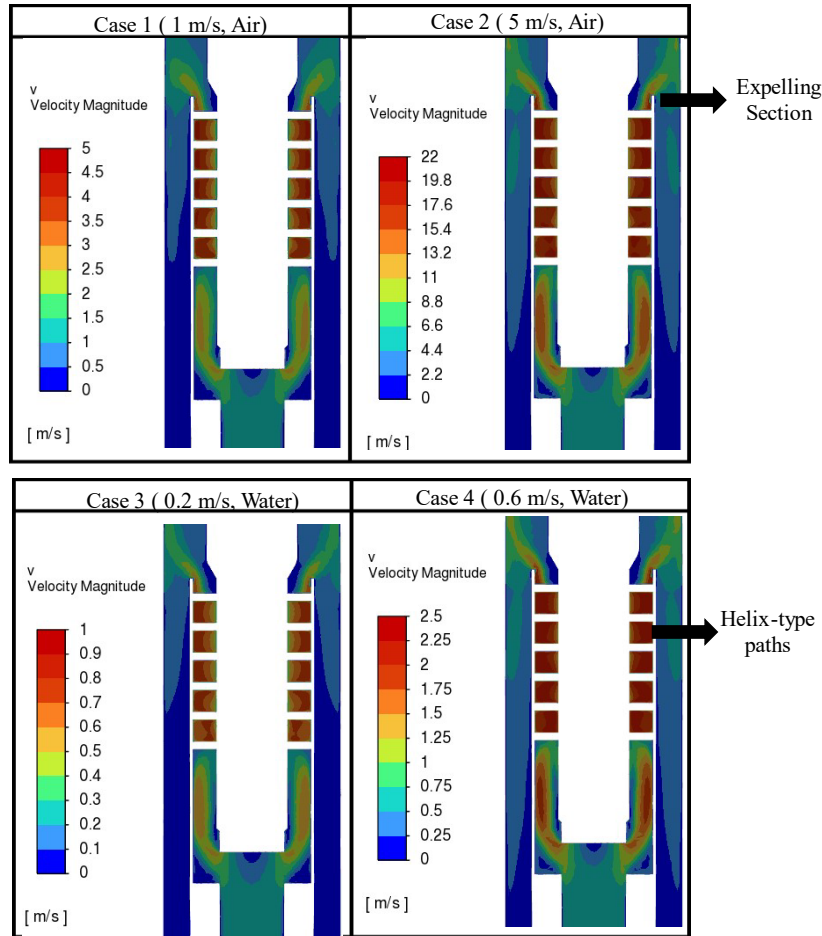


Figure 3.17. Cases 1 to 4 velocity contours

From the figure above, the velocity varies depending on the inlet velocity used for each case. However, the velocity magnitude increases in the same proportion in the outermost section of the helix-type paths, which are seen as square shapes in the X-Y plane cuts. The velocity in these sections is about five times larger than the inlet velocity. For example, the inlet velocity is 0.2 m/s for case 3, while the generated velocity in the outermost section of the helix-type paths is 1 m/s. After the fluids are expelled out of the helices, the particle's velocity decreases. This phenomenon is due to the reduction of helical motion and increased axial movement up and down the separator. The expelling section velocities seem chaotic and large regardless.

It is expected that the fluid's velocity increases in when it is forced through the helix-type paths. However, the corner sections in the inner part of the separator seem to have lower velocities, which is observed throughout all the cases. Figure 3.18 displays the corner section with lower velocity inside the separator, using case 3 as an example.

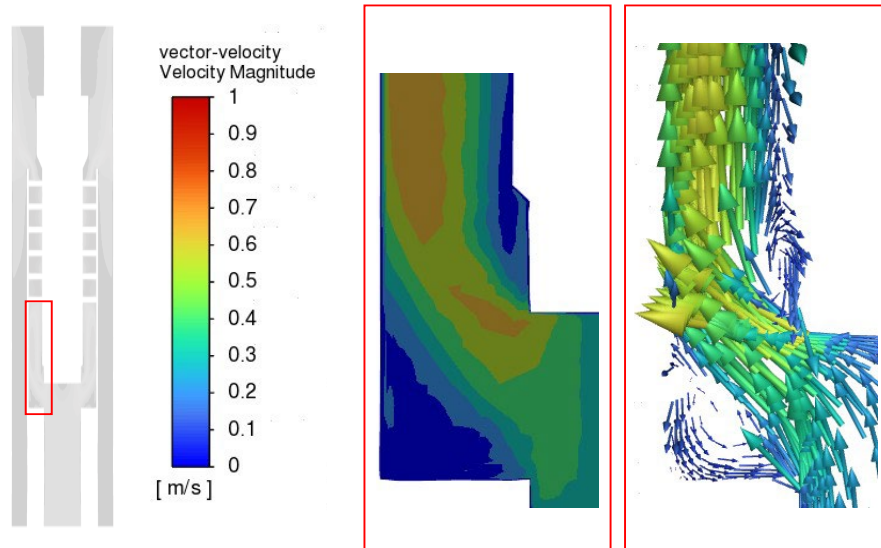


Figure 3.18. Vortex cores or eddies formation.

The above figure displays two sections of the inner separator where precessing vortex cores are formed. This phenomenon occurs due to the geometry of the separator, as the fluids encounter an obstruction impinging the wall and generating a recirculation path in those areas. The vortex generates turbulence in the area, affecting the velocity profile, which can harm the separator's performance. It is recommended to re-design this section by providing a smooth transition that reduces the generation of these vortex cores.

Figure 3.19 displays the contours of the dynamic pressure for the simulated cases. As expected, the dynamic pressure increases with the velocity increase. The largest pressure occurs in the outermost section of the helix-type paths, like the velocity magnitude increase. This dynamic

pressure can also be called head or pressure generated due to the helical motion of fluids, as it is the kinematic energy in the fluid due to its motion.

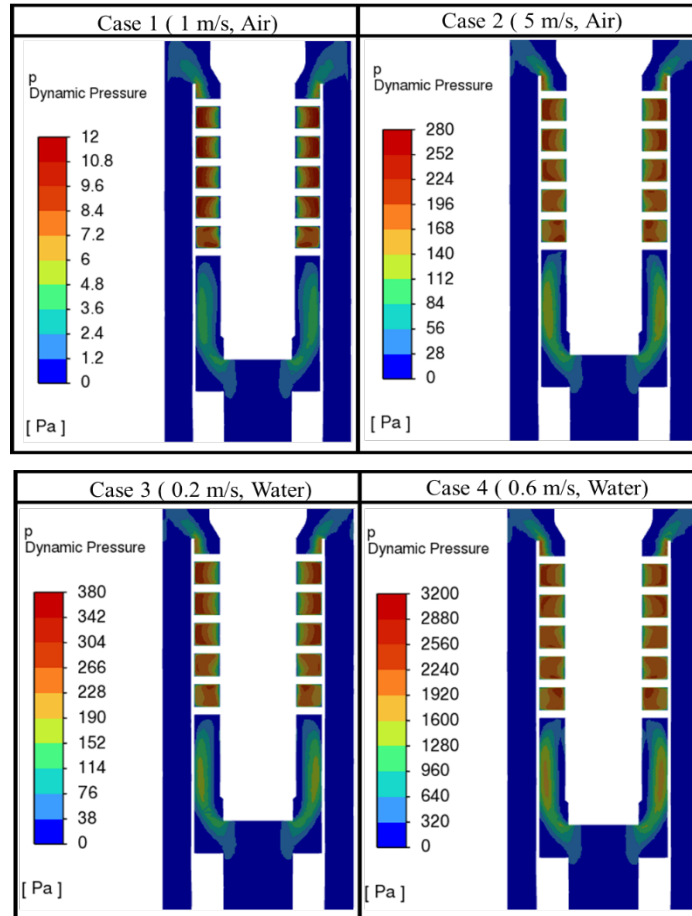


Figure 3.19. Cases 1 to 4 dynamic pressure contours.

During the simulations, a reversed flow was observed. Reversed flow is understood as the flow re-entering the domain through the outlet. Vertical velocity profiles were plotted in two lines intersecting the X-Y center plane cut and close to the outlets to observe this phenomenon. Figure 3.20 shows the vertical velocity profiles for cases 1 to 4 close to the bottom outlet. The line's location (red) is where the velocity profiles are plotted. As the vertical coordinate of the model for this study is the Y-axis, the exit or entrance of fluids can be seen by plotting this variable along

the line. The negative values show the fluid exiting the domain, while the positive values show the reversed flow of fluid into the domain.

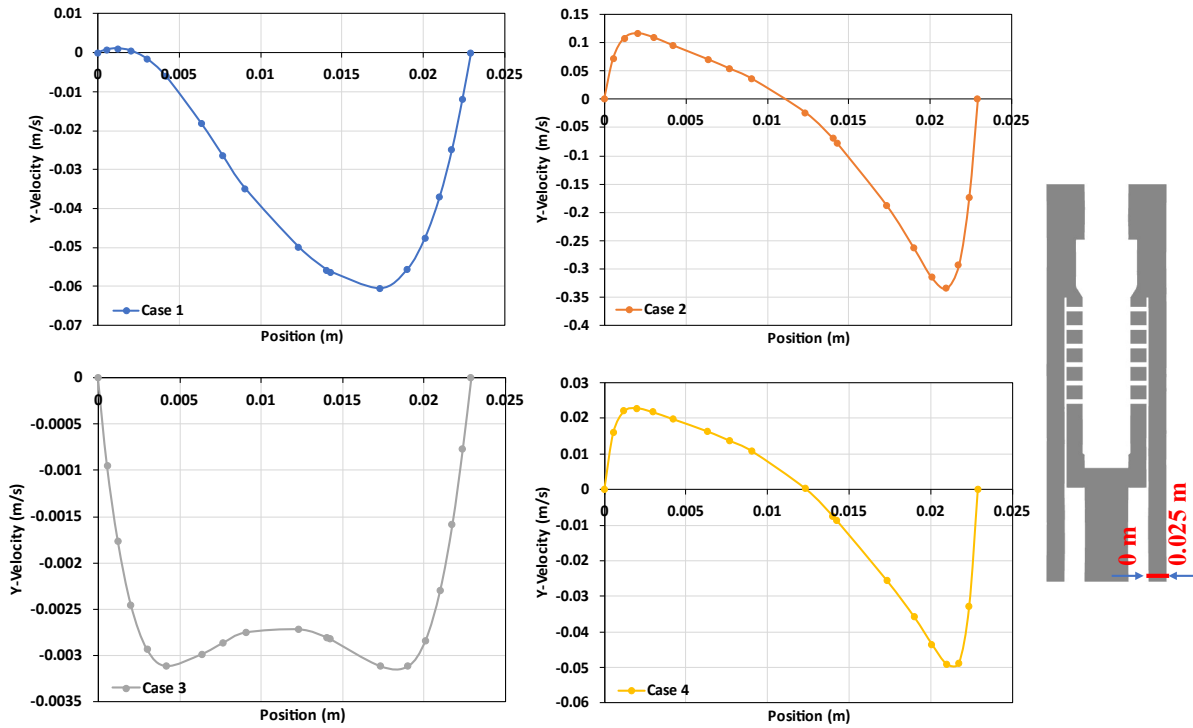


Figure 3.20. cases 1 to 4 velocity profiles in the bottom outlet.

The above plots show the velocity profiles on a line close to the bottom outlet. These profiles are plotted on one side of the bottom outlet, but because the outlet is annular, the same behavior is expected on the opposite side. The expected values of the vertical velocity are negative, meaning that the fluids are flowing downward. Cases 1 and 3 simulate low fluid velocities, air at 1 m/s and water at 0.2 m/s, respectively. Both cases have negative vertical velocities along the line, meaning the fluids are expelled throughout the outlet area. Case 1 has an almost fully developed profile with a little reversed flow in the inner part of the outlet. Meanwhile, case 3 has a developing profile. As the inlet velocities of the fluids in these cases are not high, they seem to be leaving the domain properly without any major disturbance, turbulence, or eddies formation.

Cases 2 and 4 simulate higher fluid velocities than the prior cases, air at 5 m/s and water at 0.6 m/s, respectively. As shown in their plots, both cases present reversed flow in the inner part of the bottom outlet. This might be caused by the continuous rotational motion of the fluids, when expelled from the spiral section. Although they decrease along the outlet, the rotational motions still influence the flow dynamics. Due to the movement of the fluids to the outer walls of the annulus, the pressure tends to be lower at the innermost section of this swirling movement,. This phenomenon might cause the fluids to reenter the domain at the inner section of the annulus. It is assumed that if the length of the section guiding to the bottom outlet is enlarged, like the real pipe systems in the wells, this phenomenon diminishes with length.

Figure 3.21 shows the velocity profiles of cases 1 to 4 close to the top outlet. Unlike the bottom outlet, all the cases show reversed flow to a certain degree in the top outlet. As the outlet being analyzed is at the top, positive vertical velocities represent fluids flowing upward and leaving the domain. The reverse flow is present in the inner section of the top outlet. An important feature of the model is the proximity of the helical path output to the top outlet. There is not enough length for the flow to develop, which may cause turbulence, large spirals, and unexpected dynamics that result in reversed flow.

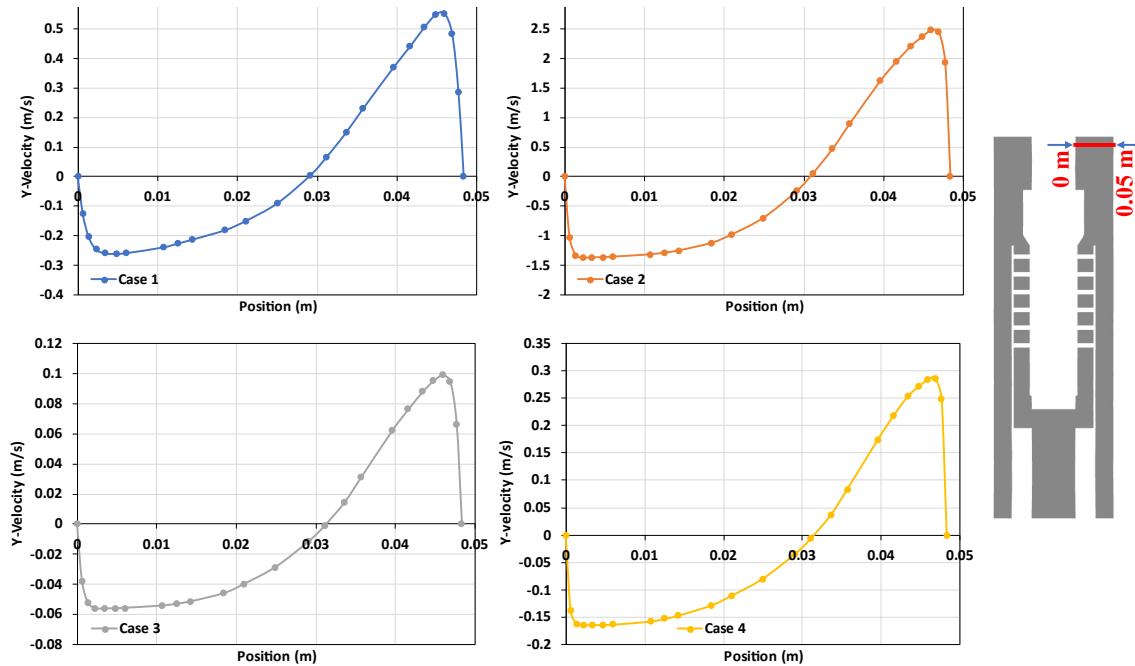


Figure 3.21. cases 1 to 4 velocity profiles in the top outlet

The turbulence influencing the reversed flow can be explained by the formation of eddies, as seen in Figure 3.22. This figure displays the velocity vectors in the top outlet section for case 3. The expelling section has larger velocities due to the induced centrifugal force. When the air, in this case, impinges on the wall, the velocity decreases. A part of the fluid flows upward without disruption, but a part of it enters a large eddy stream closer to the center of the separator. This generates turbulences and reversed flow due to the creation of low-pressure zones.

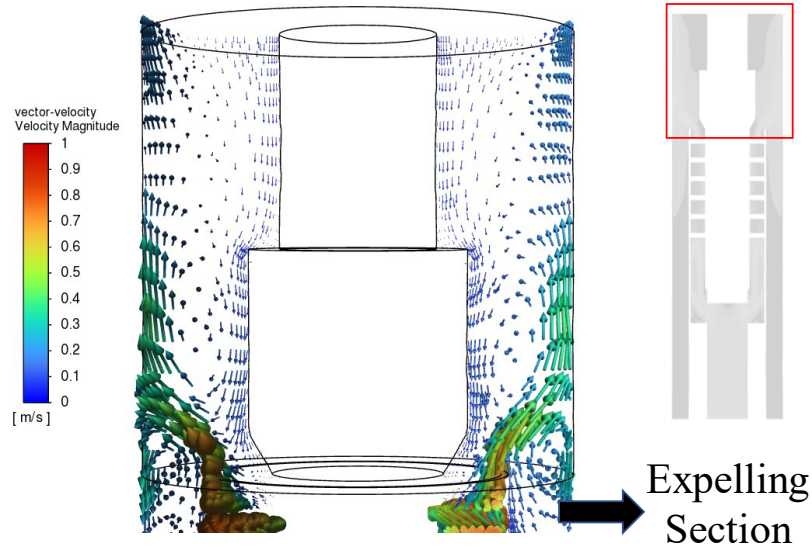


Figure 3.22. Eddies formation in the top section of the separator.

The expelling section of the separator constitutes a critical area for the equipment performance, especially when simulating multiphase flow. The fluid behavior is chaotic after getting expelled out of the helices and impinging onto the inner casing wall. This impingement releases a large amount of energy, in the form of high instantaneous static pressures, as seen in Figure 3.23. Right after the impingement, the fluids flow towards the outlets. The movement in this area is chaotic with vortices and eddies seen in Figure 3.22, close to the innermost section of the separator, resulting in significant pressure losses. Modifying the sharp features of this section might help reduce the chaotic behavior and help the fluid's transition from a high swirling movement (in the helices) to a low swirling movement (in the outlet).

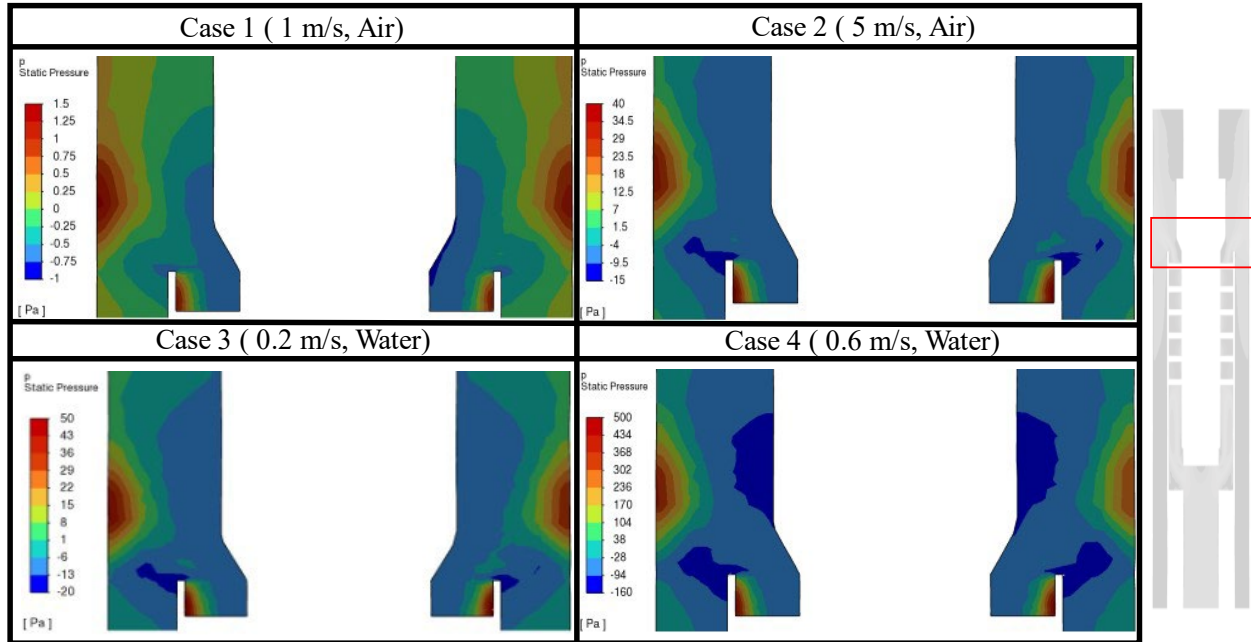


Figure 3.23 Instantaneous static pressure contours for cases 1 to 4 in the expelling section.

3.4.2. Single-Phase Flow Simulations with Constant Outlet Mass

After observing the reversed flow in constant outlet pressure simulations, it was decided to run the same cases with imposed outlet mass-flow-rate boundary conditions. Cases 5-8 were simulated with the aim of repeating cases 1-4, but with fixed mass rates at the two outlets. Table 3.7 displays the new boundary conditions set and the obtained results. The objective was to analyze the flow through the separator with the specific fluids going through the desired outlets, gas through the top outlet and liquid through the bottom outlet, expected in multiphase flow scenarios. All the cases converged properly with the imposed conditions.

Table 3.7. Single-phase cases using mass-flow outlets

Cases	Case 5	Case 6	Case 7	Case 8
Boundary Conditions				
Material	Air	Air	Water	Water
Inlet	1 m/s	5 m/s	0.2 m/s	0.6 m/s
Bottom Outlet (% of inlet mass flux)	5 %	10%	95%	90%
Top Outlet (% of inlet mass flux)	95 %	90%	5%	10%
Results				
Inlet Flux (Flow Rate)	2.98x10 ⁻³ kg/s (7.05 MCFD)	14.9 x10 ⁻³ kg/s (35.24 MCFD)	0.49 kg/s (263.07 BPD)	1.46 kg/s (789.22 BPD)
Bottom Pressure Drop ($P_{bottom} - P_{inlet}$)	-30.83 Pa	-501.48 Pa	-450.10 Pa	-5104.50 Pa
Top Pressure Drop ($P_{top} - P_{inlet}$)	-30.76 Pa	-505.47 Pa	-448.77 Pa	-5108.59 Pa
Outlets Pressure diff. ($P_{bottom} - P_{top}$)	0.15 Pa	3.99 Pa	-1.33 Pa	4.09 Pa

Table 3.7 shows pressure drops for cases 5 to 8. The top and bottom outlets were assumed at the same pressure for cases 1 to 4. Even though the difference is not too large for the top and bottom outlets in cases 5 to 8, the bottom outlets seem to be slightly larger for three cases (5, 6, and 8). It is physically correct that the bottom outlet has a larger pressure as it is loaded with a column of fluid. However, the mentioned pressure difference does not seem to be significant, justifying the initial assumption (taken for cases 1 to 4) of using the same pressure for both outlets.

It was identified that the velocities and dynamic pressures for cases 5 to 8 vary from the values obtained in cases 1 to 4. Figure 3.24 displays dynamic pressure contours of cases 5 to 8 with the same scale used priorly in Figure 3.19. The dynamic pressures, hence, the velocities, are lower for cases 5 to 8. Furthermore, the velocities projected in the expelling section are lower than cases 1 to 4. This observation might give an insight into how to obtain a good separation when two fluids are injected in the separator. If, after the fluids acquire the peak velocity and dynamic

pressure at the top of the helix-type path, the velocity is immediately decreased in the expelling back section, the chances of vortexes or eddies generation might be lower. This will be analyzed further in the multiphase flow section.

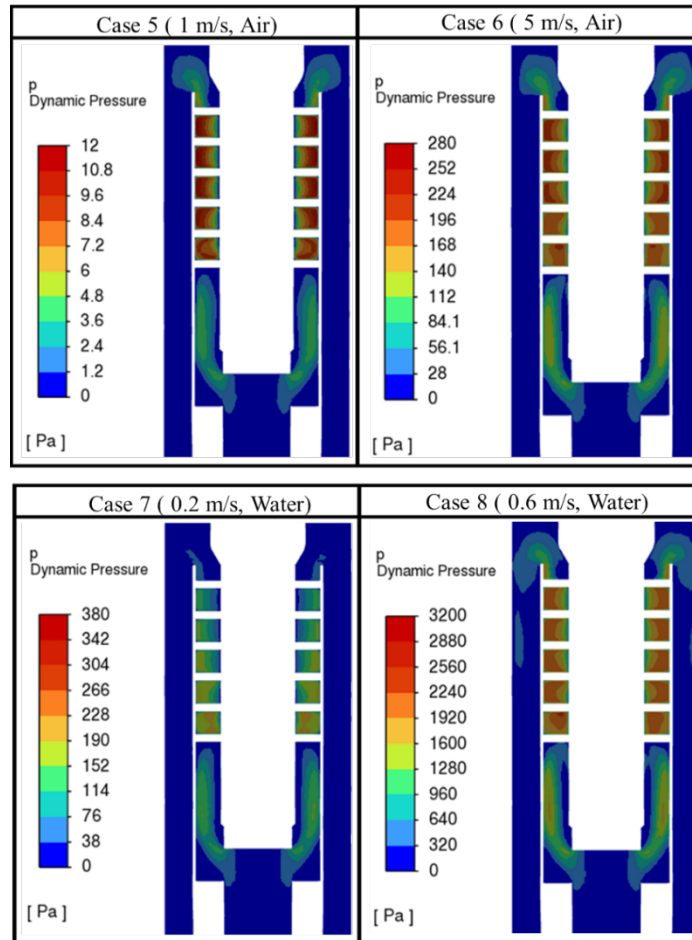


Figure 3.24. Cases 5 to 8 dynamic pressure contours.

The velocity profiles were analyzed for these four cases on the same lines used previously. Figure 3.25 shows the velocity profiles for cases 5 to 8 on the line close to the bottom outlet. Three cases (5, 7, and 8) do not have reversed flow at the bottom outlet. However, case 6 shows a slight reverse flow in the inner part of the annular outlet. Like the previous cases, displayed in Figure 3.20, the reversed flow occurs in the outlet's innermost section in case 6. There is still a rotational

movement in the innermost section of the annulus, which might cause the formation of small eddies with lower pressure zones and promote reversed flow.

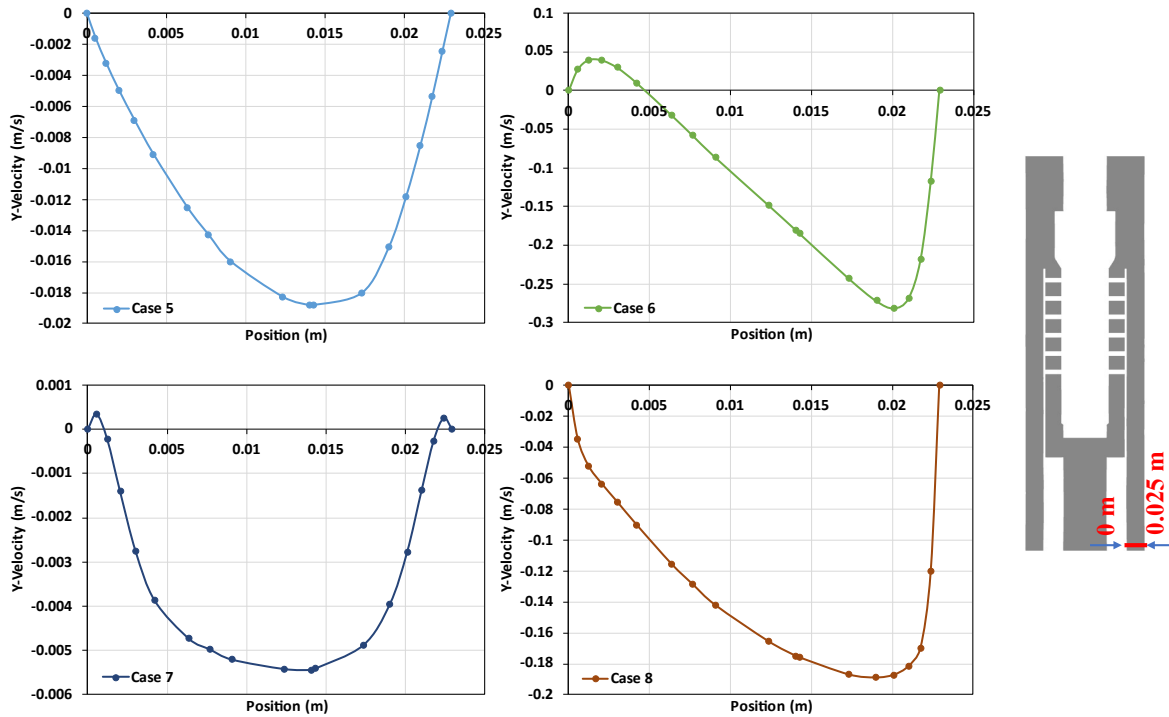


Figure 3.25. Velocity profiles of cases 5 to 8 close to the bottom outlet

Figure 3.26 displays the velocity profile for cases 5 to 8 on the line close to the top outlet. Cases 5 and 6 correspond to the cases where air was used. In both cases, there is no reversed flow, and the Y-velocity is larger at the outermost side of the top outlet. Cases 7 and 8 were simulated with water, showing reversed flow and negative Y-velocity for a section of the top outlet. This is expected as the water was imposed to leave through the bottom outlet, so there is a tendency for it to flow downward. For all cases, a larger velocity is observed at the outermost side of the top outlet. This is due to the centrifugal forces caused by the rotational motion of the fluid when getting expelled out of the helix-type paths, pushing the fluids outwards. The generated eddies and the resulting vacuum at the inner section of the annulus, cause this reversed flow.

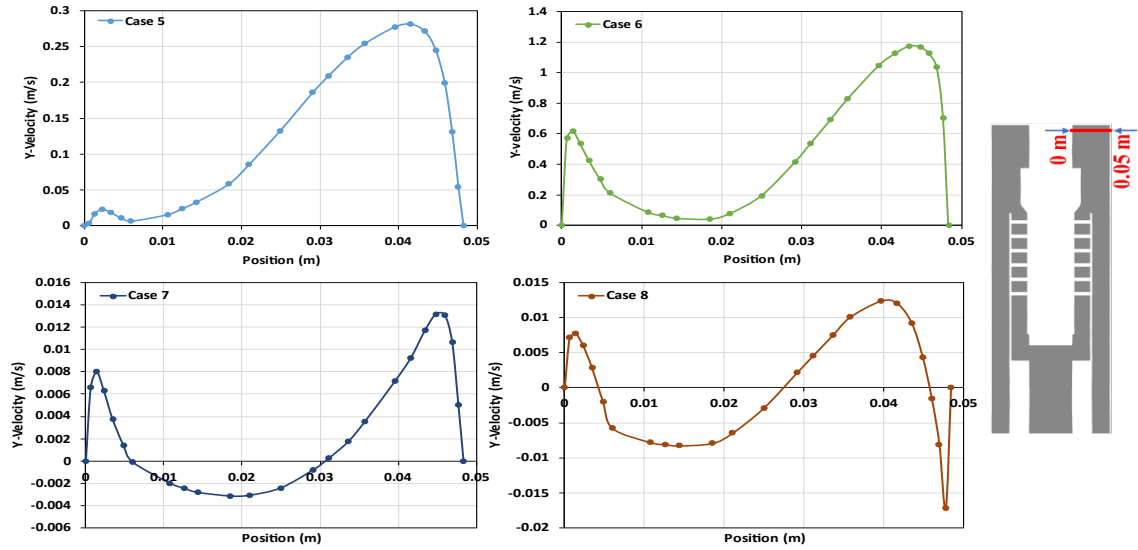


Figure 3.26. Velocity profiles of cases 5 to 8 close to the top outlet

Figure 3.27 shows the air and water particle pathline where mass-flow rates were imposed in cases 5 and 7. The velocity magnitudes are maximized inside the helical path for both cases. Also, the rotational motions are maintained after the particles are expelled out of the helical paths.

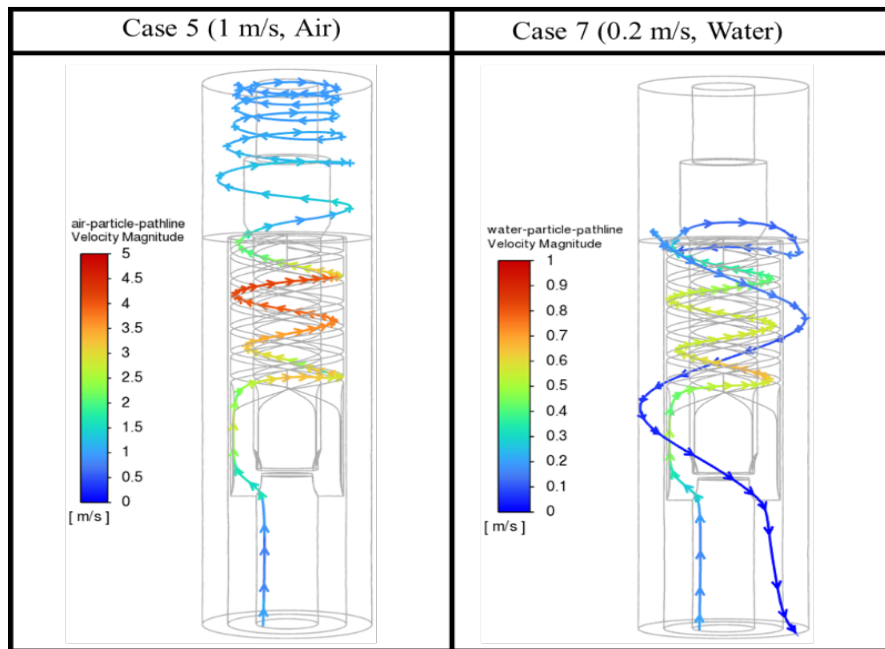


Figure 3.27. air and water particle pathlines inside and outside the helical paths

3.4.3. Multiphase Flow Study Cases

A multiphase case (Case 9) was set up to better understand the fluid dynamics inside the separator. In this case, the domain was filled with air, while water was injected through the inlet. Table 3.8 displays the results obtained in this initial multiphase flow case vs. those obtained in the most similar single-phase case (case 3). Case 9 was run using the VoF multiphase flow model instead of the Eulerian model used in the following cases. VoF was selected because it was computationally friendly to track the interface or the waterfront.

Table 3.8. Single-phase Case 3 (water) vs. Multiphase Case 9 (water-air)

Cases	Case 3	Case 9
Boundary Conditions		
Simulation Type	Single Phase	Multiphase
Fluids	Water	Air (primary) - Water (secondary)
Inlet	Water at 0.2 m/s	Water at 0.2 m/s
Initialization	Domain full of water	Domain full of air
Bottom Outlet	0 Pa	0 Pa
Top Outlet	0 Pa	0 Pa
Results		
Inlet Pressure (gauge)	771 Pa	4601 Pa
Inlet Flux (Flow Rate)	0.49 kg/s (263.07 BPD)	0.49 kg/s (263.07 BPD)
Bottom Water Outlet Flux (Flow Rate)	-5.56x10 ⁻³ kg/s (-3.01 BPD)	-0.49 kg/s (-263.07 BPD)
Bottom Air Outlet Flux (Flow Rate)	-	-5.37x10 ⁻³ kg/s (-12.70 MCFD)
Top Water Outlet Flux (Flow Rate)	-0.48 kg/s (-260.01 BPD)	0 kg/s (0 BPD)
Top Air Outlet Flux (Flow Rate)	-	5.37x10 ⁻³ kg/s (12.70 MCFD)
Liquid % Bottom	1.14%	100 %
Liquid % Top	98.8 %	0 %

The liquid follows the desired trend in case 9 by leaving through the bottom outlet. As expected, the interaction between the two fluids seems to push the liquid downward because of its higher density. Furthermore, there is a 100% reversed flow of air at the top outlet. The air entering from the top leaves the domain in totality through the bottom outlet.

Figure 3.26 displays the volume fraction, velocity, and dynamic pressure contours for case 9. The liquid follows the desired trend in case 9 by leaving through the bottom outlet. As expected, the interaction between the two fluids seems to push the liquid downward because of its higher density. Furthermore, there is a 100% reversed flow of air at the top outlet. The air entering from the top leaves the domain in totality through the bottom outlet. It is believed that the reason for the reverse flow in the top outlet is the system trying to keep the balance of imposed pressure outlets. This observation indicates that the pressure difference between the outlets plays an important role in the convergence of the simulation.

Figure 3.28 has the same colormap as the ones in Figures 3.17 and 3.19, where case 3 contours are shown. It can be noticed that the velocity magnitude, and hence the dynamic pressure, inside the helix-type path is lower here. Also, unlike case 3, case 9 presents high velocity and pressure generation outside the helix-type paths at the inner part of the bottom outlet route. The water volume fraction contour displays how the water pours down, seeking to escape through the bottom outlet. The water seems to stay closer to the inner wall, possibly due to the high gas amount coming from the top and leaving through the bottom outlet, pushing the liquid to the inner wall.

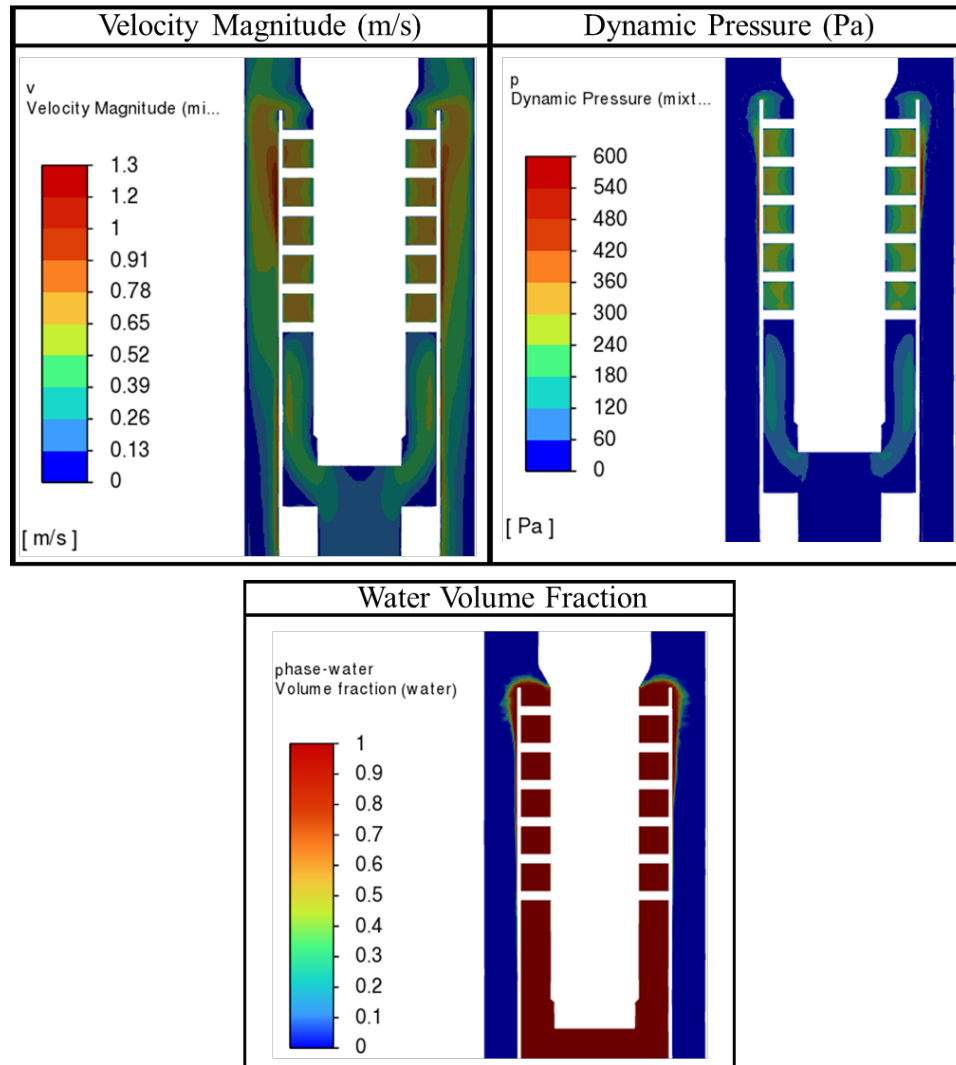


Figure 3.28. Case 9 contours of velocity, dynamic pressure, and water volume fraction

As both air and water leave through the bottom outlet, the Y-velocity profile was plotted along a line close to the bottom outlet, like the one used in the single-phase cases. This plot shows the velocity of the two fluids at the same time. The profile is shown in Figure 3.29, where there is a small reverse flow in the outer part of the outlet. This behavior differs from the one in the single-phase cases, where the reversed flow was present in the innermost part of the outlets. This behavior can be explained by the high velocity section generated in the innermost section of the pipe, above the bottom outlet, due to the flow entering through the top outlet.

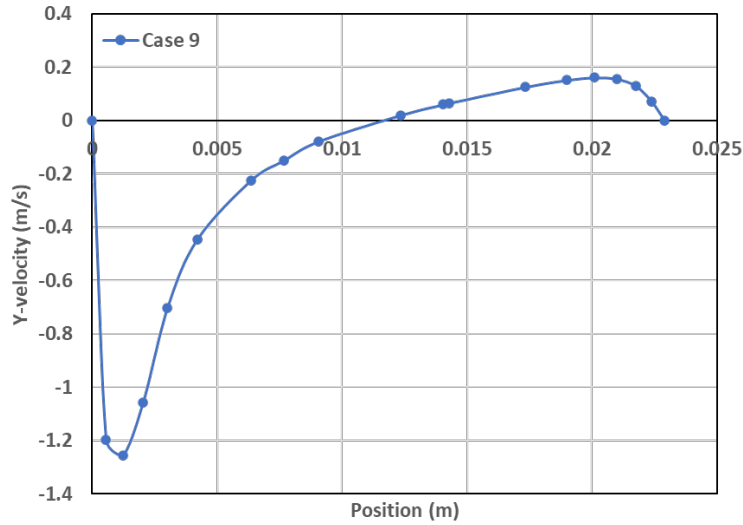


Figure 3.29. Y-velocity profile for Case 9 in the bottom outlet.

Four multiphase cases with water and air inputs (Cases 10, 11, 12, and 13) were run to understand the dynamics of multiphase flow through the separator. A gas volumetric fraction (GVF) of 0.45 was used for all cases. The Eulerian model was used to simulate the multiphase flow. The four cases differ in the boundary conditions used for the top and bottom outlets. Case 10 uses fixed-mass outlet boundaries, while Cases 11-13 use constant-pressure outlets with varying bottom outlet pressures. Table 3.9 displays the boundary conditions and results of these cases.

Table 3.9 shows that most water is leaving the domain through the bottom outlet in all the cases. This observation confirms that the air-water interaction allows the water to leave through the bottom outlet independently of the size of the outlet. This is contrary to cases 3 and 4, where single-phase water was run through the system. In case 10, fixed mass outflow boundary conditions were imposed. As most of the total mass rate is expected at the bottom outlet, this outlet was set to receive 95% of the inlet mass. The case converged correctly, and the desired outflows were achieved.

Table 3.9. Multiphase flow cases (10, 11, 12, and 13) boundary conditions and results

Cases	Case 10	Case 11	Case 12	Case 13
Boundary Conditions				
Material	Water (primary phase) - Air (secondary phase)			
Particle Size	0.001 m			
Inlet	Water = 0.5 m/s - Air = 0.4 m/s - GVF= 0.45			
Bottom Outlet	Outflow = 95% of total mass-rate	600 Pa (Backflow air = 0)	1000 Pa (Backflow air = 0)	1500 Pa (Backflow air = 0)
Top Outlet	Outflow = 5% of total mass-rate	0 Pa (Backflow air = 1)	0 Pa (Backflow air = 1)	0 Pa (Backflow air = 1)
Results				
Inlet P. (gauge)	468 Pa	5648 Pa	5723 Pa	5819 Pa
Inlet Water Flux	0.668 kg/s (362 BPD)			
Inlet Air Flux	0.536x10 ⁻³ kg/s (1.27 MCFD)			
Bottom Water Outlet Flux (Flow Rate)	-0.668 kg/s (-362 BPD)	-0.668 kg/s (-362 BPD)	-0.667 kg/s (-361 BPD)	-0.658 kg/s (-356 BPD)
Bottom Air Outlet Flux (Flow Rate)	-0.445x10 ⁻³ kg/s (-1.05 MCFD)	-0.001 kg/s (-2.76 MCFD)	-0.443x10 ⁻³ kg/s (-1.05 MCFD)	-8.198x10 ⁻⁵ kg/s (-0.19 MCFD)
Top Water Outlet Flux (Flow Rate)	-0.108x10 ⁻³ kg/s (~ 0 BPD)	0 kg/s (~ 0 BPD)	-0.0143 x10 ⁻³ kg/s (~ -1 BPD)	-8.5x10 ⁻³ kg/s (~ -6 BPD)
Top Air Outlet Flux (Flow Rate)	-6.903 x10 ⁻⁵ kg/s (-0.16 MCFD)	63.2x10 ⁻⁵ kg/s (1.49 MCFD)	-9.350 x10 ⁻⁵ kg/s (-0.22 MCFD)	-45.6x10 ⁻⁵ kg/s (-1.08 MCFD)
Bottom P. Drop ($P_{bottom} - P_{inlet}$)	-3896 Pa	-5048 Pa	-4723 Pa	-4319 Pa
Top P. Drop ($P_{top} - P_{inlet}$)	-4495 Pa	-5648 Pa	-5723 Pa	-5819 Pa
Outlets Pressure diff. ($P_{bottom} - P_{top}$)	599 Pa	600 Pa	1000 Pa	1500 Pa

In cases 11, 12, and 13, with pressure outlets, air flow through the top outlet depends on the set pressure difference between the two outlets. This phenomenon is the result of the system trying to balance the gravitational and friction losses to satisfy the imposed pressure boundary conditions. As noticed, when the pressure of the bottom outlet is 600 Pa (case 11), there is reverse air flow, coming into the domain through the top outlet (1.49 MCFD). In case 12, where the bottom

pressure is set as 1000 Pa, there is no reverse flow and gas is leaving the domain through both outlets. The bottom outlet pressure must be higher than the top outlet because of the hydrostatic fluid column. This is why the convergence occurs more easily with most of the gas leaving through the top outlet for case 13. In case 12, 1.05 MCFD (83% of total gas) leaves through the bottom outlet. Meanwhile, 100% of the water leaves through the bottom outlet. In case 13, with a bottom pressure of 1500 Pa, only 0.19 MCFD (15% of the total gas) leaves through the bottom outlet. Meanwhile, 356.4 BPD (98.5% of the total water) leaves through bottom outlet.

The velocity profiles are plotted for the same bottom and top lines used before. Figure 3.30 displays the velocity profiles for case 10. The behavior at the bottom outlet plot is like the single-phase cases 1 to 8, with slight reversed flow closer to the innermost section of the outlet. All the water is coming out of the outermost section of the bottom outlet. However, the air flow seems to have reverse flow in the innermost section of the outlet. The air's reverse flow seems logical as the natural tendency of the gas is to flow upward, leaving through the top outlet. On the other hand, the behavior of the gas in the top outlet also seems to follow the expected nature, as the air is leaving the domain through this outlet along the whole area without any reversed flow.

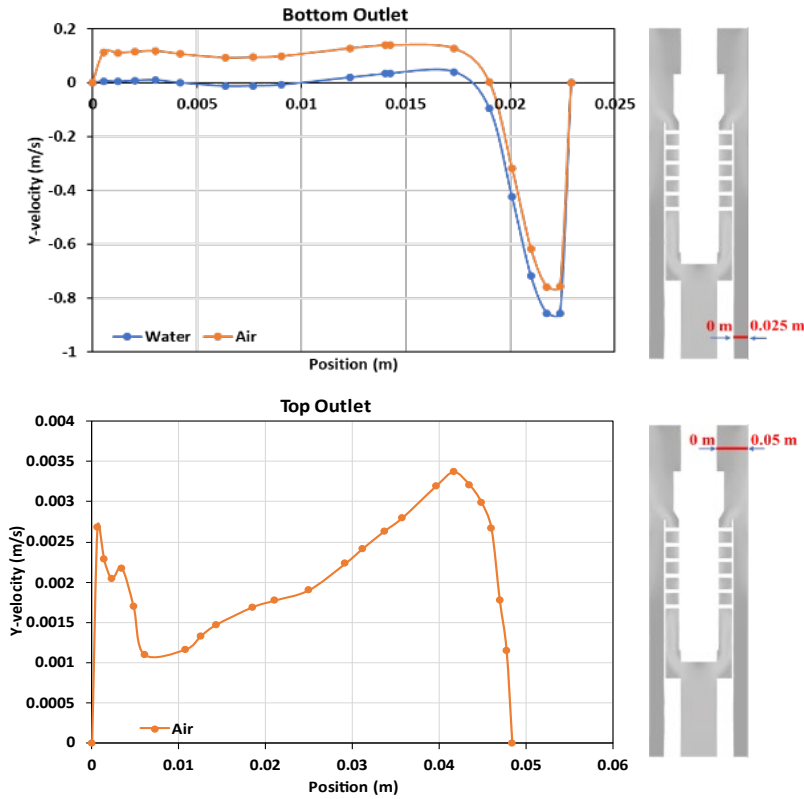


Figure 3.30. Velocity profiles for Case 10.

The vertical velocity profiles for cases 11, 12, and 13 are displayed in Figure 3.31. The water velocity plot through the bottom outlet displays how most of the water is leaving the domain closer to the outer wall of the annulus, with no reverse flow. There is no significant water reverse flow in any of the outlets. Cases 12 and 13 show 0.3% and 1.7% of the water leaving through the top outlet, respectively. From the plot representing the water leaving through the bottom outlet, most of the reverse flow occurs in the outermost section of the outlet. It is 100%, 99.7% and 98.3% for cases 11, 12, and 13, respectively.

The air leaving through the bottom for cases 12 and 13 are 83% and 15%, respectively. There is some reverse flow closer to the inner wall of the bottom outlet for the air, which is similar to what was observed in the single-phase cases. In cases 12 and 13, 17% and 85% of air leaving

through the top outlet, respectively. This shows the effect of pressure on air-water separation efficiency. In Case 13, with a proper pressure differential between the two outlet, air and water are exhibiting a near-ideal separation. This makes Case 13 the best scenario to continue an efficiency study with different GVF's. This observation helps reinforce the importance of separator pressure control. To achieve a good performance of the downhole separator, a pressure control system needs to be implemented as mentioned in Chapter 2 for laboratory testing.

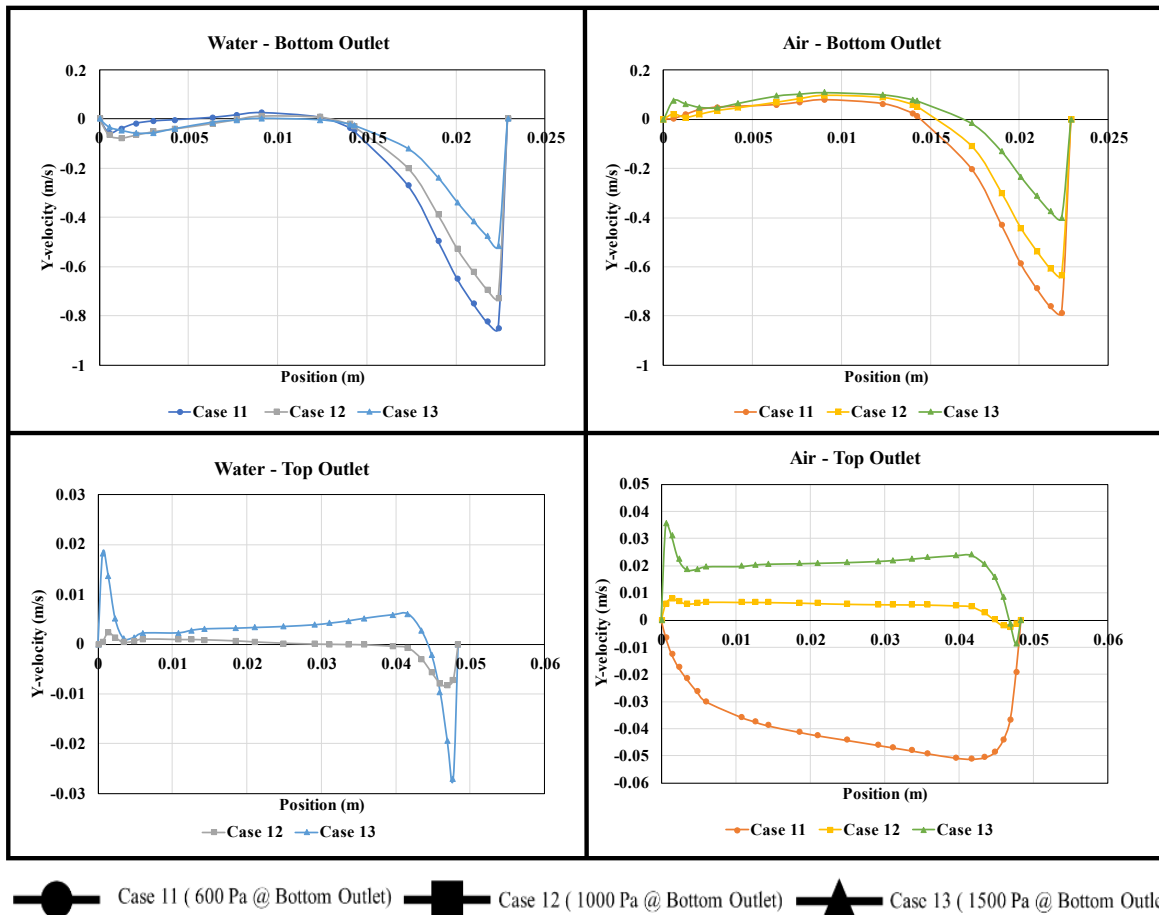


Figure 3.31. Cases 11, 12, and 13 Y-velocity profiles close to the bottom and top outlet.

Figure 3.32 displays the water volume fractions for the three cases. These contours show how water and gas are separated in the helix-type paths. The water volumetric fraction increases closer to the outer walls of the helical paths, due to the centrifugal forces. As the fluids flow from

the bottom to the top of the helical path, the amount of separated water increases, reaching its maximum in the top section of the path, right before the expelling section. For all three cases, the water is shown to get forced on the outer walls of the annular section after exiting the helical paths. This is due to the imposed centrifugal forces that consequently improve the separation. Case 13 seems to show the best performance with the highest volumetric water fractions close to the bottom outlet, showing the effect of pressure differential on separation efficiency.

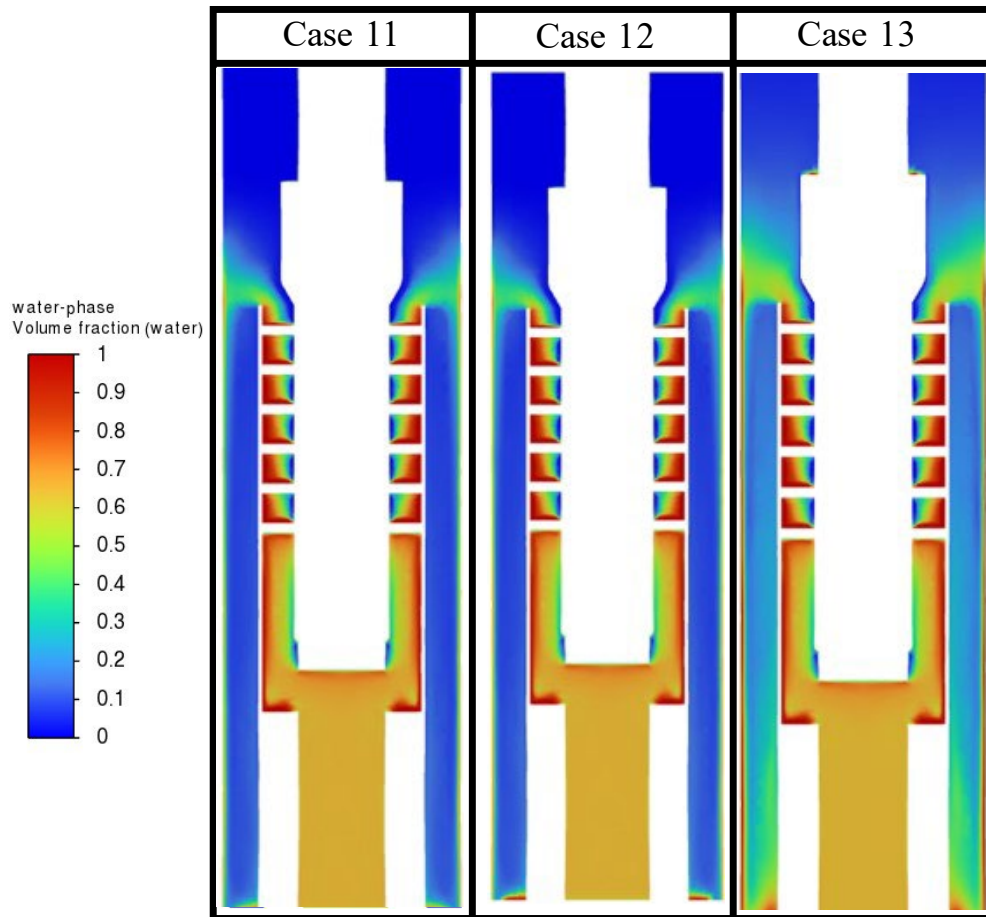


Figure 3.32. water volume fraction contours for cases 11, 12, ad 13.

Figure 3.33 displays the dynamic pressure contours in the helix-type path, using case 13 as an example. As seen in the figure, higher dynamic pressures, and hence velocities, occur in the innermost section of the helices. This can be explained by the conservation of angular momentum,

as the particles rotating closer to the center with smaller radii of rotation, have higher linear momentums (mass times velocity). The conservation law states that the product of the linear momentum and radius must remain constant. Considering the correlation of dynamic pressure and velocity, the dynamic pressure is expected to be higher in the innermost section as well.

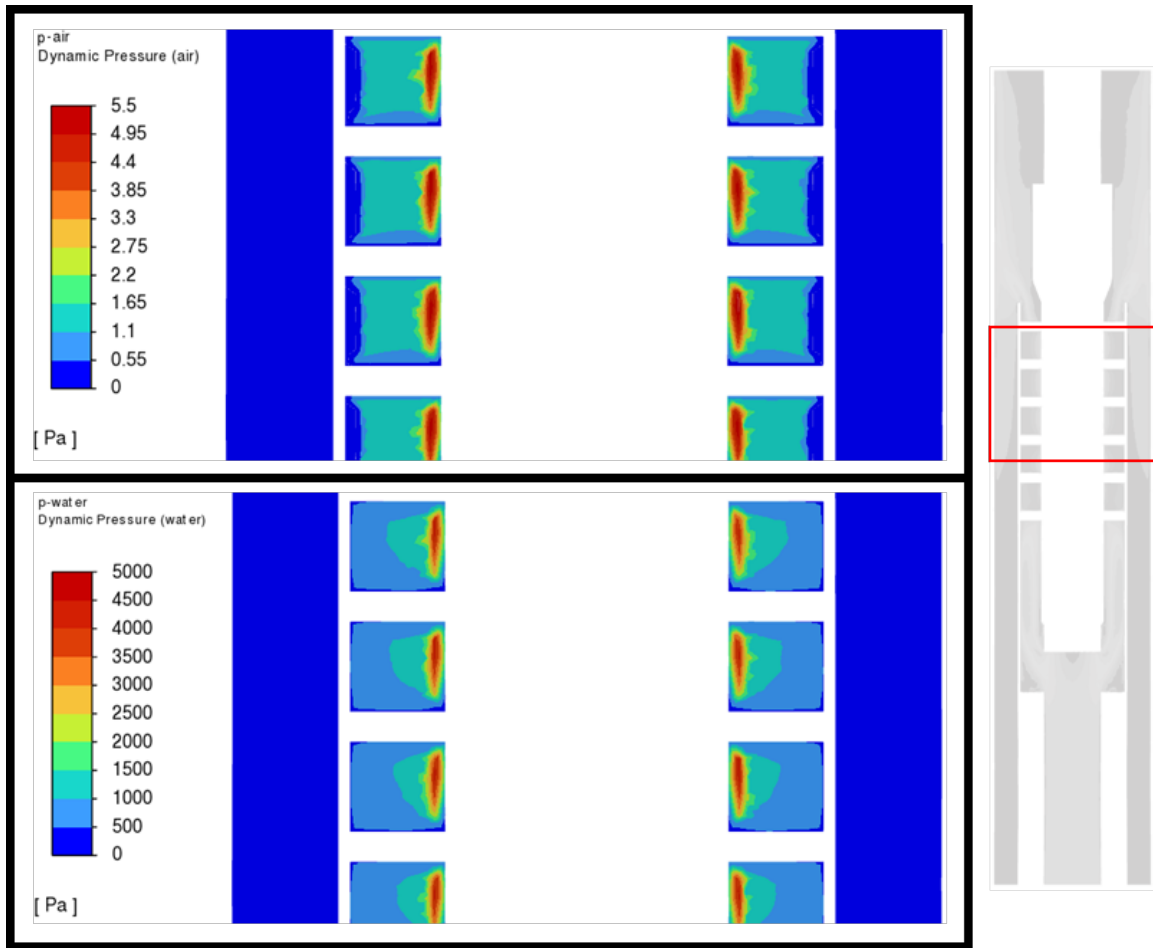


Figure 3.33. Dynamic pressure in the helix-type paths for case 13.

As mentioned before, case 13 has more similarities with the expected behavior of the separator. Pursuing more performance evaluation over cases with the conditions considered for this case is advised. Figure 3.34 displays the CFD results of case 13, with two obtained from laboratory testing over the same separator performed by Olubode (2021). The performance

following a logical trend and being close to the performance calculated from experiments can be seen.

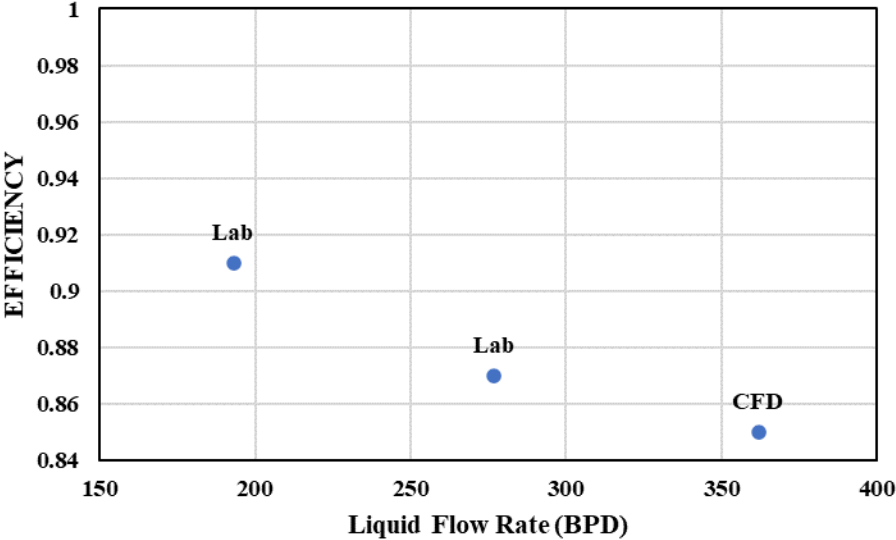


Figure 3.34. CFD vs Laboratory testing

CHAPTER 4: MACHINE LEARNING ANALYSIS

This Chapter depicts the efforts made in this study to collect data from the literature and build a machine learning algorithm. The algorithm is meant to work as a third method, besides laboratory testing and CFD simulation, to evaluate the performances of downhole centrifugal separators. The parameters used to feed the algorithm are dimensionless numbers associated with the variables of interest. The universality of the results is achieved through the use of these numbers. Besides the main machine learning algorithm, variable importance analysis is used to determine the parameters highly impacting the separators' efficiencies.

4.1. Data Collection

The extensive literature review in Chapter 2 of this study was used to gather laboratory test results. Only the data collected from downhole centrifugal separators were considered, excluding data from surface or gravitational separators. The data were collected from static and dynamic separators with different geometries and tested on different facilities. The data used to feed the machine learning algorithm were taken from the following studies: Alhanati (1993), Lackner (1997), Bohorquez et al. (2009), Wang et al. (2018), and Olubode et al. (2022). Five downhole centrifugal separators were analyzed in these studies, as observed in Figure 4.1:

- Rotary Shaft (Alhanati 1993 and Lackner 1997): It is a dynamic separator used in ESP applications. It is meant to handle high flow rates. It is attached to a shaft that induces rotational speed. It has a paddle-wheel-type rotator in its separating chamber. The

experimental set-up where the experiments of this separator were run is a flow loop mimicking the bottom of a well. It could handle liquid flow rates up to 1200 BPD, gas flow rates up to 240 MSCF/D, and pressures up to 400 psig. A 50 ft long 7 in. casing was used to house the separator, a motor, a shaft, and a seal. The testing procedure was controlled using a globe valve on the liquid return line (Alhanati, 1993). The gas and liquid inputs were controlled using a flow control valve and a by-pass hand control valve.

- Static Paddle Wheel (Alhanati 1993 and Lackner 1997): It is the same separator as the rotary shaft tested in the same facility described above but under static conditions with an immobile shaft. So, it is considered a static separator.
- Twister (Bohorquez et al., 2009): It is a static separator, which, through a swirling tube and reverse flow technology induces centrifugal separation. The testing facility used to test this separator was a closed loop apparatus with manually operated valves to control the flow. A 75 ft long 6 in, casing was used. A valve was used to obtain the desired hydrostatic pressure and liquid level inside the casing. When the valve is closed, the water accumulated inside the casing. Once the desired pressure is reached, the flow out of the casing is regulated maintaining the pressure and liquid level stable (Bohorquez, 2006).
- Accelerated Fan (Wang et al. 2018): It is a dynamic separator with an accelerating fan blade and spiral tube to induce the centrifugal motion upon the fluids. It also counts with reverse flow technology, due to the fact the liquid expelled back to the annulus flows down and re-enter the system through a shroud. Similar are the facility testing mentioned before, this separator was tested in a flow loop mimicking the well bottom.
- Double Helix (Olubode et al., 2022): It is a static separator that forces the fluids through two helix-type channels to induce centrifugal forces. It uses reverse flow technology. This

equipment is the same separator previously simulated in Chapter 3. The facility used for this separator is displayed in Figure 2.9. A compressor and tank were used to feed the facility, similar to the other separators; they have capacities of 1600 SCFM and 150 gallons, respectively. The separator is installed inside a 27 ft long 6 in. casing. The apparatus is controlled through a casing control valve that opens and closes to adjust the desired pressure and liquid level inside the separator.

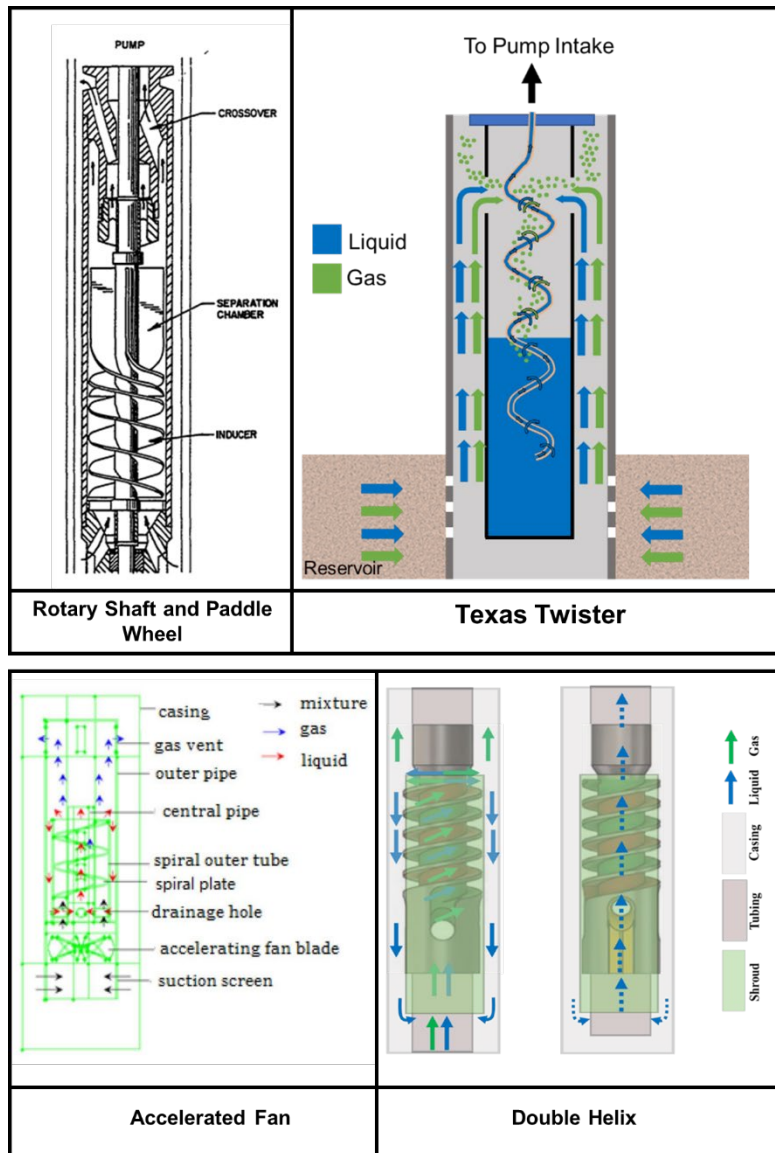


Figure 4.1. Downhole centrifugal separators used for data analysis. (Alhanati 1993, Lackner 1997, Bohorquez et al. 2009, Wang et al. 2018, and Olubode et al. 2022)

Table 4.1 summarizes the ranges of flow parameters for the data collected from these studies. The ranges represent the conditions under which each separator was tested. In addition, one geometry parameter is included, the area of separation. This area is the cross-sectional area of the separator in the section that the centrifugal separation occurs.

Table 4.1. Flow parameters for the data considered in the analysis (Osorio et al., 2023)

Separator Name	Separator Type	Liquid Flowrate (BPD)	Gas Flow rate (in-situ Mcf/d)	Pressure (psia)	Area of Separation (in ²)	No. of Data Points
Rotary Shaft	Dynamic	200 - 3000	1 - 35	100 - 350	12.6	131
Accelerated Fan	Dynamic	60 - 100	5 - 30	20 - 30	20.5	65
Paddle Wheel	Static	600 - 2700	4 - 25	120 - 250	12.6	16
Double Helix	Static	180 - 760	5 - 90	25 - 30	25	24
Texas Twister	Static	190 - 750	1.5 - 15	120 - 135	5.2	36

4.2. Operational and Geometrical Parameters

The purpose of the machine-learning algorithm is to forecast the separators' performance or efficiency for a given set of flow and geometrical parameters. The target separator efficiency is a known numerical variable for each collected data point from the literature. First, a data analysis was performed to stipulate the relation between some operational and geometric parameters and the separator's performance. There are two approaches to calculating the separation efficiency. One approach uses the liquid separation efficiency, which is the fraction of liquid successfully directed into the liquid outlet (the tubing-shroud annulus or pump intake). The other approach uses the gas separation efficiency, which is the fraction of gas successfully directed into the gas outlet (the tubing-casing annulus) (Osorio et al., 2023). For this study, the gas separation efficiency was used, calculated as shown in Eq. 4.1:

$$E = \frac{Q_{gv}}{Q_g} \quad (4.1)$$

Where E is the gas separation Efficiency, Q_{gv} is the successfully separated gas at in-situ conditions and Q_g is the total gas input to the system. Figure 4.2 displays the average efficiencies of the five analyzed separators. The overall efficiency of the five types of separators averages at 79%. The twister and double helix separators have the best average performances.

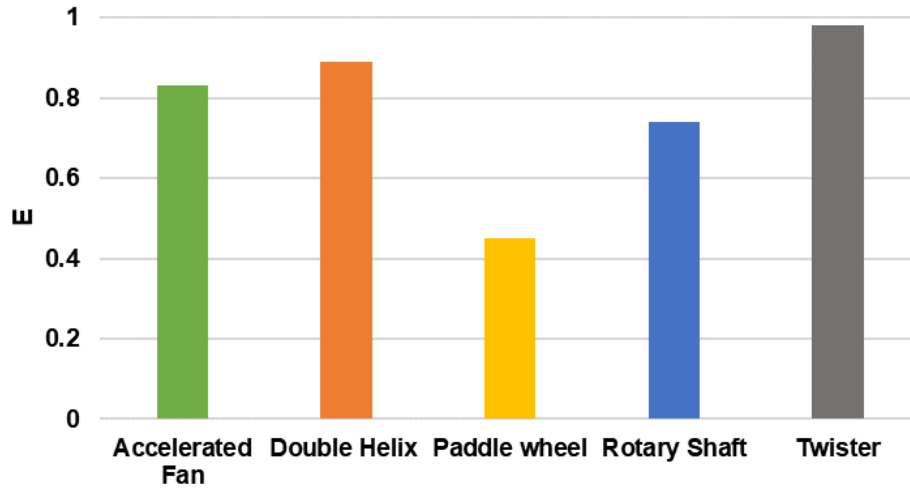


Figure 4.2. The average efficiencies of the tested separators

An initial analysis of the data was performed through superficial velocities. These variables allow a better comparison and scaling the gas-liquid separation process for different designs, sizes, and testing facilities. Superficial velocities of the liquid and gas are calculated using the separation area and in-situ liquid and gas flow rates. These factors directly impact two of the three main parameters influencing a separator's performance: turbulence and retention time. The superficial velocities were calculated using Eq. 4.2 and Eq 4.3.

$$v_{Sg} = \frac{Q_{g \text{ in-situ}}}{A} \left[\frac{\text{in}}{\text{s}} \right] \quad (4.2)$$

$$v_{SL} = \frac{Q_{l \text{ in-situ}}}{A} \left[\frac{\text{in}}{\text{s}} \right] \quad (4.3)$$

Where v_{SL} and v_{sg} are the superficial velocities of liquid and gas, $Q_{l \text{ in-situ}}$ and $Q_{g \text{ in-situ}}$ are the in-situ liquid and gas flow rates, and A is the separation area, calculated as the cross-sectional area of the separator. The liquid flow rate effect was given a closer look to understand its impact on the separator's performance. Figure 4.3 displays a bar plot of v_{SL} vs. efficiency and its distribution for different separators. The Rotary Shaft, Paddle Wheel, and Twister separators show a reducing separation efficiency when the v_{SL} increases. These separators were tested under similar v_{SL} conditions ranging from 5 to 25 in/s. The Twister separator performs better than the others, with an average efficiency of 20% larger than the overall average. The data points of these three separators cover liquid flow rates ranging from 190 to 3000 BPD.

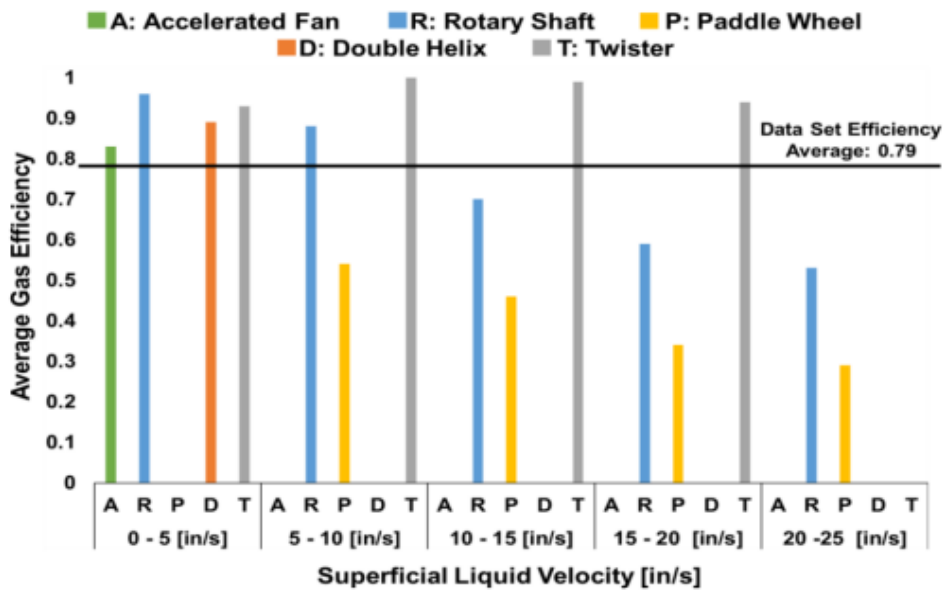


Figure 4.3. Gas Efficiency for Different Separator Types and v_{SL} ranges (Osorio et al., 2023)

The separators were tested under a wide range of liquid flow rates. As observed in Figure 4.4, the efficiencies deteriorate at higher liquid rates for all cases. The average efficiencies of the Paddle Wheel, Rotary Shaft, and Twister separators are 45%, 74%, and 99%, respectively (Osorio et al., 2023). Gas flow rates for these three separators vary similarly, with values no higher than

40 Mcf/d. These low gas rates do not impact the separation efficiency as much. This analysis shows that the liquid flow rate and separation geometry play significant roles in the separation process. The smaller testing liquid flow rates is the reason for the Twister, a static model, performing better than its counterparts at v_{SL} values higher than 5 in/s. The Paddle Wheel and Rotary Shaft separators have the same geometry. However, the efficiency of the dynamic Rotary Shaft separator is almost twice as much as the static Paddle Wheel. The added rotation of the Rotary Shaft helps enhance the centrifugal forces and improve the separation. The Paddle Wheel and Rotary Shaft separators were tested for higher liquid rates than the Twister, and their performances deteriorated with increased liquid rates. The performance of the Twister may also deteriorate at high liquid rates. However, more tests are required at higher rates to verify the trends (Osorio et al., 2023.)

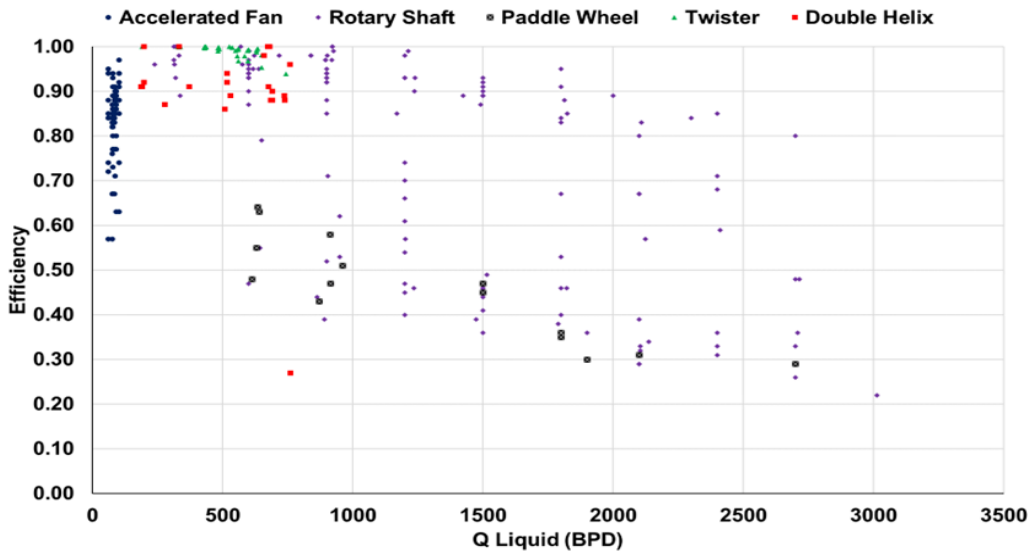


Figure 4.4. Liquid flow rate (BPD) vs. separation efficiency (Osorio et al., 2023)

The data display decreasing separation efficiencies with liquid flow rate increases for all the separators. The Accelerated Fan (dynamic), Rotary Shaft (dynamic), Double Helix (static), and Twister (static) were tested at lower v_{SL} values of 0-5 in/s, as shown in Figure 4.3. The average efficiencies of the Accelerated Fan, Rotary Shaft, Double Helix, and Twister for this low v_{SL} range

are 83%, 96%, 89%, and 99%, respectively. The Accelerated Fan does not perform as well as its counterparts. The Accelerated Fan and Rotary Shaft are dynamic models, but the second one has an average efficiency of 13% higher than the first. The Accelerated Fan was tested in liquid rates below 100 BPD, which can be the reason for its compromised performance. None of the other separators were tested in such low liquid flow rates.

The average efficiency of the Double Helix is 7% lower than the Rotary Shaft. Despite the Double Helix's larger separation area, the Rotary Shaft's dynamic nature enhances the centrifugal forces and efficiency. A dynamic separator requires added equipment to work. It needs to be attached to an ESP or a single downhole motor to generate the rotational movement, causing its implementation to be costlier. A static separator, such as the Double Helix, could be affordable and perform similarly to the Rotary Shaft for wells with high gas production (Osorio et al., 2023). After analyzing the separators' overall behaviors and understanding their geometries and testing conditions, a dimensional analysis was performed to generalize the analysis.

4.3. Dimensional Analysis

Besides the operational and geometrical parameters, the collected data include the fluid properties (densities, viscosities, and surface tension) and angular velocities for dynamic separators. Due to the number of variables in the data gathered, a dimensional analysis was performed. This method is a mathematical technique to understand and analyze complete physical phenomena. Performing a dimensional analysis helps to determine the key variables that govern the gas-liquid separation phenomenon. Additionally, it helps reduce the number of variables to focus on the most critical aspects and validate the experimental data.

The fundamental principle in dimensional analysis is the Buckingham Pi theorem. It states that if a mathematical equation can describe a physical phenomenon involving n variables and k independent dimensions (like length, mass, time, etc.), the relationship between these variables can be expressed in terms of $n-k$ dimensionless groups or numbers, known as π (pi) terms. This analysis aims to non-dimensionalize the flow parameters and make conclusions using different scales and operating conditions. For this purpose, the significant parameters influencing a separators' efficiency are discretized with their respective dimensions, as seen in Table 4.2.

Table 4.2. Dimensionless Analysis (Parameters, Units, and Dimensions)

Parameter		Unit	Dimension
Liquid Flowrate	$Q_{l\ in-situ}$	BPD	L^3/T
Gas Flowrate	$Q_{g\ in-situ}$	BPD	L^3/T
Liquid and Gas Densities	ρ_l, ρ_g	Lb-m/ft ³	M/L^3
Liquid and Gas Viscosities	μ_L, μ_G	cP	$M/L/T$
Mixture Density	ρ_m	Lb-m/ft ³	M/L^3
Liquid Surface Tension	σ_L	Lb-f/in	M/T^2
Angular Velocity	ω	Rad/s	$1/T$
Separation Area	A	m ²	L^2

Table 4.2 shows that 10 variables (n) are considered and described by 3 independent dimensions (k). According to the Buckingham Pi Theorem, the physical phenomenon can be expressed in 7 ($n-k$) dimensionless groups. An Importance Variable algorithm was run to reduce the number of variables and dimensionless numbers in play. This algorithm is a method used in machine learning to evaluate the contributions of different variables in a dataset, affecting a target variable, in this case the separation performance. It helps to detect which variables influence the outcome the most to make accurate predictions. After running the aforementioned algorithm, the following parameters were selected to conduct the dimensional analysis: $Q_{l\ in-situ}$, $Q_{g\ in-situ}$,

ρ_l , ρ_g , μ_l , μ_g , σ_L , A , and ω . These 9 parameters and their 3 dimensions (Mass, Length, and Time) resulted in 6 dimensionless numbers. After a physical analysis, four of the 6 dimensionless numbers (superficial liquid Weber number, superficial liquid Reynolds number, superficial gas Reynolds number, and mixture Taylor number) were selected as the most representative dimensionless numbers to feed the machine learning models. Besides these numbers, as some separators were tested under higher temperatures, a fifth dimensionless number was defined as the ratio of the test temperature over the standard temperature $\left(\frac{T}{T_s}\right)$ to analyze its effect. The following is a short description of the dimensionless numbers.

4.3.1. Weber Number

The Weber number (We) relates inertial and surface tension forces. When $We < 1$, the surface tension forces dominate, and the spherical droplets or bubbles tend to grow. When $We > 1$, the inertial forces dominate, and the fluid tends to break into tiny droplets or sprays. Larger bubbles or droplets positively affect the separator's performance. Meanwhile, tiny bubbles contribute to the separator's inefficiency (Osorio et al., 2023). Equation 4.4 represents the superficial liquid Weber number, We_{SL} .

$$We_{SL} = \frac{\rho_L * v_{SL}^2 * d_{sep}}{\sigma_L} \quad (4.4)$$

4.3.2. Reynolds Number

Reynolds number (Re) relates inertial and viscous forces. Inertial forces are generated from the tendency of a fluid to change its state of motion. They dominate the flow when velocities are more significant. Meanwhile, viscous forces are generated from the internal friction on the fluid,

opposing the relative motion of adjacent fluid layers. They dominate the flow at higher viscosities and smaller velocities. Two Reynolds numbers are considered here, superficial liquid and gas numbers, calculated with the respective properties of each fluid. Equations 4.5 and 4.6 describe the superficial liquid and gas Reynolds numbers, respectively (Osorio et al., 2023).

$$Re_{SL} = \frac{\rho_L * v_{SL} * d_{sep}}{\mu_L} \quad (4.5)$$

$$Re_{SG} = \frac{\rho_G * v_{SG} * d_{sep}}{\mu_G} \quad (4.6)$$

Where ρ is the density of the fluid, μ is the viscosity of the fluid, v_S is the corresponding superficial velocity, and d_{sep} is the relative diameter of separation based on the cross-sectional area of separation, mentioned before in Equations 4.2 and 4.3.

4.3.3. Taylor Number

Like the Reynolds number, Taylor number (Ta) relates inertial and viscous forces. However, this dimensionless number considers the inertial forces of the rotational fluid motion. The flow tends to be stable at low Taylor numbers due to the dominating viscous forces. Meanwhile, the flow is typically unstable and turbulent at high Taylor numbers when inertial forces dominate the flow. The transition from stable to unstable flow can significantly affect the flow behavior and mixing. Equation 4.7 describes the Taylor number definition used in this study. The definition uses the mixture density and viscosity and the rotational speed of the separator (Ω).

$$Ta = \frac{4 * \Omega^2 * d_{sep}^4 * \rho_m^2}{\mu_m^2} \quad (4.7)$$

4.4. Machine Learning Model Application

Machine learning has become a powerful tool in the past decade to train algorithms using data. The training enables an algorithm to make predictions of a desired parameter, the separator's performance for this case. The algorithm built in this thesis is meant to provide a tool that predicts the performance of a separator according to operational conditions, geometric parameters, and fluid properties. However, a vital step before implementing machine learning models is to process and clean the data.

4.4.1. Data Preprocessing

Before the algorithm generation, the data must be preprocessed. This includes handling the missing data, normalizing, scaling, categorical variables, and removing the outliers. Seven variables are parts of the preprocessed data: separator type, We_{SL} , Re_{Sg} , Re_{SL} , Ta , temperature ratio, and separator's efficiency. The five dimensionless numbers are the input parameters, and the efficiency is the output parameter or the target variable the algorithm is trained to predict.

There are 272 rows of data included in the algorithm.. To generate a machine learning algorithm, this data needs to be randomly split. 80% of the data were used as the training set, feeding the machine-learning models with these data points to generate an appropriate algorithm. The other 20% were used to test the model. The input parameters of these data were inserted into the algorithm, evaluating the accuracy of the output prediction. As mentioned, the data used for this machine-learning algorithm were obtained from five separator laboratory tests. Each separator contributes a certain percentage to the overall collection of data points. By stratifying the data according to "separator type," the data points were adequately distributed during the split process. The shares of the data from each separator used in the testing and training datasets is shown in Table 4.3. The quantity of data points from each separator was proportionally divided during the

data split. As a result, the percentages presented for each separator in Table 4.3 do not differ much between the training and testing sets.

Table 4.3. Data split percentages

Separator Type	Complete data	Training Set (80%)	Testing Set (20%)
Rotary Shaft	0.485	0.486	0.481
Accelerated Fan	0.241	0.241	0.241
Twister	0.133	0.134	0.130
Double Helix	0.001	0.079	0.093
Paddle Wheel	0.059	0.060	0.556

Some of the techniques used during the data preprocessing include outliers' removal, one-hot encoding, Min-Max scaling, and the Pipeline function. The "separator type" input parameter of the data is a categorical variable, meaning it does not have a numerical value. A One-Hot encoding allows the categorical data to be represented as binary vectors, where each binary digit corresponds to a category. Additionally, some dimensionless numbers have significantly larger values than others, such as Taylor Number, which can have values 13th orders higher than Weber number. This vast difference between the numerical scales can mask the real influences of the variables, causing variables with larger numerical values to be falsely more representative. This issue was solved using statistical scaling and normalizing techniques like the Min-Max scaler. This technique scales each numerical variable within a specified range, from 0 to 1.

Only the training set was scaled to avoid data leakage. Data leakage is an event where data points meant to be used in testing are inadvertently used during training, making the generated algorithm biased and performing better than it should. If the entire dataset is scaled, information from the testing data will be given to the training data. In addition, the pipeline function was used to prevent potential data leakage that influences the results. A pipeline function is a tool or

construct that combines multiple data processing and modeling steps into a single entity. This function ensures that data preprocessing steps are applied consistently to the training and testing data, avoiding potential data leakage.

4.4.2. Machine Learning Models

Machine learning models or algorithms can be divided into supervised, unsupervised, semi-supervised, and reinforcement learning. The choice of a suitable model depends on the target variables or outputs being studied. As the target variable for this project is the separator's efficiency, a known value measured in the laboratory, supervised learning models can be used to generate a predictor algorithm. Supervised models are divided into regression and classification models. A classification model deals with categorical target data, while a regression model deals with continuous target data. The separation efficiency is a continuous variable calculated using Eq. 1, making the regression models the best choices to generate an algorithm for this study.

Various regression models were used, with Linear Regression as the base model. Linear Regression is a weighted combination of the input variables to generate the target. Other models include Random Forest Regressor, an ensemble method that generates average predictions; k-nearest neighbors' Regression (KNN Regressor), which uses 'K' nearest neighbors to predict output values; and Support Vector Machine (SVM) Regression, a supervised algorithm that finds linear boundaries to predict new data points. The final tested model is the Voting Regressor, which combines predictions from the other models. The strength of the Voting Regressor is in using uncorrelated models as inputs (Osorio et al., 2023).

There are three commonly used metrics to assess the performance of a machine learning algorithm: R2, Adjusted R2, and Root Mean Squared Error (RMSE). R2 measures how well the

model explains the variability in the output variable. It ranges from 0 to 1, 1 meaning that the model successfully explains the totality of the variance, and 0 indicating the model does not explain any of the variance. This metric can be misleading as it tends to increase with the number of inputs or predictors. Adjusted R² addresses this issue by considering the number of predictors in the model and penalizing it for adding unnecessary variables. Very large R² or Adjusted R² values should be avoided as they can be a sign of overfitting. Overfitting leads the model to perform well on the training data but poorly on new unseen data, which is the aim of the model. Finally, RMSE measures the average error between the actual and predicted values of the target variable. Like R², RMSE ranges between 0 and 1, but lower values indicate better model performances.

An indispensable technique to assess the performance of any algorithm is K-Fold cross-validation. This method randomly splits the data into K smaller subsets, also known as folds. The program generates K number of algorithms where each subset is used as test data while the other data are used as training data. After the results from the K iterations are obtained, they are averaged and evaluated according to the aforementioned metrics. A 5-fold cross validation technique was used to evaluate the results of this study.

4.5. Modeling Results

Table 4.4 displays the results obtained when cross validating all the models used at this study. The baseline model used was linear Regression. This model achieved an adjusted R² value of 0.178 with cross-validation. It implies that the model explains 17.8% of the variance in the gas separation efficiency with the predictor variables used. Linear Regression achieves an RMSE value of 0.184 in cross-validation. It is evident from the R² and RMSE values that linear Regression cannot accurately learn the complexity of the data.

Non-linear machine learning algorithms like Random Forest, SVM Regressor, and KNN perform better than the Linear Regression baseline. Voting Regressor is an ensemble of Random Forest, KNN, and SVM Regressors. Its prediction is the average of all three models and provides the best cross-validation metrics followed by the SVM regressor. The Voting Regressor has the best cross-validation R2 value of all the models, 0.59. Adjusted R2 value penalizes R2 for increasing the number of predictors, resulting in a cross-validation value of 0.535 and an RMSE value of 0.138. This implies that the model can represent 53.5% of the variance in separation efficiency with an error of 13.8% (Osorio et al., 2023).

Table 4.4. Machine Learning Results

Model	5-Fold Cross-Validation			Train Set			Test Set		
	R ²	Adj R ²	RMSE	R ²	Adj R ²	RMSE	R ²	Adj R ²	RMSE
Linear Regression	0.275	0.178	0.184	0.361	0.345	0.177	0.48	0.425	0.155
Random Forest	0.557	0.498	0.144	0.887	0.885	0.074	0.748	0.722	0.108
KNN	0.550	0.490	0.145	0.748	0.743	0.111	0.708	0.677	0.116
SVM Regressor	0.530	0.467	0.148	0.712	0.704	0.119	0.672	0.638	0.123
Voting	0.590	0.535	0.138	0.814	0.81	0.095	0.744	0.718	0.109

From Table 4.4., the most important results to analyzed is the 5-fold cross-validation Figure 4.5 shows the predicted efficiencies of the four models: Random Forest, KNN, SVM, and the Voting Regressor. The diagonal lines represent perfectly predicted values. Despite the scatter in the data, the separation efficiency predictions are acceptable in some cases (Osorio et al., 2023). Adjusted R2 larger than 0.5 can be considered acceptable as more than 50% of the data is being captured by the model. According to the literature, adjusted R2 larger than 0.8 can be considered good results that computed the behavior of the predicted variable, although this score varies from author to author. The Adjusted R2 is the Random Forest, KNN, and voting and close to 0.5, making

them three acceptable models with potential for improvement when more data is added to the algorithm generation.

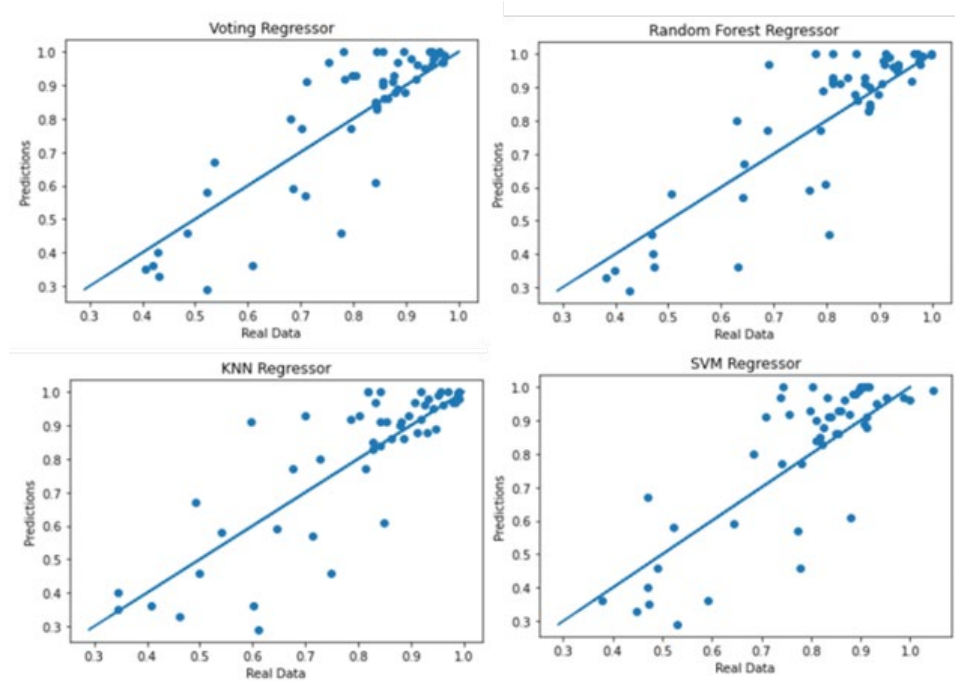


Figure 4.5. Results of the Machine Learning Models

4.6. Variable Importance

A Random Forest Variable Importance algorithm was used to evaluate the significance of the selected dimensionless numbers, as shown in Figure 4.6. It is observed that We_{SL} and Re_{SL} are the most important variables for the analysis, with measures of 37% and 29%, respectively. The influences of these numbers highly dominate the performance of the separator. The Ta and T/Ts numbers similarly influence the results, while Re_{SL} is less significant. In summary, a balance of the inertial gas forces (represented by Re_{SG}) and surface liquid forces (represented by We_{SL}) determines the separation efficiency.

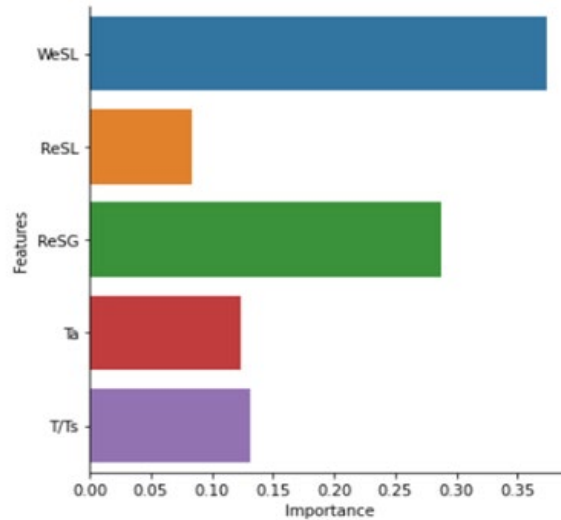


Figure 4.6. Bar plot of feature importance.

We_{SL} is the only dimensionless variable used, including the impact of surface tension forces on the separator's dynamics. The significance of this number means that the liquid surface tension greatly impacts a separator's performance. Surface tension is responsible for shaping the bubbles or droplets of fluids. As the surface tension of a liquid decreases in comparison to the body forces, represented by higher Weber numbers, there is a tendency for larger bubbles to break into smaller bubbles. Tiny bubbles or droplets remain suspended in the continuous fluid for relatively long periods, making them tougher to separate. Thus, larger We_{SL} values are correlated to the formation of tiny bubbles in the system, contributing to separation inefficiency (Osorio et al., 2023).

Figure 4.7 illustrates the negative impact of We_{SL} on the separator performances. It is worth noting that the Accelerated Fan and Double Helix do not exhibit this negative impact at lower ranges of We_{SL} values. However, the other three separators, operating at higher ranges of We_{SL} values, show a clear decline in the separator efficiency with the increase in the Weber number.

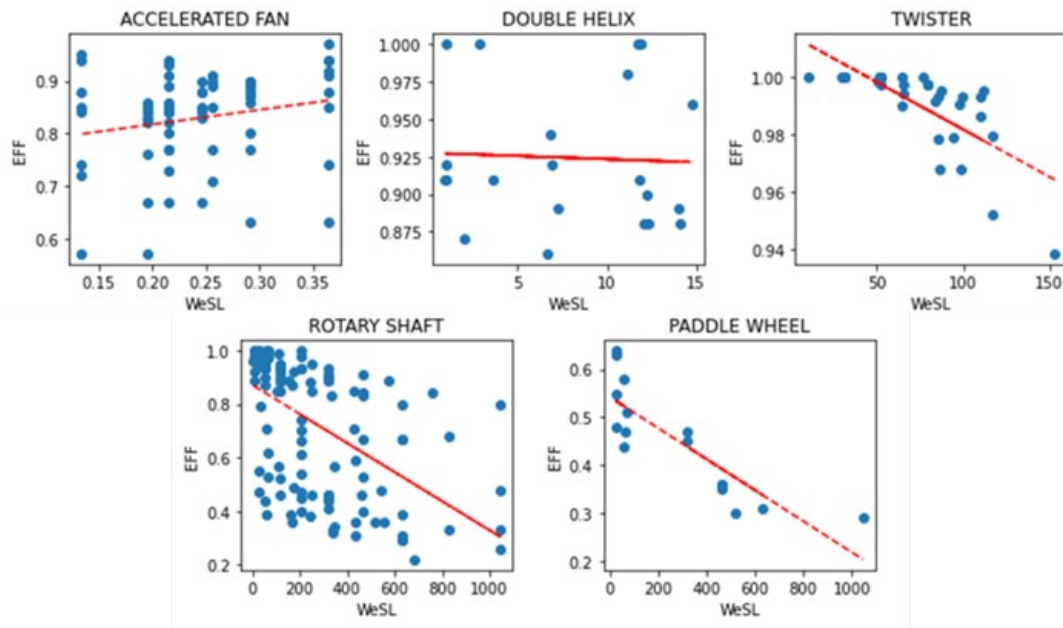


Figure 4.7. Weber Number impact over separators' efficiency.

The We_{SL} does not affect the efficiency of the Accelerated Fan separator similarly to its counterparts. By contrast, the We_{SL} seems to have a slightly positive effect on its efficiency. The separator was tested under lower liquid flow rates with $We_{SL} < 0.4$. It can be concluded that another dimensionless number dominates the performance of this separator due to its different operating conditions. A Random Forest Variable Importance algorithm was run, using only the Accelerated Fan data, to analyze the above hypothesis. The results can be seen in Figure 4.8. The Figure illustrates that the superficial gas Reynolds number (Re_{SG}) significantly impacts this separator's performance, showing the effects of inertial gas forces at lower liquid Weber numbers.

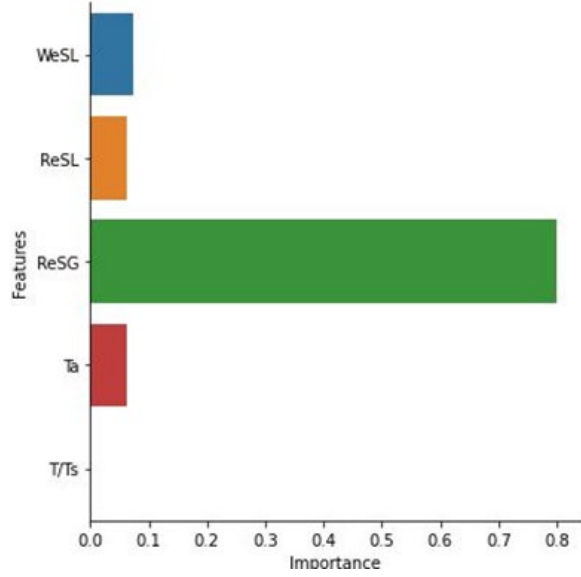


Figure 4.8. Bar plot for the feature of importance for the Accelerated Fan.

Figure 4.9 displays the efficiency plot vs. Re_{SG} for the Accelerated Fan separator. The trend in the plot shows that gas flow impacts the separation performance more than liquid in such low flow rates. The separation initially benefits from an increase in Re_{SG} or the gas turbulence up to a Re_{SG} of 6000. This phenomenon may be due to a reduction in the gas drag coefficient. The effect of Re_{SG} becomes minimized at higher Reynolds numbers. If the Accelerated Fan is tested under higher liquid rates, its performance may resemble its counterparts (Osorio et al., 2023).

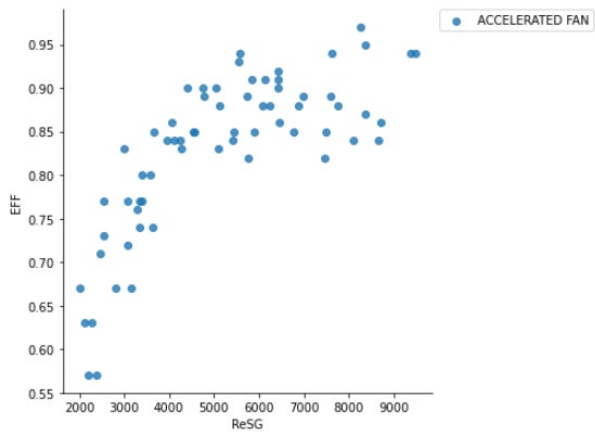


Figure 4.9. Gas Reynolds Number impact over the accelerated fan separator’s performance

Besides being the most important variable for the Accelerated Fan, Re_{SG} is also the second most important variable for the performances of the other separators, as seen in Figure 4.6. Re_{SG} represents the gas inertial forces and turbulence. Figure 4.10 displays the effect of Re_{SG} on the efficiencies of the other four analyzed separators. There is a decreasing trend in the separator performances by increasing Re_{SG} , and hence the gas turbulence, which is expected.

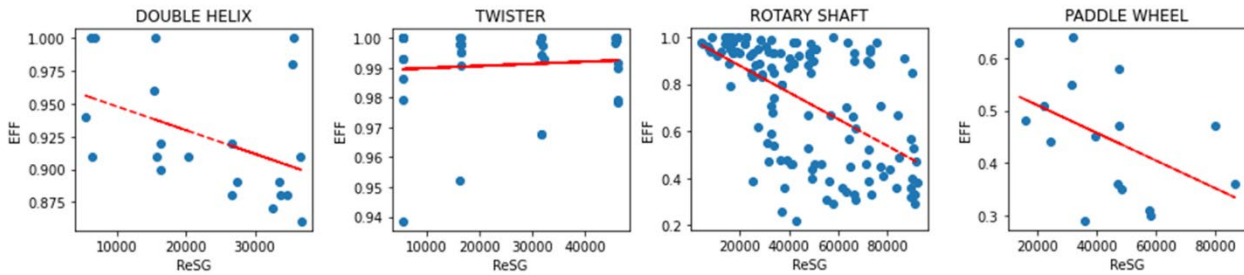


Figure 4.10. Gas Reynolds Number impact over the efficiencies of the separators

As seen in Figure 4.10, the twister separator has the highest efficiency. This static centrifugal separator has a reverse flow geometry, like the double helix separator. The Twister was tested under low liquid and gas flow rates, not surpassing 750 BPD and 15 Mcf/d, respectively. A simple explanation for the better performance of Twister is the low testing flow rates. Its performance will possibly decline at higher liquid and gas flow rates. However, it is important to notice that it performs better than the other separators by up to 20% under similar low conditions. This performance makes the twister separator an attractive option for low-production wells, particularly because its static nature makes it cheaper (Osorio et al., 2023).

CHAPTER 5: FINAL REMARKS

This chapter outlines the main outcomes of this study. The results obtained are briefly discussed, and the main conclusion are presented. In addition, some recommendations are provided for future works on this topic, considering the current work.

5.1. Summary and Conclusions

- An extensive review was conducted on gas-liquid separation literature. The information was compiled on the techniques used to evaluate the separation performances of different types of centrifugal separators: CFD and laboratory testing. This investigation allowed to conclude the necessity of entering a new type of evaluation method: machine learning.
- Downhole centrifugal separators can be classified into dynamic and static models. They enhance the primary gravitational separation through imparted centrifugal forces.
- A 3-D model was built to conduct CFD simulations for flow through a static centrifugal downhole separator. CAD was used to generate the geometry. The solid and fluid parts were extracted for CFD analysis. The fluid domain was a simplified control volume of the gas-liquid separation system (casing, tubing, and shroud).
- A mesh for the fluid domain was generated by testing various mesh types and tweaking the parameters. After conducting a grid independence analysis, a mesh with 152,446 cells was chosen for its excellent quality and short simulation time. Further examination of the y+

values in the selected mesh confirmed a suitable boundary layer, falling within the range of 5 to 30 across the domain.

- A total of 13 single-phase and multiphase cases were successfully simulated. These simulations proved instrumental in gaining insights into the separator's behavior.

- When setting pressure boundaries, for single-phase water or gas flow, the fluid naturally chose the outlet with the least resistance, which happened to be the top outlet with a larger cross-sectional area. The distribution was more balanced in multiphase flow cases, with water exiting entirely through the bottom outlet.

- Turbulence was observed in sections where eddies or vortex cores were formed, amplified at the corners of the helix paths. These areas with turbulence could benefit from a redesign to ensure a smoother flow inside the separator.

- Velocity and dynamic pressure contours were compared across cases 1 to 8. In all instances, both variables were higher in the outermost sections of the helix-type paths, with velocities reaching approximately five times the fluid's inlet velocity. While cases 1 to 4 used pressure outlets, cases 5 to 8 were constrained with imposed mass-flow outlets. The comparison revealed that cases with forced boundaries exhibited lower velocities, particularly in the expelling back section. This behavior suggests the need for controlled velocities to achieve the desired separation.

- It was observed that after the fluid is expelled from the helix-type paths, it maintains a rotational motion towards the outlets. This rotational motion can create low-pressure pockets in the innermost sections of the outlets, enabling reversed flow.

- The volume fraction contours in the multiphase cases (10-13) reveal the impact of centrifugal forces, leading to the separation of the fluids based on density difference. These contours affirm that the separator is functioning as intended, with water predominantly located in the outermost sections of the helix-type paths and air in the innermost sections.
- The importance of pressure control was studied in the multiphase flow cases. It was observed that the lower the pressure difference, the air tends to come through the top outlet to counteract friction losses.
- Case 13 was observed to have a well-balanced behavior where 85% of the air left through the top outlet, and 98.3% of the water left through the bottom outlet. This case is set at a good starting point for future performance evaluation with different GVF as displays the importance of having a good balance of pressure between the two outlets.
- A dataset was gathered of laboratory tests performed on five downhole centrifugal separators from the open literature. The average efficiency of the dataset, showing the ratio of the inlet gas successfully vented into the casing, is 79%.
- A Buckingham Pi Theorem dimensional analysis was conducted to determine the dimensionless numbers describing the governing forces on downhole centrifugal separators. These dimensionless numbers are We_{SL} , Re_{SG} , Re_{SL} , Ta , and T/T_{SC} .
- A Random Forest algorithm was used to evaluate the impacts of dimensionless variables on the efficiency of separators. We_{SL} is the most critical variable affecting the performance of a centrifugal separator, with 37% importance. Re_{SG} is the second influencing factor, with an importance of 29%.

- The separator's efficiency decreases with an increase in the liquid flow rate. Being tested at very low liquid rates, the efficiency of the accelerated fan decreases at low liquid and gas rates due to the possible changes in liquid-gas flow regimes.
- The Twister separator performs better than the other separators under similar low conditions by a difference up to 20%, making it a low-cost option for low-production wells.
- The separator's efficiency decreases with an increase in the liquid flow rate. In addition, the efficiency starts to decrease at very low liquid rates, below 100 BPD. The optimal range of operation is found to be between 200-700 BPD.
- A predictor model was created using machine learning and the gathered data. After testing several machine learning models, the Voting Regressor was selected as the best predictor for this dataset. It has a cross-validated adjusted R2 of 0.535 and RMSE of 0.138 on the set. This means that the predictor can represent 53.5% of the variance in gas separation efficiency data with an error of 13.8%. More data points must be added to the model to increase the prediction capability of the algorithm.

5.2. Recommendations

- Re-design the separator by enlarging the outlets and reducing areas of turbulence. According to CFD experts, enlarging the outlets might mitigate the rotational behavior when fluids are expelled from the helixes, promoting better velocity development of the fluid. This is done by modifying the CAD modeling.
- Simulate more cases with different GVF scenarios and using other types of fluids, such as oil and natural gas.

- Perform a sensitivity analysis on the operational parameters such as separator length, pitch, tip diameter, and blade thickness to improve equipment performance.
- Include more data points in the model to make a more robust predictor and improve the quality measures, such as adjusted R2.

REFERENCES

Abbariki, Ghasem , Riasi, Alireza , and Ali Rezghi. "Surrogate-Based Optimization for the Design of Rotary Gas Separator in ESP Systems." *SPE Prod & Oper* 35 (2020): 497–509. doi: <https://doi.org/10.2118/201188-PA>

Alhanati, F. (1993). Bottomhole Gas Separation Efficiency in Electrical Submersible Pump Installations.

Alhanati, F. J. S. and Doty, D. R. 1994. A Simple Model for the Efficiency of Rotary Separators. Presented at the SPE Annual Technical Conference and Exhibition, New Orleans, 25–28 September. SPE-28525-MS. <https://doi.org/10.2118/28525-MS>.

Alireza Bahadori, Chapter 4 - Gas–Liquid Separators, Editor(s): Alireza Bahadori, *Natural Gas Processing*, Gulf Professional Publishing, 2014, Pages 151-222, ISBN 9780080999715, <https://doi.org/10.1016/B978-0-08-099971-5.00004-0>.

Bohorquez (2006). Performance of Gravity Driven and Centrifugal Down-Hole Gas Separators for Continuous and Intermittent Flow.

Bohorquez, R.R., Ananaba, O.V., Alabi, O.A., Podio, A.L., Lisigurski, O., and Guzman, M. (2009, November1). Laboratory Testing of Downhole Gas Separators. *Society of Petroleum Engineers*. doi:10.2118/109532-PA.

Bommer, P. M. and Podio, A. L. 2015. *The Beam Lift Handbook*. Austin, Texas, USA: Petroleum Extension Service, Continuing and Innovative Education, University of Texas at Austin.

Darbani, S., Riasi, A., and Nejat, A.2015. The Parametric Study of an Electrical Submersible Pump Rotary Gas Separator under Two-Phase Flow Condition. *Energy Equip Syst*3 (1): 33–44. <https://doi.org/10.22059/ees.2015.13909>.

Derakhshan, Shahram , Riahi, Fazel , and Mohamad Bashiri. "Efficiency Improvement of a Rotary Gas Separator by Parametric Study and Gas/Liquid-Flow Analysis." *SPE Prod & Oper* 33 (2018): 320–335. doi: <https://doi.org/10.2118/187966-PA>

do Vale, O.R., Garcia, J.E., and M. Villa. "VASPS Installation and Operation at Campos Basin." Paper presented at the Offshore Technology Conference, Houston, Texas, May 2002. doi: <https://doi.org/10.4043/14003-MS>

Gabor Takacs, Chapter 4 - Use of ESP Equipment in Special Conditions, Editor(s): Gabor Takacs, *Electrical Submersible Pumps Manual (Second Edition)*, Gulf Professional Publishing, 2018, Pages 153-240, ISBN 9780128145708, <https://doi.org/10.1016/B978-0-12-814570-8.00004-0>.

Harun, A. F., Prado, M. G., Shirazi, S. A. et al. . 2002. An Improved Model for Predicting Separation Efficiency of a Rotary Gas Separator in ESP Systems. *SPE Prod & Fac*17 (2): 78–83. SPE-77279-PA. <https://doi.org/10.2118/77279-PA>.

Harun, A. F., Prado, M. G., Shirazi, S. A. et al. . 2004. Two-Phase Flow Modeling of Inducers. *J Energy Resour Technol*126 (2): 140–148. <https://doi.org/10.1115/1.1738124>.

Hreiz, R., et al., Hydrodynamics and velocity measurements in gas–liquid swirling flows in cylindrical cyclones. *Chem. Eng. Res. Des.* (2014), <http://dx.doi.org/10.1016/j.cherd.2014.02.029>

Rainier Hreiz, Richard Lainé, Jing Wu, Cécile Lemaitre, Caroline Gentric, Denis Fünfschilling, On the effect of the nozzle design on the performances of gas–liquid cylindrical cyclone separators, *International Journal of Multiphase Flow*, Volume 58, 2014, Pages 15-26, ISSN 0301-9322, <https://doi.org/10.1016/j.ijmultiphaseflow.2013.08.006>.

Hu, H. H. (2012). Computational fluid dynamics. In *Fluid mechanics* (pp. 421-472). Academic Press.

Kharoua, N., Khezzar, L., AlShehhi, M., & Meribout, M. (2016). Numerical Simulation of a New Gas-Liquid Separator.

Kou, J., & Li, Z. (2021). Numerical simulation of new axial flow gas-liquid separator. *Processes*, 10(1), 64.

Kouba, Gene & Shirazi, Siamack. (1995). Design and Performance of Gas Liquid Cylindrical Cyclone Separators.

Lackner, G. (1997). The Effect of Viscosity on Downhole Gas Separation in a Rotary Gas Separator.

Lackner, G., Doty, D. R., Shirazi, S. A. et al. 2002. Effect of Viscosity on Downhole Gas Separation in a Rotary Gas Separator. *SPE Prod & Fac* 17 (3): 184–191. SPE-79076-PA. <https://doi.org/10.2118/79076-PA>.

Lea, James F., and J.L. Bearden. "Effect of Gaseous Fluids on Submersible Pump Performance." *J Pet Technol* 34 (1982): 2922–2930. doi: <https://doi.org/10.2118/9218-PA>

Li, C., Li, Z., Zhang, Y., & Li, B. Numerical Simulation and Experimental Study of Two-Phase Flow in Downhole Spiral Gas-Liquid Separator. *Frontiers in Earth Science*, 11, 1209743.

Lopez, Jorge , Pereyra, Eduardo , and Cem Sarica. "An Experimental Investigation of Dynamic Behavior of Gravity-Driven Downhole Separators." Paper presented at the SPE Annual Technical Conference and Exhibition, Calgary, Alberta, Canada, September 2019. doi: <https://doi.org/10.2118/196197-MS>

Lopez, Jorge , Pereyra, Eduardo , and Cem Sarica. "An Experimental Investigation of a Highly Deviated Shroud Type Downhole Separators." Paper presented at the SPE Artificial Lift Conference and Exhibition - Americas, Virtual, November 2020. doi: <https://doi.org/10.2118/201127-MS>

McCoy, J. N.; Patterson, J.; and Podio, A. L. (2005). A laboratory study with field data of downhole gas separators. In Proceedings of the 6th Canadian International Petroleum Conference. June, 7-9. Calgary, Alberta. Paper 2005-254. Petroleum Society.

McCoy, J. M., Patterson, J., & Podio, A. L. (2007). Downhole gas separators - A laboratory and field study. *Journal of Canadian Petroleum Technology*, 46(5), 48–54. <https://doi.org/10.2118/07-05-05>

McCoy, J.N.. N., Podio, A.L.. L., Rowlan, O.L.. L., and D.. Becker. "Evaluation and Performance of Packer-Type Downhole Gas Separators." *SPE Prod & Oper* 30 (2015): 236–242. doi: <https://doi.org/10.2118/164510-PA>

Meng, L., Gao, S., Wei, D., Cui, B., Shen, Y., Song, Z., & Yuan, J. (2021). Effects of cross-sectional geometry on flow characteristics in spiral separators. *Separation Science and Technology*, 56(17), 2967-2977.

M.O. Olubode, P. Iradukunda, H. Karami, T. Podio, J.N. McCoy, Experimental analysis of centrifugal downhole separators in boosting artificial lift performance, *Journal of Natural Gas*

Science and Engineering, Volume 99, 2022, 104408, ISSN 1875-5100,
<https://doi.org/10.1016/j.jngse.2022.104408>.

Nieuwstadt, F. T., & Dirkzwager, M. (1995). A fluid mechanics model for an axial cyclone separator. *Industrial & engineering chemistry research*, 34(10), 3399-3404.

Ogunsina, O. O., and M. L. Wiggins. "A Review of Downhole Separation Technology." Paper presented at the SPE Production Operations Symposium, Oklahoma City, Oklahoma, April 2005. doi: <https://doi.org/10.2118/94276-MS>

Olaleye, O. E., Van Ombele, B., Li, X., & Adeshina, O. A. (2022). CFD modeling analysis of a vertical gas liquid separator. *Journal of Petroleum Science and Engineering*, 216, 110733.

Olubode, M. (2021). *Experimental Analysis of Centrifugal Downhole Separators in Boosting Artificial Lift Performance* / by Michael Olayemi Olubode.

Olubode, Michael, Osorio, Laura, Karami, Hamidreza, McCoy, Jim, and Tony Podio. "Experimental Comparison of Two Downhole Separators in Boosting Artificial Lift Performance." Paper presented at the SPE Artificial Lift Conference and Exhibition - Americas, Galveston, Texas, USA, August 2022. doi: <https://doi.org/10.2118/209723-MS>

Osorio Ojeda, Laura Camila Osorio. "Application of Machine Learning and Dimensional Analysis to Evaluate the Performances of Various Downhole Centrifugal Separator Types." Paper presented at the SPE Annual Technical Conference and Exhibition, San Antonio, Texas, USA, October 2023. doi: <https://doi.org/10.2118/217484-STU>

Osorio Ojeda, Laura Camila, Olubode, Michael, Karami, Hamidreza, and Tony Podio. "Application of Machine Learning to Evaluate the Performances of Various Downhole Centrifugal Separator Types in Oil and Gas Production Systems." Paper presented at the SPE Oklahoma City

Oil and Gas Symposium, Oklahoma City, Oklahoma, USA, April 2023. doi: <https://doi.org/10.2118/213059-MS>

Praveen Adiraju (2023). Artificial Lift Applications to Unconventional Reservoirs

Qiu, S., Wang, G., Zhou, S., Liu, Q., Zhong, L., & Wang, L. (2020). The downhole hydrocyclone separator for purifying natural gas hydrate: structure design, optimization, and performance. *Separation Science and Technology*, 55(3), 564-574.

Rosa, Eugenio & França, F.A & Ribeiro, G.S. (2001). The cyclone gas-liquid separator: Operation and mechanistic modeling. *Journal of Petroleum Science and Engineering*. 32. 87-101. 10.1016/S0920-4105(01)00152-8.

Sharma, A. (2019). Experimental evaluation of a centrifugal packer-type downhole separator. In Shareok (Vol. 4, Issue 1). <https://hdl.handle.net/11244/323223>

Shukla, S. K., Shukla, P., & Ghosh, P. (2011). Evaluation of numerical schemes using different simulation methods for the continuous phase modeling of cyclone separators. *Advanced Powder Technology*, 22(2), 209-219.

Saeid Mokhatab, William A. Poe, John Y. Mak, Chapter 4 - Phase Separation, Editor(s): Saeid Mokhatab, William A. Poe, John Y. Mak, *Handbook of Natural Gas Transmission and Processing (Third Edition)*, Gulf Professional Publishing, 2015, Pages 137-167, ISBN 9780128014998, <https://doi.org/10.1016/B978-0-12-801499-8.00004-3>.

Sharma, Ashutosh , Iradukunda, Platin , Karami, Hamidreza , McCoy, J. N., Podio, A. L., and Catalin Teodoriu. "Experimental Evaluation of a Prototype Centrifugal Packer-Type Downhole Separator." Paper presented at the SPE Artificial Lift Conference and Exhibition - Americas, Virtual, November 2020. doi: <https://doi.org/10.2118/201147-MS>

Suarez, L., Kenyery, F., Azuaje, M. et al. . 2005. 3D CFD Simulation of Rotary Gas-Separator Performance under Two-Phase-Flow Condition. Paper presented at the SPE Latin American and Caribbean Petroleum Engineering Conference, Rio de Janeiro, Brazil, 20–23 June. SPE-94959-MS. <https://doi.org/10.2118/94959-MS>.

Wang, S., Gomez, L., Mohan, R., Shoham, O., Kouba, G., & Marrelli, J. (2010). The state-of-the-art of gas-liquid cylindrical cyclone control technology: From laboratory to field.

Wang, Qinghua , Liu, Yonghui , Yang, Junzheng , Cui, Mingyue , and Dan Qi. "A Novel Downhole Gas Separator in ESP Systems." Paper presented at the SPE Asia Pacific Oil and Gas Conference and Exhibition, Brisbane, Australia, October 2018. doi: <https://doi.org/10.2118/192028-MS>

Wang, G., Yan, C., Fan, G., Wang, J., Xu, J., Zeng, X., & Liu, A. (2019). Experimental study on a swirl-vane separator for gas–liquid separation. *Chemical Engineering Research and Design*, 151, 108-119.

Wang, Y., Chen, J., Yang, Y., Han, M., Zhou, Y., Ye, S., ... & Yue, T. (2021). Experimental and numerical performance study of a downward dual-inlet gas-liquid cylindrical cyclone (GLCC). *Chemical Engineering Science*, 238, 116595.

Yin, J., Li, J., Ma, Y., Li, H., Liu, W., and Wang, D. (September 1, 2015). "Study on the Air Core Formation of a Gas–Liquid Separator." *ASME. J. Fluids Eng.* September 2015; 137(9): 091301. <https://doi.org/10.1115/1.4030198>

Zeng, X., Fan, G., Xu, J., Liu, A., Xu, Y., & Yan, C. (2020). Experimental study on a new gas–liquid separator for a wide range of gas volume fraction. *Chemical Engineering Research and Design*, 160, 561-570.

Zhang, Y., Chen, W., Liu, B., Feng, J., & Peng, X. (2018). Study on the Effects of Vane Parameters on Separation Performance in an Axial Flow Cyclone Separator.

Zheng C, Yang W, Wang G, Fan G, Yan C, Zeng X and Liu A (2019) Experimental Study on a New Type of Separator for Gas Liquid Separation. *Front. Energy Res.* 7:102. doi: 10.3389/fenrg.2019.00102

Zhou, F., Sun, G., Han, X., Zhang, Y., & Bi, W. (2018). Experimental and CFD study on effects of spiral guide vanes on cyclone performance. *Advanced Powder Technology*, 29(12), 3394-3403.

Zhu, H., Liu, Y., Tychus, D., Zheng, D., Zhu, J., & Zhang, H. Q. Tailpipe Design and Optimization for Mitigating Terrain Slug in Horizontal Wells. Available at SSRN 4429157.